PONTIFÍCIA UNIVERSIDADE CATÓLICA
DO RIO DE JANEIRO

Jorge Guillermo Díaz Rodríguez

Linear Elastic Fracture Mechanics Analysis of Fatigue Crack Growth under Complex Loading using the Digital Image Correlation Technique

Tese de Doutorado

Thesis presented to the Programa de Pós-graduação em Engenharia Mecânica of PUC–Rio, in partial fulfillment of the requirements for the degree of Doutor em Ciências - Engenharia Mecânica.

Advisor: Prof. José Luiz de França Freire

Rio de Janeiro
September 2018

PONTIFÍCIA UNIVERSIDADE CATÓLICA
DO RIO DE JANEIRO

Jorge Guillermo Díaz Rodríguez

Linear Elastic Fracture Mechanics Analysis of Fatigue Crack Growth under Complex Loading using the Digital Image Correlation Technique

Thesis presented to the Programa de Pós-graduação em Engenharia Mecânica of PUC–Rio in partial fulfillment of the requirements for the degree of Doutor em Ciências - Engenharia Mecânica. Approved by the undersigned Examination Committee.

Prof. José Luiz de França Freire
Advisor
Departamento de Engenharia Mecânica – PUC-Rio
Prof. Jaime Tupiassú Pinho de Castro
Departamento de Engenharia Mecânica – PUC-Rio
Prof. Arthur Martins Barbosa Braga
Departamento de Engenharia Mecânica – PUC-Rio
Prof. Leonardo Dantas Rodrigues
Instituto de Tecnologia – UFPA
Dr. Giancarlo Luis Gómez Gónzales

Prof. Márcio da Silveira Carvalho
Vice Dean of Graduate Studies
Centro Técnico Científico – PUC-Rio

Rio de Janeiro, September 12th, 2018

Jorge Guillermo Díaz Rodríguez

The author holds a degree in Mechanical Engineering from Universidad Industrial de Santander (Colombia) and a Masters degree in Engineering from the University of North Texas (TX, USA). His line of research and interest involves fracture mechanics, fatigue, and mechanical design.

Bibliographic data

Díaz Rodríguez, Jorge Guillermo

Linear elastic fracture mechanics analysis of fatigue crack growth under complex loading using the digital image correlation technique / Jorge Guillermo Díaz Rodríguez; advisor: José Luiz de França Freire. – 2018.

176 f. : il. color. ; 30 cm

Tese (doutorado)–Pontifícia Universidade Católica do Rio de Janeiro, Departamento de Engenharia Mecânica, 2018.

Inclui bibliografia

1. Engenharia Mecânica – Teses. 2. Correlação de imagens digitais. 3. Mecânica de fratura linear elástica. 4. Carregamento multiaxial. 5. Carregamentos não proporcionais. 6. Abertura da ponta da trinca. I. Freire, José Luiz de França. II. Pontifícia Universidade Católica do Rio de Janeiro. Departamento de Engenharia Mecânica. III. Título.

CDD: 621

A mis padres quienes siempre me incitaron a entregar lo mejor de mí.

To my wife and daugther who are my support, especially in the last four years.

Acknowledgements

In all theses and dissertations I read, there were always thanks and kind words for the advisor. However, in this case, whatever I say, it will not describe the timely help, suggestions, revisions, encouragement, and ideas given when results were not what we were hoping for. Thank you prof. José Luiz!

To the lab personnel: Julian, Vitor, Felippe, Graça, Dr. Eduardo Maneschy, Dr. Marco Guamán, Dr. Jesus L. Carvajalino and especially to Dr. Giancarlo L. González for the help with the Matlab code and some of the DIC measurements. Without him, this thesis could not have been done the way is presented.

To all my collegues at PUC: Andrés, Dr. Cesar, Dr. Luiz Fernando, Dr. Bruno, Giovani, Alexis, Sergio, Salvador, Dra. Lilia e Dra. Patricia.

To the professors at the department of mechanical engineering for the classes and wisdom, especially to: Arthur, Ivan, e Jaime. Additionally to Prof. Michael Vormwald and Dr. Yigiter Hos at TU Darmstadt in Germany for sharing the DIC data and for all the ideas and revisions given to the published works.

To the examination committee for the invaluable ideas and suggestions that helped shaping the final version of this thesis.

This study was financed in part by the Coordenação de aperfeiçoamento de pessoal de nivel superior Brasil (CAPES) – finance code 001.

Finally, to all the wonderful people who help me and my family during the four years we lived na cidade maravilhosa.

Abstract

Díaz Rodríguez, Jorge Guillermo; Freire, José Luiz de França (advisor); **Linear Elastic Fracture Mechanics Analysis of Fatigue Crack Growth under Complex Loading using the Digital Image Correlation Technique.** Rio de Janeiro, 2018. 176p. Doctoral thesis – Mechanical Engineering Department, Pontificia Universidade Catolica do Rio de Janeiro.

Fatigue crack propagation assessment includes identifying the crack direction, knowing the equivalent Stress Intensity Factor (SIF) range, determining a crack length growth rate per number of cycles (da/dN), and establishing a crack propagation rule connecting the equivalent SIF and da/dN rate, such as a Paris type of rule. When mixed and non-proportional loading occur, those parameters are not fully understood yet. This thesis deals with some of the variables that influence crack propagation under non-proportional mixed mode loading.

The Digital Image Correlation (DIC) technique was used to acquire images of test specimens subjected to cyclic proportional and non-proportional loading. Two types of specimen samples were used. Firstly, two different plate test specimens were tested; a disk compact tension (DCT), and a modified compact tension, C(T). They were subjected cyclic loading inducing crack opening mode I or proportional crack opening modes I and II. Secondly, the previously and elsewhere acquired DIC data for five thin tubes subject to cyclic loading were analyzed. The thin tubes had pre-fabricated slit-notches from which fatigue cracks initiated and propagated. Those five thin tubes were subjected to different cases of proportional and non- proportional loading. One tube specimen was exposed to axial loading and presented mode I crack opening. The other four were subjected to torsion loading or mixed axial-torsional loading and exhibited all three I, II and III crack-opening modes. The experimentally acquired DIC displacement fields were processed to independently calculate SIF for each existing opening mode using linear elastic fracture mechanics (LEFM) formulations. One formulation used full

field displacement data acquired in small areas that surrounded the crack tip. Another formulation used data acquired from a pair of points located along the opposite crack flanks. The determined SIFs were used to find equivalent SIFs and equivalent SIF ranges using the maximum tensile stress criterion (for both 2D and 3D versions of combinations of modes I-II and modes I-II-III respectively) which implicitly included the crack propagation angle. It was found that the inclusion of the experimentally determined mode III SIF indeed makes a difference in the determined equivalent SIF and equivalent SIF ranges.

A da/dN versus equivalent SIF ranges plot was drafted with the experimentally measured crack growth rates and the SIF ranges that were found by using the widely accepted assumption that the cracks grew in the direction that maximizes the tensile stress. For this, extensions of the Schöllmann et. al. model as well as of the Erdogan-Sih model, which are generally applied to proportional loading, were used to determine equivalent SIFs and equivalent SIF ranges for the cases of proportional and non-proportional loading. Finally, the second stage of the Paris rule (da/dN versus SIF range) was plotted for the five thin tubes loading cases showing that they fell inside a reasonably thin scattered band.

Keywords

Stress Intensity Factor; Linear Elastic Fracture Mechanics; Digital Image Correlation; Crack Opening Displacement; Least Square method; Multiaxial loading; Non-proportional loading.

Resumo

Díaz Rodríguez, Jorge Guillermo; Freire, José Luiz de França (orientador). **Análise do Crescimento de Trincas de Fadiga pela Mecânica de Fratura Elastica Linear sob Carga Complexa utilizando a Técnica de Correlação de Imagens Digitais.** Rio de Janeiro, 2018. 176p. Tese de Doutorado - Departamento de Engenharia Mecânica, Pontifícia Universidade Católica do Rio de Janeiro.

A avaliação da propagação de trincas de fadiga inclui a identificação da direção da trinca, o conhecimento do Fator de Intensidade de Tensões (SIF) equivalente, a determinação de uma taxa de crescimento de comprimento de trinca por número de ciclos da/dN e o estabelecimento de uma regra de propagação de trinca conectando SIF e da/dN, como uma regra de tipo Paris. Quando ocorrem cargas mistas e não proporcionais, esses parâmetros ainda não são totalmente compreendidos. Esta tese trata de algumas das variáveis que influenciam a propagação de trincas sob carregamento no modo misto não proporcional.

A técnica de Correlação de Imagens Digitais (DIC) foi utilizada para a aquisição de imagens de corpos de prova submetidos a carregamento proporcional e não proporcional cíclico. Dois tipos de corpos de prova foram utilizados. Primeiramente, dois corpos de prova planos foram testados; um disk compact tension (DCT, em inglês) e um compact tension modificado (C (T) em inglês). Eles foram submetidos a carregamento cíclico induzindo o modo I de abertura de trinca ou modos I e II de abertura de trinca proporcionais. Em segundo lugar, os dados DIC adquiridos anteriormente, e em outro lugar, para cinco tubos finos sujeitos a carregamento cíclico foram analisados. Os tubos finos tiveram entalhes usinados a partir dos quais as trincas por fadiga iniciaram e se propagaram. Esses cinco tubos finos foram submetidos a diferentes casos de carga proporcional e não proporcional. Um corpo de prova tipo tubo fino foi exposto a carga axial e apresentou modo de abertura de trinca tipo I. Os outros quatro foram submetidos a carregamento de torção ou carga axial-torcional mista e exibiram todos os três modos de abertura de

trinca I, II e III. Os campos de deslocamento adquiridos experimentalmente com a técnica DIC foram processados para calcular independentemente o SIF para cada modo de abertura existente usando formulações de mecânica de fratura elástica linear (MFLE). Uma formulação delas utilizou dados de deslocamento de campo completos adquiridos em pequenas áreas que circundavam a ponta da trinca. Outra formulação usou dados adquiridos de um par de pontos localizados ao longo dos flancos opostos das faces da trinca. Os SIFs determinados foram usados para encontrar os SIFs equivalentes e faixas de SIF equivalentes usando o critério da tensão máxima de tração (para ambas as versões 2D e 3D de combinações dos modos I-II e modos I-II-III respectivamente) que implicitamente incluíram o ângulo de propagação de trinca. Verificou-se que a inclusão do SIF no modo III experimentalmente determinado efetivamente faz diferença nas faixas do SIF e dos SIF equivalentes estimados.

A curva da/dN versus faixa do SIF equivalente foi elaborado com as taxas de crescimento de trinca medidas experimentalmente e as faixas de SIF que foram encontradas usando a suposição amplamente aceita de que as trincas cresceram na direção que maximiza a tensão de tração. Para isso, extensões do modelo de Schöllmann et. al. e bem como o modelo de Erdogan-Sih, que são geralmente aplicados ao carregamento proporcional, foram usados para determinar os SIFs equivalentes e faixas de SIF equivalentes para os casos de carregamento proporcional e não proporcional. Finalmente, a segunda zona da regra de Paris (da/dN versus faixa do SIF equivalente) foi plotada para os cinco casos de carregamento nos tubos finos mostrando que eles caíram dentro de uma faixa razoavelmente fina e dispersa.

Palavras-Chave

Fator de Intensidade de Tensões, Mecânica de Fratura Linear Elástica, abertura da ponta da trinca, método dos mínimos quadrados, carregamento multiaxial, carregamentos não proporcionais.

Table of contents

List of Figures

Tables

List of Acronyms

2D : Two dimension space

3D : Three dimension space

ASTM : American Society for Testing Materials

CAD : Computer Aided Design

C(T) : Compact Test Specimen

CCD : Charged Coupled Device

CTL : Crack Tip Location

CTD Crack Tip Displacement Criterion

CSD : Crack Sliding Displacement

COD : Crack Opening Displacement

CTOD : Crack Tip Opening Displacement (mode I)

$CTSD_{II}$: Crack Tip Sliding Displacement mode II

$CTSD_{III}$: Crack Tip Sliding Displacement mode III

CTOA : Crack Tip Opening Angle

DCT : Disk Compact Test coupon

DIC : Digital Image Correlation

FEM : Finite Element Method

FCG : Fatigue Crack Growth

IR : Infrared

LSM : Least Squares Method

MEER : Maximum Energy Release Rate Criterion

MTS : Maximum Tangential Stress Criterion

MTSN : Maximum Tangential Strain Criterion

SAE : Society of Automotive Engineers

SED : Strain Energy Density Criterion

SG : Strain Gage

SSD : Squared sum of difference correlation criterion

TSA : Thermoelastic Stress Analysis

UTM : Universal Testing Machine

List of Symbols

A	: Area
a	: Crack length
a*	: Accumulated crack length
da	: Crack grow increment
da/dN	: Crack growth per cycle N
E	: Young´s modulus
f	: Moiré fringe orders
F	: Applied force
G	: Shear modulus
G	: Energy release rate
i	: Complex number, or consecutive counter
K	: Stress Intensity Factor
Kc	: Critical Stress Intensity Factor
K_{Ic}	: Critical Stress Intensity Factor mode I
Keff	: Effective Stress Intensity Factor
Keq	: Equivalent SIF (under mixed mode loading)
R_L=	: Axial load reversal ratio
R_T=	: Torsional load reversal ratio
Sx, Sy, Sz	: DIC correlation error in X, Y and Z directions respectively.
u	: Displacement in X direction
v	: Displacement in Y direction
w	: Displacement in Z direction
W	: Residual ligament in a cracked specimen

Δ	: Increment
ΔKth	: SIF propagation threshold
δ	: Crack Tip Opening Displacement, CTOD
σ	: Normal stress
σ_o	: Yield strength
$\sigma_{o\,x}$	: Stress acting along the crack edges (T-stress)
σ_u	: Ultimate strength
τ	: Shear stress
$\jmath$	: J integral
ν	: Poisson modulus
θ	: angular direction of a point with respect to crack tip
θ^*	: direction of crack kinking with respect to crack path
Ψ	: direction of crack twisting (out of plane)
θoES	: direction of crack kinking as predicted by Erdogan-Sih model
$\theta oS3D$	: direction of crack kinking as predicted by Schöllmann et. al. model

1. Introduction

In 1982, the US department of commerce estimated a loss in order of 119 billion dollars due to structural integrity failures. It also estimated that the annual losses could be reduced to $35 billion if available technology was applied [1]. Bridges, buildings, airplanes, ships, pipes and pressure vessels - which are large, critical, and expensive structures - have flaws that make them must-monitor-for-cracks targets. Theoretical and/or numerical models are used to predict crack growth and stress fields caused by a diverse number of different types of flaws. Some of these models advise users about errors in calculation, mainly due to their inherently complex geometry, whereas others work only with very particular ranges of parameters.

For Mechanics of Materials calculation, the material is assumed as a continuum, whereas with Fracture Mechanics, the internal flaws are considered. Therefore, it can be said that a flaw (several microns or several millimeters long) undermines the macrostructure load bearing capacity. Models for integrity assessment around flaws are based on limiting states that compare loading and material capacity. On the other side, structural load, component geometry, and crack length are combined as "crack parameters" such as: the Stress Intensity Factor (SIF), the Crack Tip Opening Displacement (CTOD, δ), the J integral ($\int$), and the Energy release rate (G). They were proposed analytically, verified experimentally with different techniques and numerically with the Finite Element Method (FEM) or its derivations. The material strength properties for integrity assessment, such as fracture thoughness, are determined following standards (Zhu and Joyce [2] did a very thorough review in 2012). Once calculation of the chosen crack parameter is performed, it is compared to the respective material property. A graphical comparison with Mechanics of Materials is shown in Figure 1-1. In Mechanics of Materials the acting load, in conjunction with geometry, produces an acting stress state (σ) which is increased if a stress concentrator (K_t) is present. That combination $\sigma * K_t$ must be lower than the material property, such as: the yield strength, the

ultimate strength, the maximum allowable strain, etc. However, in Fracture Mechanics only acting crack opening positive loads are considered, producing an acting stress. The flaw dimensions in conjunction with the applied stress produce a SIF (or ⌡, δ or G depending on what parameter is used). For Linear Elastic Fracture Mechanics (LEFM), if the SIF surpasses the equivalent material toughness property ($K_{I c}$ or K_c) according to a standard criteria, that body is labeled as not fit for service. Therefore, calculating those parameters (SIF, ⌡, δ or G) is a key step while performing a structural integrity assessment.

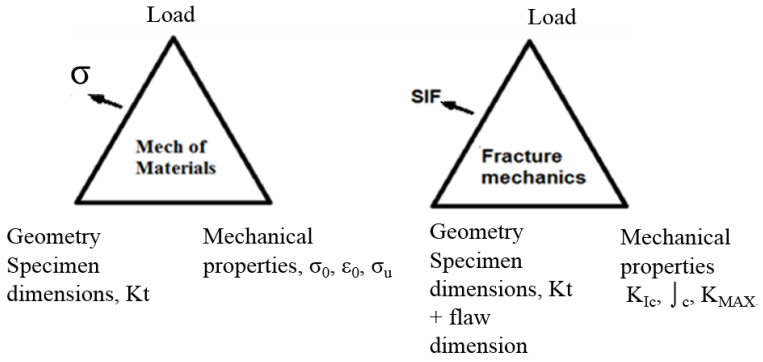

Figure 1-1. Comparison between Mechanics of Materials and Fracture Mechanics

There are several methods, based on different experimental techniques to calculate fracture mechanics parameters. One of them is the Digital Image Correlation technique (DIC), which is non-intrusive, requires little sample preparation, and can map the whole surface stress field in a body. It has disadvantages as well; such as moderately high cost, the need for a level of expertise, the data post processing can be awkward, and their limitation to see how stress changes inside the sample. Overall, it is more advantageous than traditional methods such as strain gages (SG) and photoelasticity

Structural integrity standards, such as API 579, define levels of assessment, being level I the most conservative and level III closer to reality than the levels I and II. Cracked body problems, for which there is no analytical or tabulated solution, or that do not pass level I and II of said norm, need to be solved by sophisticated techniques (FEM is a popular option). However, a helpful FEM simulation relies on reproducing accurately boundary conditions and creating an appropriate mesh, which can be time consuming. Such procedures are used in industries where time is of the essence by having unproductive assets. Experimental

measures provide the basis for understanding the physics of problems and they are the base to propose models that later are used in simulations.

This thesis presents the experimental analysis of three kind of samples subjected to fatigue crack growth: a Disk Compact Test (DCT) specimen under pure mode I, a modified Compact Test (C(T)) specimen under proportional modes I and II, and five thin tubes under: pure and proportional or non-proportional mixed-mode loading. Furthermore, it also presents how the SIF and SIF ranges were calculated. Finally, it attempts to explain how the cracks direction behave and how they propagate.

1.1 Fracture Mechanics

The problem of dealing with geometric discontinuities dates back to German engineer Ernst Gustav Kirsch in 1898 when he proposed a stress solution for an infinite plate with a circular hole. In 1913, British engineer Charles Inglis widened the solution to elliptical holes showing that stress will grow as the ellipse flattens. In 1920, British engineer Alan Arnold Griffith used an energy approach in brittle materials, relating crack growth with stored potential energy. It is what is known as Energy release rate (G). It, however, intrinsically neglects energy associated with metal plasticity. In 1939, Danish professor Harold Malcolm Westergaard, working at Harvard, used complex functions to develop a whole stress field solution for an infinite cracked plate with equibiaxial loads [1–3].

Meanwhile, World War II (WWII) came and there was a need to quickly manufacture ships. Welding was the chosen method for that, but its rapid manufacturing time came with problems that were unknown of back then. Famous, is the case of the Liberty ships that cracked even while at port. Bad quality welds, rough conditions in the North Atlantic Ocean, and low toughness materials were the causes for such failures. After WWII, from October 1953 to April 1954, three British De Havilland Comets, the first commercial jetliner produced, crashed in mid-flight for no apparent reason. A posteriori analysis determined that sharp corner windows caused fatigue cracks to growth to critical length. The entire fleet was grounded until 1958. Once the problem was fixed, the company had such a bad

of reputation that it could not recover financially and eventually lost the market to American Boeing 707 and Douglas DC8 jets. On a different, but conclusive event, in 1969 the crash of American bomber F111, due to an overseen crack in a D6aC steel (a type of SAE 4340) pin that held a wing, made the aeronautic industry implement fail-safe design policies based on Fracture Mechanics [3].

Nearly twenty years later after Westergaard, American physicist George Rankine Irwin, while working at the US Naval Research Laboratory, showed that Westergaard´s solution could be simplified in the area surrounding the crack tip. He proposed the SIF concept, fathering modern Fracture Mechanics [4].

The advantage of Irwin´s solution (which is simplified) over Westergaard´s (exact) are:

- Irwin´s solution is accurate at the crack tip, exactly where it matters. Only the crack tip surroundings regulate how fast the crack can grow, in what path, and whether it fails catastrophically or not [3].
- Irwin´s solution lead to the SIF definition, probably the paramount of fracture mechanics.

The same year, American professor Max L. Williams [5] from CalTech, arrived at the same solution using trigonometric functions. The result is an expansion series that is identical to Irwin solution when using only the first term in the expansion. They both arrived to the same solution.

Figure 1-2 shows the three possible opening modes for cracked bodies. Mode I is opening perpendicular to crack faces, mode II is sliding parallel to crack faces, and mode III is out of plane sliding.

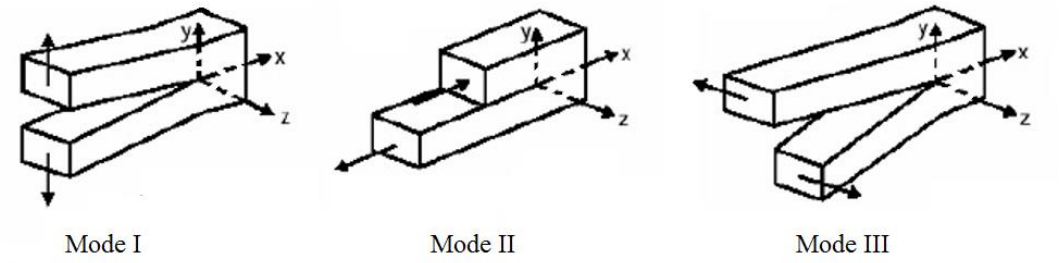

Figure 1-2. Opening modes for cracks

Three years later, a team lead by Dr. Paul Paris [6] at the University of Washington proposed the SIF range (ΔK) as the driving force for fatigue crack growth.

If loads do not produce large plastic zones ahead of the crack tip or the material does not exhibit plastic work, SIF works just fine. Otherwise, a different parameter needs to be used to describe stress field. In 1960 after observing that bending specimens deformed too much to be characterized with SIF, British scientist Alan Wells, from The Welding Institute (TWI), came up with the COD, nowadays termed CTOD (Crack Tip Opening Displacement). He was able to show that a critical CTOD, in wide plate specimens of the same thickness under bending were equivalent, proving that fracture toughness can be transferred from test coupons to field geometries [2]. In 1967, Russian scientist Gerady Cherepanov [7], from the Institute of Mechanics Moscow, and American professor James Rice [8], from Brown University in 1968, independently proposed a method to calculate the energy strain release rate per surface in a cracked material. It was a follow up on work done in 1956 by Dr. John D. Eshelby at the University of Birmingham. It was named J integral (⌡) which it is a purely mechanic model that does not take into account microstructure [3]. Hutchinson, Rice and Rosengreen showed that ⌡ characterizes stresses and strains at the crack tip for nonlinear materials, making it an energy parameter and a stress intensity parameter as well [1].

The first attempt to explain crack path (CP) direction was done in 1963 by professors Fazil Erdogan and George Sih [9] from Lehigh University who proposed that cracks under mixed-mode (proportional I and II modes) grow in the direction of maximum tangential stress (MTS). Later in 1973, prof. Sih proposed that a crack grows along the direction where strain energy density (SED) is minimum [10]. In 1974 Goldstein and Salganik [11] proposed a criteria named local symmetry (LS) which gave very close results as MTS. Same year, Strifors [12] proposed a criteria for mixed mode based on the ⌡, treating them as vectors, named the apparent crack extension force criterion (CEF). One year later, R. J. Nuismer [13] proposed that cracks grow in the direction which guarantees that they release the maximum energy (MEER). In 1981 Chang [14] proposed a model assuming cracks advance in the direction where the tangential strain energy is maximum. One year later, P. Theocaris and N. P. Andrianopoulos [15] proposed a model based on the

assumption that cracks propagate when the dilatational strain energy reaches a critical value. In 1989 Papadopoulos [16] took into account the third stress invariant, stating that the angle for crack growth is controlled on the condition that the norm of the stress tensor takes a maximum value. However, in 1992 Spyropoulos challenged its foundations, stating it is composed of two different magnitudes, so they cannot be added freely. Same year, prof. Chingshen Li [17] from the Taiwan University of Technology proposed that cracks take the direction of the rate of SIF in mixed mode. Maccagano and Knott [18] came up with a model based on the Maximum Shear Stress (MSS) for materials prone to shear or for loading cases where shear is dominating. A team led by Schöllmann and Richard [19] proposed a model that included K_{III} in the input variables as well as the crack angle. Wasiluk and Golos [20] in 2000 proposed a model based on an adimmensional plastic zone radius. More recently, in 2016 Demir et. al. [21] proposed an empirical model fitting experimental data to a polynomial and logarithmic model. All in all, it can be said that all CP prediction models state a hypothesis for crack increase direction and increment generally is created when an equivalent SIF (Keq) surpasses a material property.

In the present century, a couple of researchers stand out for their work on crack path prediction. Prof Hans Albert Richard from Universität Paderborn. Prof. Sylvie Pommier from École Normale Supérieure Paris-Saclay (Cachan), and Prof. Michael Vormwald from Technische Universität Darmstadt, both in Germany. The first one introduced a crack twisting angle model and an equivalent SIF model which included mode III with an implicit crack kinking angle [19] that later was reduced to an empirical model [22]. It has been implemented in the ADAPCRACK3D [1] FEM software. The second one has been working extensively on modeling fatigue crack growth aiming to include non-linear effects such as fatigue history, damage accumulation, plasticity and roughness induced crack

[1] http://www.dlr.de/Portaldata/23/Resources/dokumente/wsk_2012/Simulation_der_Rissausbreitung_unter_komplexen_Lasten.pdf

Last accessed January 4, 2018

closure, creep, corrosion and thermal effects. Finally, the last researcher has tackled the problem equivalent SIF and crack path under non-proportional loading.

In the last few years, there has been a number of works in non-proportional loading. There are works describing the macroscopical aspects of fatigue crack growth under non-proportional loading for hollow tubes [23], the microstructure transition when going from tensile to shear dominating fracture [24]. One more work identifying factors that affect crack behavior, among them are: crack tip plasticity, load reversal ratio, material anisotropy, geometry, mean applied stress, and mode-mixity [25]. Another one attempted to numerically reproduce FCG results from round samples made out of low carbon steel alternating from a tensile to shear dominated crack growth criteria where an attempt to identify fracture mode transition was made where, however, they acknowledged that the effect of load reversal was not considered [26]. A similar job was performed by Yu, Li and Proust [27] but working with Aluminum. However, when calculating SIF, they did so with established numerical formulas, and they also did not report K_{III}, although the samples were tubes under torsion and axial load. Their loading cases can compare to some of the cases reported in this thesis. However they applied a minimum of R_L=0,2 and R_T=0, as follows: their LC1 is R-028 here, their LC4 is R-030 here. Finally, they also used the Erdogan-Sih (MTS), MSS and SED criteria to predict crack growth finding the SED is the closest to proportional loading crack path prediction. There is one article modeling material behavior under non-proportional loading using a Caboche material model and considering kinematic hardening with the Amstrong-Frederick rule [28]. Mei et. al. [29] applied an equivalent SIF model, using compliance functions for C(T) specimens made out of AISI/SAE 1070 steel under modes I and III, that accounts for loading path history by combining da/dN data from different loading tests founding that it can successfully correlate FCG data from both, proportional and non-proportional mixed-mode loading conditions. Frémy, Pommier, Poncelet, et. al. [30] subjected a plate to a three independent-axis loading conditions, however with an R_L=0,33 to avoid crack closure effects, measuring FCG rates with the DIC technique. The applied SIF and their sequence were chosen carefully to always achieve the same SIF peaks at the same time. They showed that non-proportional crack growth is influenced by loading path for the tested conditions, something was mentioned earlier in 1983 by Tschegg et. al [31]

but, in a way, challenged in 1985 by Pook [32] who stated that despite noisy results, non-proportional FCG in modes I and III could be described by Paris rule except for out-of-phase crack growth.

This thesis uses the experimental data from [33] taking advantage of the measured DIC displacement fields to calculate LEFM parameters and establish a FCG rule combining different loading conditions.

1.2 Methods to calculate Fracture Mechanics parameters

Right after models to calculate fracture mechanics parameters were proposed, calculation using experimental techniques has been comprehensively explored. In literature is well documented the working principle, input / output variables and data posprocessing for local measurements (strain gages) and optical methods (photoelasticity, caustics, Moiré, and more recently DIC).

For many years Irwin´s method [34], along with Wells and Post [35], were used to extract SIF from photoelastic patterns. It was Irwin [4] in 1957 who suggested using SG to measure SIF, but Dally and Sanford [36] in 1987 were the first who successfully used them to calculate SIF in different configurations of CT specimens. Barker et. al. [37] proposed in 1984 a general algorithm to calculate stress-field parameters in mode I. Although it was developed for Moiré, it can be labelled as the first approach to calculate stress field parameters for opaque materials, as it can be extended to any technique that gives full field displacements. In 1987, McNeill et. al. [38] fitted DIC data to Westergaard solution using LSM to establish K_I. Sanford in 1989 [39] extended Barker´s method [37] to include non-singular terms in the solution. Lopez-Crespo et. al [40] in 2008 calculated SIF by fitting DIC measurements to Muskhelishvili stress functions, and attempted to locate crack tip location using image processing techniques. The same year, Yates et. al [41] used DIC to measure SIF, T-stress and crack tip opening angle (CTOA) from displacement fields using Williams solution. In 2012 Zhang and He [42] used DIC to compute SIF, T-stress, rigid body motion, and rotation by fitting displacement fields under mixed loading conditions to Williams equations in a Plexiglas C(T) sample. In 2014, Hos, Vormwald, and Freire [43, 44], used

commercial DIC to calculate SIF in thin tubes loaded in mixed mode under complex tension-torsion loading using DIC strain data to fit Irwin´s solution. Harilal et. al. [45] introduced crack tip coordinates as unknowns into Williams solution. Kotousov et. al. [46] measured SIF variation through thickness by taking DIC data on a rotated angle from the focal plane, and same authors in [47], using a semi disk in a three-point bending test collecting DIC displacement data, established the radii at which 3D effects can be estimated.

1.3 Motivation

There are numerous techniques available in literature that address SIF, and da/dN vs. ΔK calculation from experimental data. However, several problems arise when calculating them. In the case of SIF they are:

- The exact location of the crack tip is fundamental to determine an accurate SIF value.
- The number of terms used in Williams' series influences the solution depending on how far from the CTL one goes to extract data to determine and to analyze SIF.
- When using DIC data, one can use Williams' series for displacement, strain or stress. The two latter may give erroneous results due to inherent noise.
- The high deformation gradient around the crack tip may induce an error in the solution by feeding models false data.
- When in presence of induced plasticity or a partially opened crack, readings need to be analyzed properly to avoid false interpretations[48–50] .
- For non-proportional loading, crack path and equivalent SIF is not fully understood yet [23–25, 51].

SG have a problem with their finite size. In addition to that, in the past the availability of other more efficient experimental methods, such as photoelasticity, and compliance made SG a second choice to measure Fracture Mechanics parameters. On the other hand, photoelasticity may have difficulties in opaque materials and compliance techniques are not practical in dynamic applications [52]. The radial location of SG is restricted by inherent problems, such as plasticity

effects, three-dimensional effects and high strain gradients. Large strain gradients, near the crack tip, also cause large averaging errors due to the finite size of SG [52]. This was confirmed by Kotousov [47] using DIC and numerical techniques.

Hos, Vormwald and Freire [43] analyzed data for subjected thin-walled pipes to five types fatigue loading: pure tension-compression, pure torsion, proportional tension- torsion, out-of-phase tension- torsion with a phase angle of 45°, and out-of-phase tension- torsion with a phase angle of 90°. They estimated crack length, crack growth, near crack edge deformation, and crack closure using 3D DIC. SIF were reported for loads in tension calculated by fitting DIC stresses to Westergaard's equations. Results are compared to FEM results using ABAQUS´® ⌡ routine. In another paper [44], same authors determined SIF via COD (a pair of points with simplified William´s equations) and with strains from many points which were reduced using LSM using DIC strain data, both ways at the working maximum and minimum loads for pure tension-compression, proportional tension-torsion, and pure torsion. Additionally, they plotted the da/dN vs. ΔK curve for the pure tension-compression case only. The authors identified some problems:

- SIF values were calculated with strains and stresses from DIC data. As pointed out before, they might lead to inaccurate readings due to inherent noise.
- Reported SIF values differ between COD and LSM using DIC strain data for axially loaded sample. Such difference may be attributed to the difficulty of pinpointing the CTL and to the inherent noise when derivating displacements to calculate strains.

As mentioned before, crack path is not fully understood yet [53] [20]. There are models based on stress, energy, and critical plane calculation. For mode I, they give accurate predictions and for in-phase mixed-mode loading some of them perform well, and actually they are used in commercial crack growth simulation software. Miranda et. al [54] investigated crack propagation under proportional mixed-mode comparing, and founding excellent agreement, experimental results with numerical simulations with a considerably reduction in computing time by using the Maximum Tangential Stress criterion (MTS) and self-adapting meshes to calculate SIF at each crack increment. However, the question remains open when loads are out-phase. Yang [26] performed simulations on thin tubes subjected to

proportional and non-proportional loads, similar to [23] [43], alternating MTS and Maximum Shear Stress criterion (MSS) criteria looking for a parameter that could tell when the crack path changes from tensile to shear dominated growth. Although there were differences in crack growth rates, being the simulated ones more conservative, the simulated crack path was close to experiments. Vormwald [53] observed that there is a predisposition to underestimate fatigue lives when non-proportional loading is involved, and at the same time, he acknowledged several issues in FCG that affect accurate prediction such as mixed-mode ratio and crack closure.

Although this thesis does not answer the question of crack path under non-proportional loading, models for crack kinking were evaluated for in-phase and out-of-phase loading using SIF calculated from the experimentally obtained DIC displacement fields. A comparison of crack growth rates is made for the thin tubes finding they might be explained by an Erdogan-Sih propagation rule, although with a high dispersion.

1.4 Thesis Objective

From the experimental data acquired by Hos [33] published and analyzed in [28, 43, 44, 48], there is still much more information that can be analyzed such as, SIF, a da/dN vs. ΔK curve, and crack path prediction, for the five types of loading. After those parameters were calculated, an attempt will be made to explain their behavior, such as SIF, SIF range, and crack path in mixed mode for the complex loading cases. It is important to highlight that the experiments related in [29, 30], were performed at Technische Universität Darmstadt (Germany), and processed at PUC´s Photomechanics lab using the software 3D-VIC from Correlated Solutions®. To gain confidence in calculating SIF from displacement fields, simpler experiments (sections 4.1 and 4.2) were performed to tests the methods and models and experimental results were compared to FEM modeling solutions.

As a result, this thesis determines SIF and SIF range for fatigue tests that involve tension and torsion loads including complex loading such as the ones described at the beginning of this section. For this, it was conducted a study of

methods that could be used with DIC, analyzing their physical fundamentals, input/output variables, and sensitivity to change in input variables. The suitable methods were implemented to process the collected data, so information could be properly analyzed. The research question at hand is to answer whether the da/dN vs. ΔK curve correlates for different types of loading or not. Thus, the objectives can be summarized as follows:

- To determine a FCG rule that combines proportional and non-proportional mixed mode loading cases.
- To study LEFM formulations for SIF, SIF ranges and equivalent SIF, the methods to calculate them using displacement field such as the ones acquired by the DIC technique.
- To perform an evaluation of crack kinking models for the determined SIF and SIF ranges calculated from the experimentally acquired displacement fields.

1.5 Thesis Outline

This thesis is divided in seven chapters. The first is the introduction and presents the objectives. The second has the relevant theoretical background needed to develop the work. The third one presents a review on models for crack path propagation. The fourth describes the performed tests and how the methods were used to analyze results, especially how an existant equivalent SIF for proportional loading can be used to evaluate equivalent SIF under non-proportional loading. The fifth chapter reports findings on SIF, SIF ranges, and equivalent SIF ranges. Then, the sixth chapter discusses such results, how models for crack kinking perform for the specimens tested, and it shows the comparison of equivalent SIF ranges using Paris rule. Finally the seventh chapter draws conclusion and suggests future work.

2.
Literature Review

This chapter reviews the derivation and definition and of necessary concepts and techniques used to analyze the performed tests. The nomenclature for the relevant mechanical models, derived in the past, may have been altered here to comply with only one arbitrary standard.

2.1.
Digital Image Correlation

DIC started in 1982 at the University of South Carolina [55]. Later in 1983 [56], a paper described a method to estimate deformation from a photographed deformed sample and another one [57] described how to compute rigid body displacements. Nowadays, it is the most extensively used technique for experimental mechanics, and it has its own dedicated annual conference[2].

DIC is a non-contact optical technique that uses one (DIC-2D) or more (DIC-3D) cameras to account for displacement, rigid body, rotation and out-of-plane displacement in case of DIC-3D. The technique uses a virtual mesh to discretize the aerea of interest (AOI) in smaller elements called subsets, see Figure 2-1.

DIC takes advantage of the gray intensity change within a subset in sequential photographs taken on a sample before and after deformation [58]. Photographs are acquired digitally, i.e. by a digital camera (CMOS or CCD), or by traditional methods which subsequently are digitalized as maps of bytes $f(x,y)$ making possible to compare grey intensity before and after deformation to obtain displacement fields using a correlation criteria. Eq. (1) shows the squared sum of difference correlation criterion, SSD. Sutton et. al. [58] warns that although the SSD is the least influenced

[2] http://idics.org/

by-light-variation optimization criteria, it is also the most computer time consuming method.

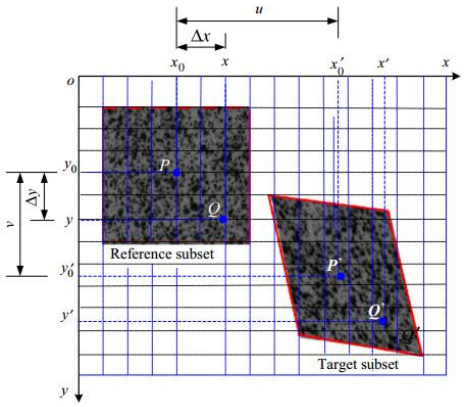

Figure 2-1. Notation before and after deformation images (adapted from [42])

$$SSD = \min \sum_{x=-M}^{M} \sum_{y=-N}^{N} \left[g(x'y') - f(x,y) \right]^2 \tag{1}$$

where SSD is the correlation criteria, f(x, y) and g(x', y') represent the grey levels of reference before and after deformation; and(x, y) and (x', y') are the coordinates of a point in the subset before and after deformation. The coordinate (x', y'), after deformation, is related to the coordinate (x, y), before deformation, with Eq. (2) following the schematics depicted in Figure 2-1.

$$\begin{aligned} x' &= x + u + \frac{\partial u}{\partial x}\Delta x + \frac{\partial u}{\partial y}\Delta y + \frac{1}{2}\frac{\partial^2 u}{\partial x^2}\Delta x^2 + \frac{1}{2}\frac{\partial^2 u}{\partial y^2}\Delta y^2 + \frac{1}{2}\frac{\partial^2 u}{\partial x \partial y}\Delta x \Delta y \\ y' &= y + \mathrm{v} + \frac{\partial \mathrm{v}}{\partial x}\Delta x + \frac{\partial \mathrm{v}}{\partial y}\Delta y + \frac{1}{2}\frac{\partial^2 v}{\partial y^2}\Delta x^2 + \frac{1}{2}\frac{\partial^2 v}{\partial y^2}\Delta y^2 + \frac{1}{2}\frac{\partial^2 v}{\partial x \partial y}\Delta x \Delta y \end{aligned} \tag{2}$$

DIC provides independent values of displacement *u* and *v* in directions X, Y; in the case of 3D DIC, the *w* displacement in Z direction can be obtained as well. Moreover, DIC technique that can be used to measure small or large samples, static or dynamics events, and rigid or soft materials. The speckles can be added by ink spray, can be etched, or stamped [52, 58, 59].

One of the most important task in experimental work is preparing the sample, organizing the equipment (Cameras, light source, and computer controller), and calibrating the experiment. The DIC technique is not exempted of doing so. Here it

is briefly described how to perform those tasks for hard materials while performing solid mechanics measurements.

Sample preparation. The sample should be clean and polished to minimize external interference. Then, the speckles are added over a white coating with speckles size in accordance with spatial resolution and lens magnification. As rule of thumb, speckles should about 3 to 4 pixels in size. They can be applied with airbrush, with a standard spray aerosol, a regular brush, off the shelf stickers, or rubber stamped. Nonetheless the method, the pattern should non-repetitive, isotropic and exhibit a high contrast. Because the cameras are usually black and white, those colors are recommended for the speckles.

Equipment: Cameras are usually monochromatic and with a high resolution (nowadays a 6MPixels resolution is easily achieved). The light source should be in accordance with the camera´s minimum exposure time being room light the one that needs the longest and a stroboscope the fastest exposure time. The 3D-VIC user manual[3] recommends keeping external motion under 0.02 pixels therefore, the light frequency should be chosen according to the frame acquisition rate. Finally, the computer controller triggers cameras, synchronizes the testing matching to record analog signals.

Experiment calibration. Its objective is to provide a field of view from known coordinates. This is achieved by placing grids of known separation in front of the cameras, recording them and processing them to create such envelope. The calibration includes intrinsic parameter (focal length, aspect ratio, and sensor center) as well as extrinsic parameters (such as relative linear and angular position between cameras). The latter will change in case the cameras are moved during the experiment [3].

[3] For details and a more extentive instructions, see the "3D-VIC 2010 testing and reference guide" or "A Good Practices Guide for Digital Image Correlation" availbable at: https://doi.org/10.32720/idics/gpg.ed1

2.2
Stress Intensity Factor

When stressed bodies are in presence of macroscopic flaws, they exhibit a non-linear intensification near the crack tip. Westergaard [1] proposed an Airy stress function (ϕ) and developed a complex number solution for an infinite plate with a crack in the center. The proposed solution describes the whole stress field around the crack, which is summarized in Table 1. A thorough deduction and proof can be found in [1] or [3].

Table 1. Summary of the Westergaard complex function

Function ϕ	$\phi = \mathrm{Re}(\overline{\overline{Z}}) + i\,\mathrm{Im}(\overline{Z})$
Z	$Z(z) = \dfrac{\sigma_\infty}{\sqrt{1-(a/z)^2}}$
$\overline{\overline{Z}}$	$\iint$ Z
$\overline{Z}$	$\int$ Z
Z	z=x+*i*y

where *a* is crack length, z position, and σ_ω remote stress.

Stress fields around a crack´s vicinity exhibit a non-linear intensification near the crack tip, which depends on $1/\sqrt{r}$. However, Westergaard solution was awkward to use in engineering practice. The stress field ahead of a crack tip (Figure 2-2) in an isotropic linear elastic material, can be accurately represented by the SIF, as shown in Eq. (3).

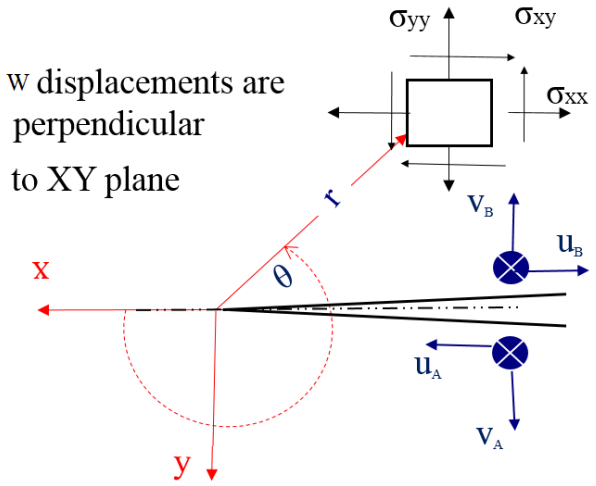

Figure 2-2. Notation for stress, displacements, and position near a crack

$$\sigma_{ij} = \frac{K}{\sqrt{2\pi r}} f_{ij}(\theta) + higher\ order\ terms\ (r,\theta) \qquad (3)$$

which is known as the Irwin solution. The term $f_{ij\ (\Theta)}$ is a function of the measured angle and geometry. When approaching the crack, the prevalent term is the first one, so higher order terms can be dismissed. It can be seen how stresses vary linearly with the SIF, so in presence of a crack, the stress field is described by the SIF. It has to be pointed that the equations in Table 2, Table 3, and Table 4 include a $1/\sqrt{r}$ term, which describes the influence of distance from the CTL on stress and displacements and reveals a singularity at r=0. So, in theory stresses go to infinite for points closer to the CTL. For mode I (opening mode) stress and displacements are summarized in Table 2 [1].

Table 2. Stress and displacements for mode I

Stress	Displacement
$\sigma_{xx} = \frac{K_I}{\sqrt{2\pi r}} \cos\frac{\theta}{2}\left[1 - \sin\frac{\theta}{2}\sin\frac{3\theta}{2}\right]$ $\sigma_{yy} = \frac{K_I}{\sqrt{2\pi r}} \cos\frac{\theta}{2}\left[1 + \sin\frac{\theta}{2}\sin\frac{3\theta}{2}\right]$ $\tau_{xy} = \frac{K_I}{\sqrt{2\pi r}} \cos\frac{\theta}{2}\sin\frac{\theta}{2}\cos\frac{3\theta}{2}$	$u = \frac{K_I}{2G}\sqrt{\frac{r}{2\pi}} \cos\frac{\theta}{2}\left[k - 1 + 2\sin^2\frac{\theta}{2}\right]$ $v = \frac{K_I}{2G}\sqrt{\frac{r}{2\pi}} \sin\frac{\theta}{2}\left[k + 1 - 2\cos^2\frac{\theta}{2}\right]$

For mode II (in-plane) stress and displacements are presented in Table 3 [1]:

Table 3. Stress and displacements for mode II

Stress	Displacement
$\sigma_{xx} = -\frac{K_{II}}{\sqrt{2\pi r}} \sin\frac{\theta}{2}\left[2 + \cos\frac{\theta}{2}\cos\frac{3\theta}{2}\right]$ $\sigma_{yy} = \frac{K_{II}}{\sqrt{2\pi r}} \sin\frac{\theta}{2}\cos\frac{\theta}{2}\cos\frac{3\theta}{2}$ $\tau_{xy} = \frac{K_{II}}{\sqrt{2\pi r}} \cos\frac{\theta}{2}\left[1 - \sin\frac{\theta}{2}\cos\frac{3\theta}{2}\right]$	$u = \frac{K_{II}}{2G}\sqrt{\frac{r}{2\pi}} \sin\frac{\theta}{2}\left[k + 1 + 2\cos^2\frac{\theta}{2}\right]$ $\mathrm{v} = \frac{-K_{II}}{2G}\sqrt{\frac{r}{2\pi}} \cos\frac{\theta}{2}\left[k - 1 - 2\sin^2\frac{\theta}{2}\right]$

Finally, mode III (out of plane) stress and displacements are presented in Table 4 [1].

Table 4. Stress and displacements for mode III

Stress	Displacement
$\tau_{xz} = \frac{-K_{III}}{\sqrt{2\pi r}} \sin\frac{\theta}{2}$ $\tau_{yz} = \frac{K_{III}}{\sqrt{2\pi r}} \cos\frac{\theta}{2}$	$w = 2\frac{K_{III}}{G}\sqrt{\frac{r}{2\pi}} \sin\frac{\theta}{2}$

where *k* is the Kolosov constant given by (4).

$$k = \begin{cases} 3 - 4\nu; \varepsilon_{pl} \\ \frac{3-\nu}{1+\nu}; \sigma_{pl} \end{cases} \tag{4}$$

On the other hand, Williams' solution is expressed as an infinite series of *n* terms [5], as shown in Eq. (5) for displacement.

$$u=\sum_{n=1}^{\infty}\frac{r^{n/2}}{2G}\left(\begin{array}{l}a_n\left\{\left[k+\frac{n}{2}+(-1)^n\right]C\,\mathrm{os}\frac{n\theta}{2}-\frac{n}{2}C\,\mathrm{os}\left(\frac{n-4}{2}\right)\theta\right\}-\\ b_n\left\{\left[k+\frac{n}{2}-(-1)^n\right]Sin\frac{n\theta}{2}-\frac{n}{2}Sin\left(\frac{n-4}{2}\right)\theta\right\}\end{array}\right)$$

$$\mathrm{v}=\sum_{n=1}^{\infty}\frac{r^{n/2}}{2G}\left(\begin{array}{l}a_n\left\{\left[k-\frac{n}{2}+(-1)^n\right]Sin\frac{n\theta}{2}+\frac{n}{2}Sin\left(\frac{n-4}{2}\right)\theta\right\}+\\ b_n\left\{\left[k-\frac{n}{2}+(-1)^n\right]Cos\frac{n\theta}{2}+\frac{n}{2}Cos\left(\frac{n-4}{2}\right)\theta\right\}\end{array}\right) \qquad (5)$$

$$w=\sum_{n=1}^{\infty}\left\{\frac{2r^{n-\frac{1}{2}}}{G}c_n Sin\left(n-\frac{1}{2}\right)\theta\right\}$$

where a_1= $K_I/\sqrt{2\pi}$, b_1=$K_{II}/\sqrt{2\pi}$, c_1=$K_{III}/\sqrt{2\pi}$, a_2=$\sigma_{ox}/4$,

2.3
Crack Tip Opening Displacement

SIF mode I can be also calculated from COD, and $CTSD_{II}$ for mode II and $CTSD_{III}$ for mode III, if points *A* and *B*, from Figure 2-2, are considered to be ±180 degrees from the crack tip. Then Eqs. (5) are simplified to Eqs. (6).

$$K_{I,II}=\frac{E\cdot COD_{I,II}}{4}\sqrt{\frac{2\pi}{r}}\quad ;\quad K_{III}=\frac{E\cdot COD_{III}}{4(1+\nu)}\sqrt{\frac{2\pi}{r}}$$
$$COD_{\mathrm{I}}=v_A-v_B\qquad COD_{\mathrm{II}}=u_A-u_B\qquad COD_{\mathrm{III}}=w_A-w_B \qquad (6)$$

However, if points *A* and *B* do not fall within the ±180 degrees assumption of Eq. (6), SIF can be represented by Eq. (7) by using the first term of Eq. (5).

$$K_I=\frac{E\Delta \mathrm{v}}{2(1+\nu)}\left\{\sqrt{\frac{r_A}{2\pi}}\sin\frac{\theta_A}{2}\left[\frac{2}{1+\nu}-\cos^2\frac{\theta_A}{2}\right]-\sqrt{\frac{r_B}{2\pi}}\sin\frac{\theta_B}{2}\left[\frac{2}{1+\nu}-\cos^2\frac{\theta_B}{2}\right]\right\}^{-1}$$

$$K_{II}=\frac{E\Delta \mathrm{u}}{2(1+\nu)}\left\{\sqrt{\frac{r_A}{2\pi}}\sin\frac{\theta_A}{2}\left[\frac{2}{1+\nu}+\cos^2\frac{\theta_A}{2}\right]-\sqrt{\frac{r_B}{2\pi}}\sin\frac{\theta_B}{2}\left[\frac{2}{1+\nu}+\cos^2\frac{\theta_B}{2}\right]\right\}^{-1} \qquad (7)$$

$$K_{III}=\frac{E\Delta \mathrm{w}}{2(1+\nu)}\left\{\sqrt{\frac{r_A}{2\pi}}\sin\frac{\theta_A}{2}-\sqrt{\frac{r_B}{2\pi}}\sin\frac{\theta_B}{2}\right\}^{-1}$$

where Δu, Δv and Δw are the relative displacement between points *A* and *B* from Figure 2-2 in *x, y* and *z* direction respectively. It can be seen in Eq. (6) and Eq.

(7) that SIF should not depend on the position of the evaluation points because further-from-the-CTL-points exhibit larger displacements and viceversa. Therefore, SIF describes the displacement field and, it is proportional to the relative displacements between two-opposite-to-the-crack points. Henceforth, COD indistinctly refers to COD, $CTSD_{II}$, and $CTSD_{III}$ unless specified otherwise.

2.4
J integral

Path-independent integrals are used in exact sciences to estimate the intensity of a field with a singularity and /or with profile uncertainty in the vicinity of the singularity, and they are derived from conservation laws. J can be physically interpreted as the system potential energy relief rate in relation to the variation of crack length [7, 8]. It is presented in Eq. (8).

$$J = \int_{\Gamma} \left[W dy - \bar{T}_i \frac{\delta u_i}{\delta x_i} \delta s \right]; \ (i = x, y) \tag{8}$$

where W is the strain energy density, u_i is displacement, x the crack growth direction, T is stress vector, and δs is length increment along the chosen path. J is path independent for an open path [8, 59].

Because J works on plastic zones, even though the path is arbitrary (i.e. Figure 2-3), a sufficiently small contour can be made. A rectangular path is probably the most common, but a curvilinear one has advantages as well. As pointed out before, there are problems evaluating J. Therefore, it is important to understand what all of J terms represent when evaluated it those two paths. Below is the J deduction for a rectangular path implemented in [49].

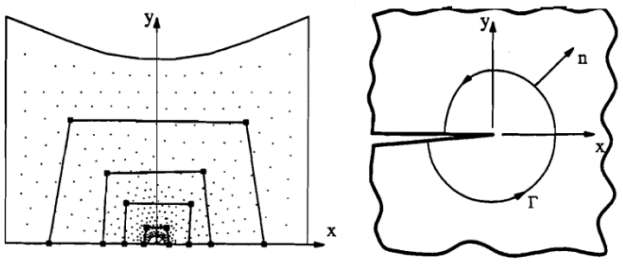

Figure 2-3. Different paths for J. Quasi-rectangular and quasi-circular, adapted from [1].

In Eq. (8), with the normal vector shown in Figure 2-4, the stress vector can be expressed as:

$$\bar{T}_i ds = \sigma_{ij} n_j ds$$

$$T_i = \begin{vmatrix} \sigma_{xx} & \tau_{xy} \\ \tau_{xy} & \sigma_{yy} \end{vmatrix} \begin{vmatrix} n_x \\ n_y \end{vmatrix}$$

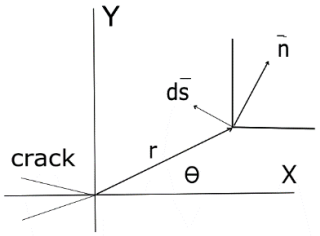

Figure 2-4. Normal Vector to Crack Position

For a position at a distance *r* and at angle θ measured from the crack tip, as shown in Figure 2-4, the normal vector *n* can be expressed as $n = \cos\theta i + \text{sen}\theta j$:

The increments *dx* and *dy* along the path can be expressed as:

$$dx = -ds Sin\theta \rightarrow Sin\theta = -\frac{dx}{ds} = n_x$$

$$dy = ds Cos\theta \rightarrow Cos\theta = \frac{dy}{ds} = n_y$$

Then, replacing them in Eq. (8), and for a rectangular path, J can be calculated as Eq. (9).

$$J = \int_{\Gamma} W dy - \int_{\Gamma} \left[\overrightarrow{Tx} \frac{\delta u}{\delta x} + \overrightarrow{Ty} \frac{\delta v}{\delta y} \right] \delta s \qquad (9)$$

Expanding the traction vector, Eq. (9) becomes Eq. (10).

$$J = \int_{\Gamma} W dy - \int_{\Gamma x} \left[\tau_{xy} \frac{\partial u}{\partial x} + \sigma_{yy} \frac{\partial v}{\partial y} \right] dx - \int_{\Gamma y} \left[\tau_{xy} \frac{\partial v}{\partial x} + \sigma_{xx} \frac{\partial u}{\partial y} \right] dy \qquad (10)$$

where the strain energy, *W*, is a function of principal stresses and strains shown in Eq. (11).

$$W = \frac{\left[\sigma_1 \varepsilon_1 + \sigma_2 \varepsilon_2 \right]}{2} \qquad (11)$$

The expression in Eq. (10) represents the energy per unit area [J/m^2, J/mm^2] spent in opening the crack. Therefore, if more than one loading mode is present, J represents the sum of energy per unit area in each loading direction, or: $J = J_I + J_{II} + J_{III}$ [60, 61].

2.5
Methods to determine SIF using DIC

With the recorded data from DIC measurements, posprocessing has to be done. Using full field displacement data, Barker, Sanford and Chona [37] fit data to Westergaard equations (Table 1) mounting a linear system shown in Eq. (12).

$$[h] = [b][\Delta] \tag{12}$$

where matrix *[b]* contains the functions of position terms described in Eq. (5), *{Δ}* is the unknown vector coefficients of the stress function, and *{h}* the concatenated vector of known displacements. One can see it may yield an over-determined system that can be solved by LSM, as shown in Eq. (13).

$$[\Delta] = \left[b^T b\right]^{-1} [b]^T [h] \tag{13}$$

McNeill et. al. [38], using DIC displacements, established K_I in small areas (1.27 cm x 1.27 cm) from a C-specimen made out Plexiglas and compared results to ASTM solution. They fit measured displacements to Eq. (14).

$$h_1(r,\theta) = \frac{K_I}{G}\sqrt{\frac{r}{2\pi}}\sin\frac{\theta}{2}\left[\frac{2}{1+\nu} - \cos^2\frac{\theta}{2}\right] + A_2 f_2 \tag{14}$$

where h_1 is the measured point displacement and A_2 and f_2 account for body rigid motion. It becomes imperative that CTL location has to be chosen correctly. They ran a routine repeatedly using different CTL until the error was minimized.

Sanford [39] extended Barker´s method [37] to include non-singular terms in the solution. He claimed an increase in accuracy and a back-then non-existent capability to deduce additional information about fracture parameters from the added nonsingular terms. He applied the method to holographic interferometry, Moiré and photoleasticity. For photoelasticity, the series are expressed in Eq. (15),

where N'_o is the the fringe order, f_p the unknown initial fringe order, and t the material thickness.

$$\frac{N' f_p}{2t} = \sum_{n=0}^{\infty} A_n r^{n-\frac{1}{2}} Cos(n-\frac{1}{2})\theta + \sum_{m=0}^{\infty} B_m r^m Cos(m\theta) + \frac{N_o}{2} \tag{15}$$

which returns an over determined system that can be resolved by the LSM method showed in Eq. (12). More recently, Zhang and He [42] computed SIF from DIC displacements fields on an Aluminum C(T) sample with a R_L= 0,4 by expressing Williams' displacement fields as Eq. (16).

$$\begin{aligned} u &= \sum_{n=1}^{N} C_n f_{In(r,\theta)} - \sum_{n=1}^{N} D_n f_{IIn(r,\theta)} + T_x - Ry_n \\ \mathrm{v} &= \sum_{n=1}^{N} C_n g_{In(r,\theta)} - \sum_{n=1}^{N} D_n g_{IIn(r,\theta)} + T_y + Rx_n \end{aligned} \tag{16}$$

where N is the number of terms of the expansion of the displacement field, T_x and T_y are the rigid body components in x and y respectively and Ry_n and Rx_n the rigid body rotation. The two equations can be rewritten as matrix form as Eq. (12), where [b(r, θ)] is a matrix composed of functions described in Eq. (17).

$$h = \begin{bmatrix} u_1 \\ \vdots \\ u_M \\ \mathrm{v}_1 \\ \vdots \\ \mathrm{v}_M \end{bmatrix} \quad ; \Delta = \begin{bmatrix} C_1 \\ \vdots \\ C_M \\ D_1 \\ \vdots \\ D_M \end{bmatrix} ; b = \begin{bmatrix} f_{I1(r1,\theta1)} & \cdots & f_{II1(r1,\theta1)} & \cdots & 1 & 0 & -y_1 \\ \vdots & \ddots & \vdots & \ddots & \vdots & \vdots & \vdots \\ f_{IM(rM,\theta M)} & \cdots & f_{IIM(rM,\theta M)} & \cdots & 1 & 0 & -y_1 \\ g_{I1(r1,\theta1)} & \cdots & g_{II1(r1,\theta1)} & \cdots & 0 & 1 & x_1 \\ \vdots & \ddots & \vdots & \ddots & \vdots & \vdots & \vdots \\ g_{IM(rM,\theta M)} & \cdots & g_{IIM(rM,\theta M)} & \cdots & 0 & 1 & x_1 \end{bmatrix} \tag{17}$$

where functions in Eq. (17) are detailed in Eq. (18). This method was implemented and used in [49].

$$f_{In(r,\theta)} = \frac{r^{n/2}}{2G}\left[\left(k - \frac{n}{2} + (-1)^n\right)Cos\frac{n\theta}{2} - \frac{n}{2}Cos\theta\left(\frac{n}{2} - 2\right)\right]$$

$$f_{IIn(r,\theta)} = \frac{r^{n/2}}{2G}\left[\left(k + \frac{n}{2} - (-1)^n\right)Sin\frac{n\theta}{2} - \frac{n}{2}Sin\theta\left(\frac{n}{2} - 2\right)\right]$$

$$g_{In(r,\theta)} = \frac{r^{n/2}}{2G}\left[\left(k - \frac{n}{2} - (-1)^n\right)Sin\frac{n\theta}{2} + \frac{n}{2}Sin\theta\left(\frac{n}{2} - 2\right)\right] \quad (18)$$

$$g_{IIn(r,\theta)} = \frac{r^{n/2}}{2G}\left[\left(-k + \frac{n}{2} - (-1)^n\right)Cos\frac{n\theta}{2} - \frac{n}{2}Cos\theta\left(\frac{n}{2} - 2\right)\right]$$

In an analog way, Williams series, expressed in Eq. (5), for mode III can be rewritten as Eq. (19).

$$w = \sum_{n=1}^{N} c_n p_{n(r,\theta)} + T_z + Rz_n \quad (19)$$

where Tz is rigid body displacement in perpendicular-to-plane and Rzn rotation about perpendicular-to-crack-plane axis.

The expansion is arranged as Eq. (20), which may yield an over determined system that can be solved by the LSM, as presented previously in Eq. (13).

$$\{h_{III}\} = [b_{III}]\{\Delta_{III}\} \quad (20)$$

with h_{III}, Δ_{III}, and b_{III} defined in Eq. (21).

$$h_{III} = \begin{bmatrix} w_1 \\ \vdots \\ w_M \end{bmatrix}; \Delta_{III} = \begin{bmatrix} C_1 \\ \vdots \\ C_M \end{bmatrix}; b_{III} = \begin{bmatrix} p_{1(r_1,\theta_1)} \\ \vdots \\ p_{M(r_M,\theta_M)} \\ 1 \\ 1 \end{bmatrix}^T \quad (21)$$

where M is the number of data points, and functions $p_{i(r,\theta)}$ of $[b_{III}]$ are expressed in Eq. (22).

$$p_{n(r,\theta)} = \frac{2r^{n-1/2}}{G}\left\{c_n Sin\left(n - \frac{1}{2}\right)\theta\right\} \quad (22)$$

Hos, Vormwald, and Freire [44] calculated SIF from strain using derived DIC displacement data using Eq. (23).

$$\varepsilon_{xx}+\varepsilon_{yy}=\frac{2(1-\nu)}{E\sqrt{\frac{2\pi}{r}}}\left[K_I\cos\frac{\theta}{2}-K_{II}\sin\frac{\theta}{2}\right]+\frac{2(1-\nu)}{E}\sigma_{oX} \tag{23}$$

Once again, Eq. (23) is a linear system that can be solved by the LSM. For only mode I, $K_{II}=0$ and Eq. (23) can be simplified to Eq. (24). It has to be noted that this was the first study found where SIF were measured via DIC with the load inversion ratio (R_L) set at -1 and performed in a ductile material so crack closure was largely visible.

$$\varepsilon_{xx}+\varepsilon_{yy}=\frac{2C}{\sqrt{\frac{2\pi}{r}}}\left[K_I\cos\frac{\theta}{2}\right] \tag{24}$$

To calculate SIF via COD, Eq. **(**6), Eq. (7) or LSM via Eq. (12), one needs to choose at least two points (as shown in Figure 2-2), identify their position with respect to CTL, and extract orthogonal displacements.

He and Kotouzov [62], performing a numerical regression with the *w*-field DIC data from a 3-point bending test, identified crack corner effects and found a correlation between SIF mode I and said field. The expression is described by Eq. (25).

$$\mathrm{w}(r,\theta,\pm t)\approx\frac{-1{,}34\nu}{E}K_I\sqrt{\frac{t}{2}} \tag{25}$$

Their method is somewhat restricted to: relatively brittle materials, thick plates or low loads at which the plastic zone is much smaller than 1/20th of plate thickness, *t*.

2.6
Methods to Determine ⌡ using DIC

The advantage of using DIC to calculate ⌡, is that DIC measures the whole displacement field, whereas strain gages measure displacements along a selected contour which is fixed. Furthermore, if the selected contour lies within the elastic part of the field, the non-linear area around the CTL can be avoided [63]. Yoneyama et. al. [59] evaluated ⌡ using path and area formulations, that included plasticity, by

modeling the stress-strain behavior with a Ramberg-Osgood material model. Moreover, strains and stresses can be estimated using continuum mechanics equations. Therefore, terms in Eq. (8) are already known, minimizing DIC post processing. However, Eq. (8) was implemented following a recommendation found in the ANSYS manual and implemented in [49] to calculate derivatives as follows.

a) Choose a path that encloses a crack
b) Measure the length of the path
c) Calculate Δx_i as a 1% of the chosen path.
d) Dislocate the path on $-\Delta x_i/2$ and $+\Delta x_i/2$
e) Extract directional displacement along the alleged dislocated paths
f) Calculate derivatives as shown in Eq. (26):

$$\frac{\partial u_i}{\partial x_i} = \frac{u_i\big|_{+\Delta x_i/2} - u_i\big|_{-\Delta x_i/2}}{\Delta x_i} \tag{26}$$

g) Repeat d), e) and f) for the other direction

The procedure is graphically explained in Figure 2-5, where the original and dislocated paths enclosing the crack can be seen.

Because the resulting small path shifts from the above recommendation, it was very difficult to manually extract that kind of information on VIC-3D. A Matlab ® algorithm [49] was used which reads DIC data (position and displacement), computes the derivatives, and ⌡with Eq. (8) by using path formulation. In this case, the path length is chosen as 100 times the pixel spacing.

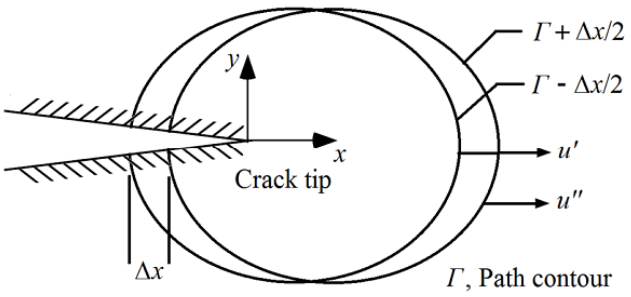

Figure 2-5. Path dislocation to obtain derivatives [49].

Because ⌡ calculates the total energy per unit area spent to grow a crack regardless of the loading direction(s), a technique named M-integral was devised by Yau et. al [64] in 1980 from the University of Illinois to separate the ⌡ value in each loading direction using auxiliary displacement fields with a beforehand known

solution [26, 60]. Another way to separate ⌡ in each direction is taking advantage of the displacements field symmetry and antisymmetry with respect to the crack axis [61].

2.7. da/dN vs. ΔK curve

The linear portion of Paris curve [6] can be obtained by plotting the logarithm of crack growth rate (da/dN) versus the logarithm of SIF range (ΔK), as shown in Eq. (27).

$$Log\left(\frac{da}{dN}\right) = mLog(\Delta K) + LogC \tag{27}$$

Taking a logarithm on both sides of Eq. (27), it gives a straight line, becoming Eq. (28).

$$\frac{da}{dN} = C\left[\Delta K\right]^m \tag{28}$$

Coefficients (*C* and *m*) for Eq. (27) are fitted experimentally, using for example the Levenberg-Marquardt or the least squares algorithms. Paris rule is plotted in Figure 2-6, where there are three distinctive zones A, B and C. Zone A is where no crack growth is perceived, zone B is where a linear relation is visible, and zone *C* is where the crack growth advances very rapidly. However, Eq. (27) does not represent the following situations:

- Because Eq. (27) is a linear relation, da/dN works only in zone B, leaving zones A and C out of prediction estimates. Althought there are several variations, and additions, to Paris rule many of them are thoroughly reviewed by [3].
- When the body is subjected to remote plastic loading, ΔK no longer describes the stress field. In that case, Δ⌡ [65, 66] and CTOD [67] have been used as crack driving parameters in analogous da/dN curves.

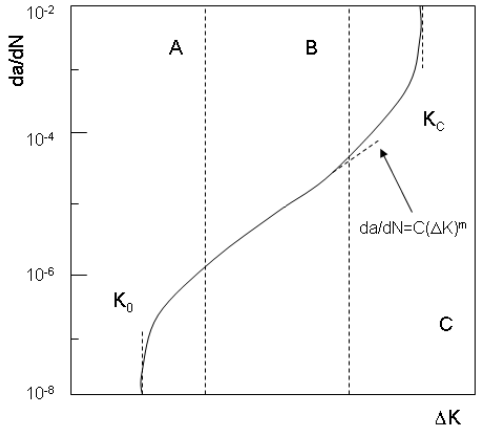

Figure 2-6. Paris´ Law

It is expected that the plastic deformation ahead of the tip of the crack will leave a residual stress. When the specimen is unloaded, it builds up residual compressive stresses ahead of the crack tip. When the load goes to zero, a higher maximum SIF (K_{max}) must be applied to overcome the residual compressive stresses and accumulated plasticity on the crack flanks (and open the crack) so that the measured SIF range threshold (ΔK_{th}) needed for crack growth is augmented. In other words, if the specimen is completely unloaded, a higher SIF has to be applied in order to open the crack because the applied SIF has to overcome accumulated effects of plastic deformation ahead and before the CTL.

3. LEFM Mixed-Mode Criteria

One of the problems in mixed-mode loading to be yet fully understood is to predict crack grow direction [20, 51, 53]. Nonetheless, the problem of crack kinking and equivalent SIF already has several postulated criteria.

This chapter presents the principles and deduction of selected fracture criteria models to determine crack path and to calculate SIF under mixed mode. Models are stress based, energy based, or/and suported on experimental observations. The understanding of crack and SIF performance is fundamental for modeling cracked bodies behavior using numerical techniques, such as FEM. Although most of the models were initially proposed for brittle materials, they have extended (and used) for ductile materials [27]. Comprehensive and contemporary reviews are available in literature. Recently, Rozumek and Macha [68] summarized equivalent SIF models, whereas Mróz and Mróz [51] did the same for crack kinking and twisting angles. Vormwald [25] summarized problems encountered in crack growth under non-proportional loading being mode-mixity the most important, whereas Pommier [69] pointed that load amplitude and history, material non-linear behavior, and crack roughness as relevant factors. Although most of the work presented in current literature has been done for crack initiation, this chapter presents some of the models used to predict crack path direction.

3.1 Models Based on Stress

Several authors derived crack kinking angle formulation using stress field equations. Here there are presented some of them.

3.1.1
Maximum Tangential Stress Criterion (MTS or ES)

The Maximum Hoop Stress, Maximum Tangential Stress (MTS), Maximum Tensile Stress or Maximum Normal-to-Crack Stress or simply Erdogan-Sih Criterion (ES) [9] postulates that a crack under mixed-mode (I-II) loading will propagate in the direction perpendicular to the maximum tangential stress ($\sigma_{\theta\theta}$) and ahead of the crack tip.

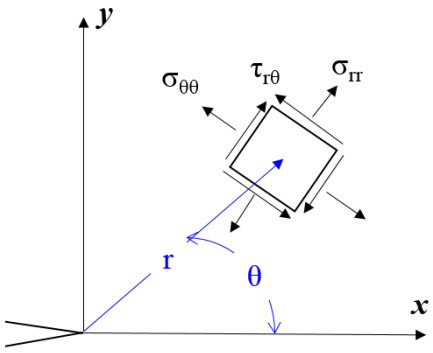

Figure 3-1. Notation for stress

The stress acting ahead of a crack, shown in Figure 3-1, are given by Eq. (29).

$$\sigma_{rr} = \frac{\cos\left(\frac{\theta}{2}\right)}{\sqrt{2\pi r}}\left[K_I\left(1+sin^2\left(\frac{\theta}{2}\right)\right)+K_{II}\left(\frac{3}{2}\sin\theta-2\tan\left(\frac{\theta}{2}\right)\right)\right]$$

$$\sigma_{\theta\theta} = \frac{\cos\left(\frac{\theta}{2}\right)}{\sqrt{2\pi r}}\left[K_I\cos^2\left(\frac{\theta}{2}\right)-K_{II}\frac{3}{2}\sin\theta\right] \qquad (29)$$

$$\sigma_{r\theta} = \frac{\cos\left(\frac{\theta}{2}\right)}{2\sqrt{2\pi r}}\left[K_I\sin\theta+K_{II}\left(3\cos\theta-1\right)\right]$$

Now, the angle of maximum tangential stress (θ*, which according to this hypothesis is the crack propagation angle as well), is full filled by Eq. (30).

$$\frac{\partial\sigma_{\theta\theta}}{\partial\theta}=0 \quad \text{and} \quad \frac{\partial^2\sigma_{\theta\theta}}{\partial\theta^2}>0 \qquad (30)$$

That hypothesis implicates that the shear stress $\sigma_{r\theta}$ in Eq. (29) is zero, which is given in Eq. (31).

$$-\frac{3}{4}\cos\left(\frac{\theta}{2}\right)\left[K_I \sin\theta + K_{II}\left(3\cos\theta - 1\right)\right] = 0 \tag{31}$$

There is a trivial solution for θ=±180 degrees, which corresponds to crack faces. The solution for the terms inside the parenthesis in Eq. (31) gives θ* as shown in Eq. (32).

$$\theta_{MTS} = 2\tan^{-1}\left(\frac{K_I}{4K_{II}} - \left(\frac{\operatorname{sgn}\left[\frac{K_I}{K_{II}}\right]}{4}\right)\sqrt{\left(\frac{K_I}{K_{II}}\right)^2 + 8}\right) \tag{32}$$

Because the ES criterion is based solely on stress, it does not depend on plane stress/strain conditions[4]. The sign of the radical in Eq. (32) takes the opposite value of the ratio K_I/K_{II}, which means the kinking angle depends on the direction of SIF mode II. A negative K_I does not make physical sense, but as it is shown later, K_{II} indeed may take negative values.

3.1.2
Maximum Shear Stress Criterion (MSS)

It was proposed in 1992 by Maccagno and Knott [18] for materials mainly sensible to a shear-dominated loading, especially for pure mode II or at elevated K_{II}/K_I ratios, where the fracture path is macroscopically prone to shear. The MSS criterion predicts crack growth on the direction along the plane of maximum $\sigma_{r\theta}$ when it exceeds a critical shear stress (τ_{cr}). The angle θ^* of this maximum shear plane is found by solving:

$$\frac{\partial\sigma_{r\theta}}{\partial\theta} = 0 \quad \text{and} \quad \frac{\partial^2\sigma_{r\theta}}{\partial\theta^2} > 0 \tag{33}$$

There is no analytical solution for the derivative shown in Eq. (33). Hinghsmith [24] cites a polynomial solution depending on the $\tan^{-1}(K_I/K_{II})$ parameter. In 2012, Habousa et. al. [70] performed data fitting finding Eq. (34).

[4] Panasuk developed a criteria based on the same principle. (Panasuk, V.V., 1968. Limiting balance of brittle bodies with cracks. publ. Naukova Dumka, Kiev, 246 p. (in Russian).

$$\theta_{MSS} = \text{sgn}\left[K_{II}\right]\frac{\pi}{4}\tan^{-1}\left[\sqrt{\pi}\left|\frac{K_I}{K_{II}}\right|\right] \tag{34}$$

where the crack angle, θ_{MSS}, has the same sign of K_{II}.

3.1.4
Richard Criteria

Richard criteria assumes that a crack will grow perpendicular to the principal stress and from the crack front when the equivalent SIF, under mixed mode conditions (I and II), exceeds K_{Ic}. For planar mixed mode conditions, this hypothesis is equivalent to the MTS criterion. They proposed a solution [71] in terms of normalized SIF for each direction, as seen in Eq. (35).

$$\theta^*_{R2D} = \mp\left[115^o\frac{\left|K_{II}\right|}{K_I+\left|K_{II}\right|} - 83,4^o\left(\frac{\left|K_{II}\right|}{K_I+\left|K_{II}\right|}\right)^2\right] \tag{35}$$

where θ^* is the crack kinking angle measured from an axis aligned with the crack growth direction.

3.1.5
Schöllmann Criteria

For 3D problems, Schöllmann et. al. [19] proposed a model which included K_{III}. Assuming $\sigma_z = 0$ (orthogonal to surface stress), they found the equivalent principal stress, and then differentiated $\sigma_1(\theta, K_I, K_{II}, K_{III})$ partially with respect to θ, to find an implicit function for crack kinking shown in Eq. (36).

$$\begin{aligned}&-6K_I\tan\frac{\theta}{2} - K_{II}\left(6-12\tan^2\frac{\theta}{2}\right) + \left\{\begin{array}{l}\left[4K_I - 12K_{II}\tan\dfrac{\theta}{2}\right] \\ \left[-6K_I\tan\dfrac{\theta}{2} - K_{II}\left(6-12\tan^2\dfrac{\theta}{2}\right)\right] \\ -32{K_{III}}^2\tan^2\dfrac{\theta}{2}\left(1+K_I\tan^2\dfrac{\theta}{2}\right)^2\end{array}\right\} \\ &\left\{\left[4K_I - 12K_{II}\tan\frac{\theta}{2}\right]^2 + 64{K_{III}}^2\left(1+\tan^2\frac{\theta}{2}\right)^2\right\}^{1/2} = 0\end{aligned} \tag{36}$$

In [19] they claimed that this criterion "is appropriate for the description of crack growth, except in cases such as crack growth in anisotropic materials or the

sliding of cracks under pure Mode II or Mode III loading". From the same principle, they also proposed Eq. (37) for crack twisting.

$$\Psi = 0,5tg^{-1}\left(\frac{2\sigma_{\theta z(\theta^*)}}{\sigma_{\theta\theta(\theta^*)} - \sigma_{zz(\theta^*)}}\right) \tag{37}$$

One can see that Eq. (36) is implicit, so there is no analytical solution that readily gives the crack kinking angle. After many experimental tests a few years later, Richard et. al. [22] fit results and proposed the expression shown in Eq. (38).

$$\theta^*_{R3D} = \mp\left[140^o \frac{|K_{II}|}{K_I + |K_{II}| + |K_{III}|} - 70^o\left(\frac{|K_{II}|}{K_I + |K_{II}| + |K_{III}|}\right)^2\right] \tag{38}$$

As one can see, the application of this crack criteria was simplified by going from an implicit, Eq. (36), to and explicit equation, Eq. (38) in the same manner as it was done in Eq. (35) by the same author.

3.2
Models Based on Energy

Some authors derived crack kinking angle predictions using energy principles. This section presents some of them.

3.2.1
Strain Energy Density Criterion (SED)

In 1974 Sih [10] proposed the strain energy density criterion, which predicts crack growth along the direction of the minimum strain energy density (*S)* under mode I and II, as shown in Eq.(39b).

$$\begin{aligned} S &= \frac{1}{16\pi G\cos\Psi}\left[a_{11}K_I^{\,2} + 2a_{12}K_IK_{II} + a_{22}K_{II}^{\,2}\right] \\ a_{11} &= \left(k - \cos\theta\right)\left(1 + \cos\theta\right) \\ a_{12} &= \sin\theta\left(2\cos\theta - (k-1)\right) \\ a_{22} &= (k+1)\left(1 - \cos\theta\right) + \left(1 + \cos\theta\right)\left(3\cos\theta - 1\right) \end{aligned} \tag{39a}$$

where *k* is the kolosov constant and Ψ is the angle of crack twisting (out of plane) as observed in the upper rigth hand of Figure 5-43a. Therefore, in this thesis the SED equations use the initial Ψ value measured from the DIC photos at the internal slit surface. In 1980 Badaliance [72] extended the model to include mode III loading, as presented in Eq. (39b).

$$
\begin{aligned}
S &= \frac{1}{16\pi G \cos\Psi}\left[a_{11}K_I{}^2 + 2a_{12}K_I K_{II} + a_{22}K_{II}{}^2 + a_{33}K_{III}{}^2 \right] \\
a_{11} &= \left(k - \cos\theta\right)\left(1 + \cos\theta\right) \\
a_{12} &= \sin\theta\left(2\cos\theta - (k-1)\right) \\
a_{22} &= (k+1)\left(1 - \cos\theta\right) + \left(1 + \cos\theta\right)\left(3\cos\theta - 1\right) \\
a_{33} &= 4
\end{aligned}
\tag{39b}
$$

Badaliance himself found a good agreement with the MTS criterion. However, according to Highsmith [24], this criterion does not represent shear controlled crack growth accurately.

3.2.2
Maximum Energy Release Rate Criterion (MEER)

The Griffith criteria states that crack growth implicates energy dissipation. An amount of energy is needed to create two new separated surfaces (the two new crack faces). The energy release rate G is shown in Eq. (40) for isotropic, linear elastic solids.

$$
G = \frac{1-\nu^2}{E}\left\{ K_I{}^2 + K_{II}{}^2 \right\} \tag{40}
$$

The MEER was proposed by Nuismer [13] and states that a crack will propagate in the direction which the energy release rate is maximum. Before its publication, it had been discussed earlier by Erdogan and Sih [9], and they concluded that crack initiation happens when such rate attains a critical value.

For a kinked crack, the MEER can be calculated as a function of angle θ from the crack tip using stress field equations, such as the ones from Irwin formulation. Nuismer matched the SIF for the straight and kinked cracks in order to project the kinking angle as seen in Eq. (41), where k_i are the SIF for the kinked crack.

$$G = \frac{1}{E'}\left\{k_{1\,(\theta)}^{\,2} + k_{2\,(\theta)}^{\,2}\right\}$$

$$k_{1\,(\theta)}^{\,2} = \left(\frac{4}{3+\cos^2\theta}\right)\left(\frac{\pi-\theta}{\pi+\theta}\right)^{\frac{\theta}{2\pi}}\left(K_I\cos\theta + \frac{3}{2}K_{II}\sin\theta\right) \tag{41}$$

$$k_{2\,(\theta)}^{\,2} = \left(\frac{4}{3+\cos^2\theta}\right)\left(\frac{\pi-\theta}{\pi+\theta}\right)^{\frac{\theta}{2\pi}}\left(K_{II}\cos\theta - \frac{1}{2}K_I\sin\theta\right)$$

Upon taking Eq. (41) first derivative with respect to θ and matching it to zero, one will find the crack kinking angle given by the MEER criterion.

3.2.3
Maximum Tangential Strain (MTSN)

Chang [14] developed a criteria based on the assumption that crack growth happens in the direction on which the normal strain factor attains a maximum value. It is an extension of Saint Venant's maximum normal strain theory, and it is shown in Eq. (42).

$$\begin{aligned} C &= \frac{1}{64G}\left[b_{11}K_I^{\,2} + b_{12}K_IK_{II} + b_{22}K_{II}^{\,2}\right] \\ b_{11} &= (1+\cos\theta)(k+2+\cos\theta) \\ b_{12} &= \sin\theta - \frac{3}{2} - k - 3\cos\theta \\ b_{22} &= 3\sin^2\theta(k+3\cos\theta) \end{aligned} \tag{42}$$

Upon using an analog derivative such as Eq. (30), one can find the propagating kink angle according to the MTSN criterion.

3.3
Other Criteria

This section presents two more criteria that do not fit into the aforementioned categories. One that depends on crack tip opening and another one that uses curve fitting to experimental data to get a predicting equation.

3.3.1
Demir Criteria

Demir and Ayhan (2016) [21] fitted experimental and numerical data from two different coupons (T and CTS test samples) to a multiparameter equation to find a mixed- mode I/II kink angle criteria, leaving out pure mode I loading, as seen in Eq. (43).

$$\theta^* = a + b\ln K_I + c\ln K_I^{\,2} + d\ln K_I^{\,3} + e\ln K_I^{\,4} + f\ln K_I^{\,5} + hK_{II} + gK_{II}^{\,2} + iK_{II}^{\,3} + jK_{II}^{\,4} + kK_{II}^{\,5} \quad (43)$$

where the coefficients are seen in Table **5**.

Table 5. Coefficients for Demir criteria

a	b	c	d	e	f	g	h	i	j	k
-0,7907	2,0365	-3,4144	2,2844	-0,5928	0,0456	1,1736	-2,6539	1,8244	-0,533	0,0565

The difference of this model is that they included the assembly (pins, bushes, and grips) and not only the test coupons in the numerical modeling rather than just the sample.

3.3.2
Crack Tip Displacement Criterion (CTD)

The crack tip displacement (CTD) criterion was proposed in 1989 by Li [17]. It is based on the hypothesis that a crack will grow according to the vector crack tip displacement direction. The vector CTD is represented by the vector summation of the CTOD vector (corresponding to mode I) and the CTSD vector (corresponding to mode II) as seen in Figure 3-2.

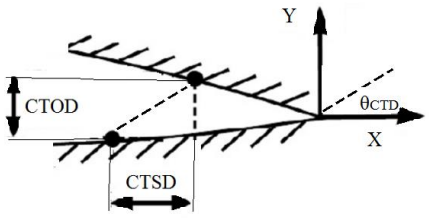

Figure 3-2. Displacements in an open crack, adapted from [17].

The crack is assumed to propagate along the direction of the resultant vector as shown in Eq. (44).

$$\tan\theta_{CTD} = \left[\frac{CTSD}{CTOD}\right] \tag{44}$$

It is possible to replace SIF in Eq. (44) to obtain Eq. (45).

$$\theta_{CTD} = \tan^{-1}\left[\frac{K_{II}}{K_I}\right] \tag{45}$$

This criteria is cited in literature when describing micro crack behavior [73].

It should be highlited that the Schollman et. al. and the SED criteria are the only two models that account for mode III influce in the crack kinking angle.

3.4
Equivalent SIF

When more than one loading is present, it is understood that a corresponding SIF represents the combination of the present loading modes. This section presents the physical principles used by some of the most important models to calculate SIF under mixed mode loading.

3.4.1
Tanaka

Tanaka [74] deducted an equivalent SIF expression by treating displacement as vectors and applying the result to the rigid plastic strip model proposed by Bilby, Cottrell and Swinden. They proposed that crack growth happens when the displacements (or the sum of them) in a strip ahead of the crack tip attains a critical value, and it is a factor of SIF to the 4^{th} power. Later on, Miranda et. al. [75] showed Tanaka´s model could be extended to include out-of plane sliding. The model is shown in Eq. (46), and it was originally tested in a thin Aluminum plate with an inclined-to-stress slit.

$$K_{Tanaka} = \sqrt[4]{K_I{}^4 + 8K_{II}{}^4 + \frac{8K_{III}{}^4}{1-\nu}} \tag{46}$$

3.4.2 Asaro

Pei and Asaro [76] proposed a SIF for in-plane problems of functionally graded materials, treating the SIF as complex quantity, as shown in Eq. (47).

$$K_{eq} = |K| e^{\theta i} \tag{47}$$

where θ is the phase angle as defined by Eq. (48) and |K| is the vector norm as described in Eq. (49) which is the same as the CTD model, Eq. (45).

$$\theta = \tan^{-1} \frac{K_{II}}{K_I} \tag{48}$$

and the magnitude of equivalent SIF is given by Eq. (49).

$$K_{Asaro} = \sqrt{K_I{}^2 + K_{II}{}^2} \tag{49}$$

3.4.3 Pook

L. Pook [77] proposed a criteria based on stress in mode I for a three-point bending test sample with an inclined-to-normal crack.

$$K_{P2D} = \frac{0,83K_I + \sqrt{0,4489K_I{}^2 + 3K_{II}{}^2}}{1,5} \tag{50}$$

Later on [78], the criteria was expanded to include mode III as well.

$$K_{P3D} = \frac{K_I(1+2\nu) + \sqrt{K_I{}^2(1-2\nu)^2 + 4K_{III}{}^2}}{2} \tag{51}$$

3.4.4
Erdogan-Sih

It is based on the maximum MTS criterion [9]. It states that crack growth occurs in the direction which has the maximum tangential stress and a shear stress of zero. It is shown in Eq. (52).

$$K_{ES} = \frac{K_I}{4}\left(3\cos\frac{\theta^*}{2} + \cos\frac{3\theta^*}{2}\right) - \frac{3K_{II}}{4}\left(\sin\frac{\theta^*}{2} + \sin\frac{3\theta^*}{2}\right) \tag{52}$$

The θ^* angle in Eq. (52) is defined in Eq. (32), and another way to find it, is by giving values to θ within an interval and identify the angle that makes K_{ES} maximum.

3.4.5
Schöllmann

In 2002 [19], Schöllmann et. al. proposed a generalized failure criterion for the three opening modes as a function of angular position θ as shown in Eq. (53).

$$K_{S3D} = \frac{1}{2}\cos\left(\frac{\theta}{2}\right)\left[\begin{array}{l} K_I\cos^2\left(\frac{\theta}{2}\right) - \frac{3}{2}K_{II}\sin\theta + \ldots \\ \ldots + \sqrt{\left[K_I\cos^2\left(\frac{\theta}{2}\right) - \frac{3}{2}K_{II}\sin\theta\right]^2 + 4{K_{III}}^2} \end{array}\right] \tag{53}$$

Eq. (53) is implicit as it includes the kinking angle, so it cannot be solved directly. If K_{III} is zero, the Schöllmann et. al. model becomes the ES model.

The extension from monotonic to cyclic loading has been addressed in literature. Several authors state that monotonic loading criteria can be extended to fatigue loading [22, 51, 68, 73, 79, 80]. That means that an equivalent SIF can be replaced by an equivalent SIF range (ΔK) in the aforementioned criteria.

As stated at the beginning, the models mentioned in this chapter are based on a physical principle. They are used to predict the two most important characteristics in fracture mechanics: crack path (angle of crack), and crack growth; when an equivalent SIF surpasses a material property, the crack advances a finite distance. Such prediction could be done with software (usually FEM) which relies in models

like the ones just presented here. In chapter 6 they will be evaluated with the experimentally calculated SIF and SIF ranges determined in chapter 5.

To close this chapter, it can be said that the research community agrees that crack growth has a preference for growing under mode I. However, crack path kinking for non proportional loading is not completely understood yet. Zerres and Vormwald [25] identified seven factors that affect crack growth under non-proportional loading: material's sensitivity to shear dominated fracture, plastic deformation ahead of crack tip, crack closure, the specimen´s geometry, the mean stress, mode mixity, and the variability of mode-mixity. The last two are the main agents responsible for making cracks turn.

4. Materials and Methods

Two set of tests, a Disk Compact Tension sample (DCT) and a modified Compact Test sample C(T), were conducted at the fatigue lab at PUC-Rio by doctoral student Julián Andrés Ortiz González and Dr. Giancarlo Luis Gómez Gonzáles. A second set of experiments, five thin tubes with horizontal slits, were tested at the materials and structures lab at Technische Universität Darmstadt by Prof. Michael Vormwald, Prof. José Luiz de França Freire and doctoral student Yigiter Hos. This section describes the performed tests in order to obtain SIF under mixed mode loading using the DIC technique as well as the procedures used to further process the measured displacement fields.

4.1 Disk Compact Tension (DCT)

A DCT sample made out of AISI-SAE 4340 machined from a 3" round bar heat treated to tempered martensite with 200 Vickers hardness [49] with material composition [5] shown in Table 6, was subjected to pure mode I loading. For the measurements reported here, the coupon had a fatigued grown crack size of 4.7mm, as shown in Figure 4-1a.

Both sample's faces were polished with sand paper, and the sample was primed in white paint and then, black speckles were applied on the polished surface for DIC data acquisition. A traveling optical microscope was placed in the rear to allow crack´s growth optical observation. The sample was mounted

[5] Material composition was obtained with a portable Thermo Scientific ® NITON XL5 XRF analyzer, performed by Mr. Humberto de Matos Andrade from HCG Equipamentos, São Bernardo, SP.

in an INSTRON 8501 universal testing machine equipped with a 100kN load cell. The test set up is shown in Figure 4-1b.

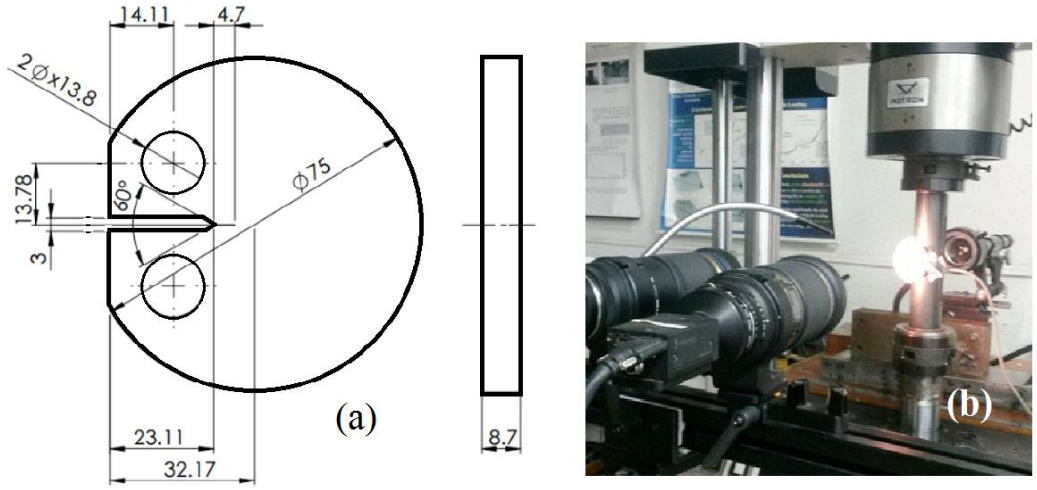

Figure 4-1. DCT coupon dimensions

Table 6. Material composition for DCT sample

Element	Fe	Ni	Cr	Mn	Al	Si	Other
%	95.41	1.76	0.76	0.69	0.25	0.24	0.4

For DIC data acquisition images were recorded using two five megapixel digital cameras (Point Grey GRAS -50S5M with 2448 x 2048 pixels) attached to lenses Tamron ® A031 AF28-200mm F /3.8-5.6, and the applied load was recorded with a NI ® DAQ NI9215 card. Images were processed with 3D VIC ® from Correlated Solutions with a subset size 41 pixels, a step of 15 pixels and a strain window of 15. It was loaded with a quasi-static load up to 14400 N, R=0.1 and $K_{I\,MAX}$ = 34 MPa√m, calculated via ASTM E-399 for plain strain, as shown in Eq. (54). The coupon had undergone previous fatigue crack growth.

$$K_I = \frac{P(2+\frac{a}{W})}{t\sqrt{W}(1-\frac{a}{W})^{3/2}}\left[0,76+4,8\frac{a}{W}-11,58\left(\frac{a}{W}\right)^2+11,43\left(\frac{a}{W}\right)^3-4,08\left(\frac{a}{W}\right)^4\right] \qquad (54)$$

where *t* is sample thickness, *W* is width, *a* is crack length (all of them in m), and P the applied load in N.

For the purpose of validation, numerical simulations were performed in ANSYS using 2 mm hexahedral elements (Solid 185) and 0.25mm quarter-point

elements in a 7 mm radius around the crack edge. There were 59 partitions around the crack front and 6 countours around the crack tip. Details of the mesh are shown in Figure 5-4.

4.2
Modified Compact Tension C(T)

A modified Compact Test C(T) sample was subjected to axial loading. The sample had a drilled hole ahead of the crack front so proportional mode I and II conditions existed. The hole-modified C(T) specimen was made of a low carbon steel, with material composition [6] shown in Table 7; see appendix A for complete results on the optical emission spectroscopy test. After the tests, the sample was subjected to a Nital etching and observed under an optical microscope showing a Ferritic-Perlitic structure. This confirmed the material was indeed a low carbon steel. The sample's lateral faces were polished with sand paper No. 350 to minimize the presence of surface micro cracks and to better visualize the crack path with a traveling optical microscope placed on the back of the specimen.

Table 7. Material composition for modified C(T) sample

Element	Fe	C	Si	Mn	P	S	Other
%	98.9	0.268	0.046	0.68	0.0042	0.025	0.0768

Figure 4-2(a) shows the specimen's dimension where the drilled hole can be observed, and Figure 4-2(b) shows the sample's speckled side mounted in the Instron machine.

[6] Material compostion was obtained with the optical emission spectroscopy techinique according to ASTM A751-2014a

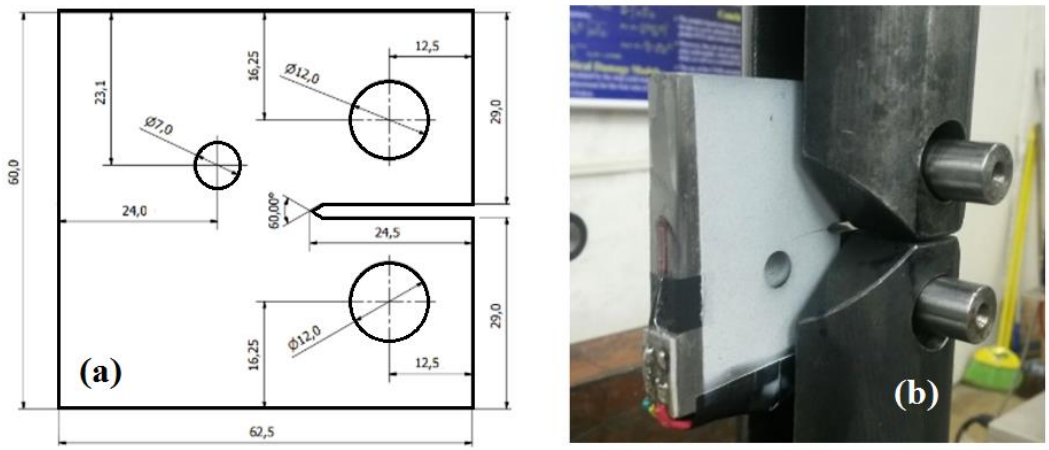

Figure 4-2. (a) Holed CT specimen; (b) Testing set up

The modified C(T) coupon was subjected to a cyclic axial load P, using an INSTRON 8501 universal testing machine equipped with a 100 kN load cell. The crack was propagated via fatigue loading at 10 Hz, and about every 1 mm of crack growth lenght, the load frequency was lowered to 0.1Hz to allow DIC image recording. Figure 4-3 shows the schema used to propagate and to photograph the C(T) sample.

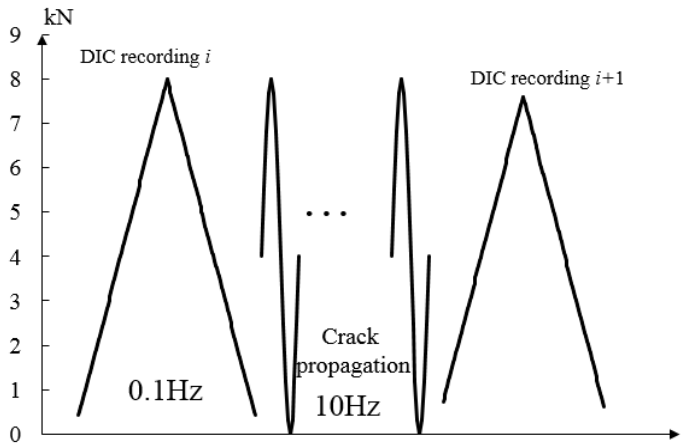

Figure 4-3. Crack propagation and DIC recording loading schema

Even though the drilled hole presence caused mixed-mode conditions, the tests were run under load control adjusting P to keep ΔK_I and K_{MAX} constants (ΔK=22 MPa-m$^{1/2}$ and R=0.1) using ASTM E647-13 as a guide. The applied load was recorded with a NI ® DAQ NI9215 card. The specimen's polished face was primed with white paint and sprayed with random black speckles, according with DIC technique procedures. DIC photographs were taken when the optically-

observed crack-growth increment was about 1 mm. Crack size measurements were directly measured with an optical microscope following the horizontal component of the crack growth in the non-speckled side of the specimen. The loads *P* was synchronously recorded and stored along with the corresponding speckled images. Images were acquired with the 3D-VIC Snap ® software and processed later by the VIC-3D® digital image correlation software, both from Correlated Solutions (Columbia, SC). The 3D DIC system consisted of two 5-MP cameras (Point Grey GRAS-50S5M with 2448 x 2048 pixels) in a stereo configuration equipped with high magnification lenses (Tamron ® A031 AF28-200mm F /3.8-5.6). The DIC analysis was performed using a subset of 25 pixels, step of 6 pixels, and strain window size of 15. The spatial image resolution was of approximately 8.4 μm/pixel.

4.3
Thin tubes

Five thin tubes were subjected to constant amplitude fatigue tests with different combinations of axial load (R_L = -1) and alternated torsion (R_T = -1) [33]. The experiments were conducted at the Materials Mechanics group laboratory from TU Daarmstadt (Daarmstadt, Germany). Some results are published in references [28, 33, 48, 81, 82]. The specimens were machined from longitudinally welded tubes. A horizontal slit, diameter 4 mm and 10 mm (length of an arc measured at the outer surface) between their centers was drilled on the opposite-to-the-longitudinal weld as shown in Figure 4-4. The material was steel S235 with measured mechanical properties as follows: Young's modulus, E = 210GPa, yield strength (0.2% plastic offset), S_y = 378MPa, and ultimate tensile strength S_u = 420MPa [28]. Table 8 presents a summary of the loading combinations.

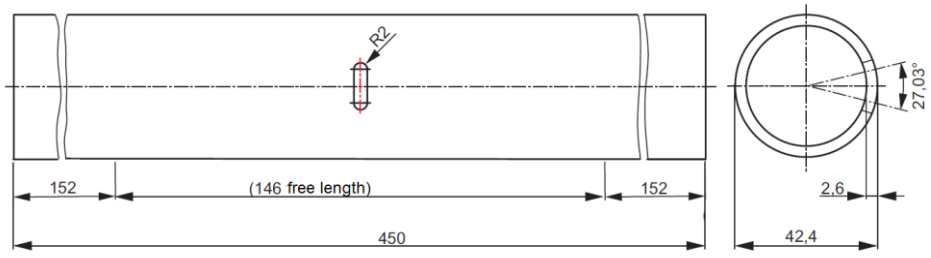

Figure 4-4. Thin tubes, dimensions im mm [33].

The five fully alternated loading combinations were: pure tension-compression (P) loading (R-028 specimen), pure alternated torsion (T) loading (R-029 specimen), proportional loading resulting from the superposition of in-phase axial and torsional loading (R-030 specimen), and out-of-phase loading with phase angles (ϕ) of 90° (R-031 specimen), and 45° (R-033 specimen).

Table 8. Designation and values of fully alternated loading combinations used for testing the thin tubes samples

Specimen	P [kN] Axial load	T [N-m] Torsion load	ϕ phase angle
R-028	± 44	0	-
R-029	0	± 532	-
R-030	± 33	± 382	0
R-031	± 33	± 382	90
R-033	± 33	± 382	45

In Figure 4-5 can be seen one of the samples mounted in the tension-torsion testing machine. The experiments were conducted under axial load control and torsion load control, respectively, using a servo-hydraulic, four-pillar tension-torsion Schenck testing machine with frequency of 2 Hz. Every so often, the load frequency was lowered to 0.1Hz during 3 cycles to allow DIC recording. The machine´s controller was a MTS FlexTest® SE device and temperature at 23°C with a relative humidity of 60% were kept steady throughout all the experiments. Additional experiment details can be found in [33].

Depending on the loading type, two or four cracks, initiating at the notch, were witnessed [48] The cracks were assumed to be through-wall cracks with a straight crack front. Two cameras (Allied Vision Tech ® GT 2450) with resolution: 2448x2050 pixels, equipped with Rodagon ® 1:4 / 80mm lenses, and 3D VIC ® were used for the DIC data image collecting. The actual loads, *P* and T at the instant

of each snapshot (100 shots/cycle of image acquisition) were recorded and stored together with the corresponding pictures. Figure 4-6 shows the applied loads in a force versus torque plot for the five thin tubes as well as the “slow down” procedure used to take the DIC pictures.

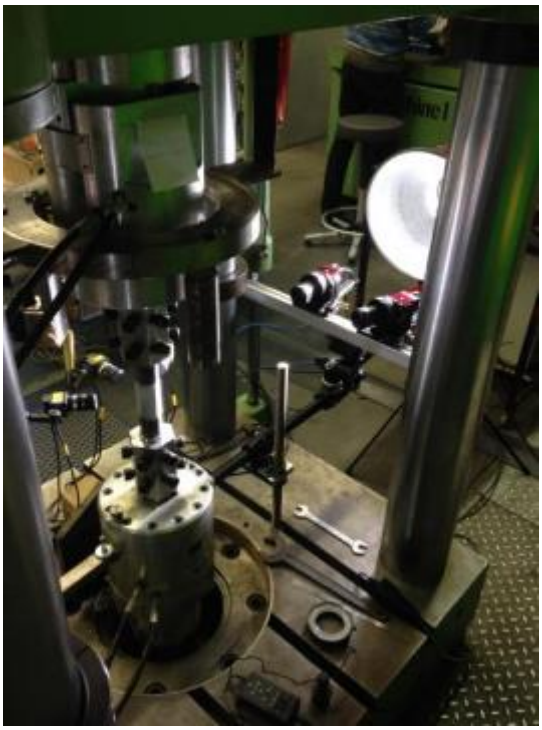

Figure 4-5. Thin tube being tested on the tension-torsion machine [33].

It can be seen in Figure 4-6 (bottom left), the loading frequency was lowered to allow DIC recording during three cycles. These data were acquired at a frequency of 0.1Hz for each crack length at intervals of 400, 500 or 1000 cycles.

4.4
DIC data selection

The area around the crack lips presents a high noise level, which is inherent to the DIC technique. As pointed before, the correlation algorithm identifies the gray intensities best-matching subsets between the reference and the deformed images. When in presence of a crack, the algorithm cannot distinguish crack sides, possibly matching gray intensities from opposite crack edges, therefore, calculating

unrealistic strains that, if used in the analysis, can lead to false readings. Hence, they should be cropped out from the AOI (Area of Inspection) to analyze the DIC acquired data.

Exemplary data for measured displacement fields ,without cropping, is shown in Figure 4-7 a) v, b) w, fields respectively for directions Y, and Z and d) principal strain field, for sample R-030 at 10400 cycles and crack length of 3.66 mm at maximum load, P= 32kN and T=382 N-m in-phase. The axis X (parallel to crack), Y (orthogonal to crack direction) and Z (orthogonal to surface) and respective u, v, and w displacement fiels have been oriented to coincide with the crack propagation angle. Notice there is no data along the crack.

The CTL (Crack Tip Location) must be determined accurately in order to achieve precise results when calculating SIF. At first, the CTL was identified on 3D-VIC by:

1. First of all, remove the rigid body movement of the measurements.
2. The principal strain field shows an extremely high gradient around the crack edges and crack tip, as seen in Figure 4-7d.
3. Location of maximum correlation error *Sx, Sy, Sz* in each direction. Around the crack, these errors are higher because of the discontinuity over the crack lips. When there is a high gradient in such error, most likely the CTL is located there, as seen in Figure 4-7c for the correlation error in the parallel to crack direction.
4. The vertical displacement, v, goes from positive to negative when crossing crack edges. If one moves axially going to the CTL, there is a point where such gradient stops, as seen in Figure 4-7a. Most likely, that is the CTL. Such procedure is reported in literature [45, 67]
5. The out-of-plane displacement, w, presents a zone with a high gradient ahead of the CTL (seen in Figure 4-7b), as documented by Kotousov [47].

With a pre-identified CTL in the 3D VIC system, the data was fed to an algorithm [49] which fit displacement fields to the Westergaard's stress function. A refined grid was used to pinpoint more accurately the CTL by minimizing the error

between the experimental displacements and the fitted displacements. Such error was arbitrarily set to 0.05 mm.

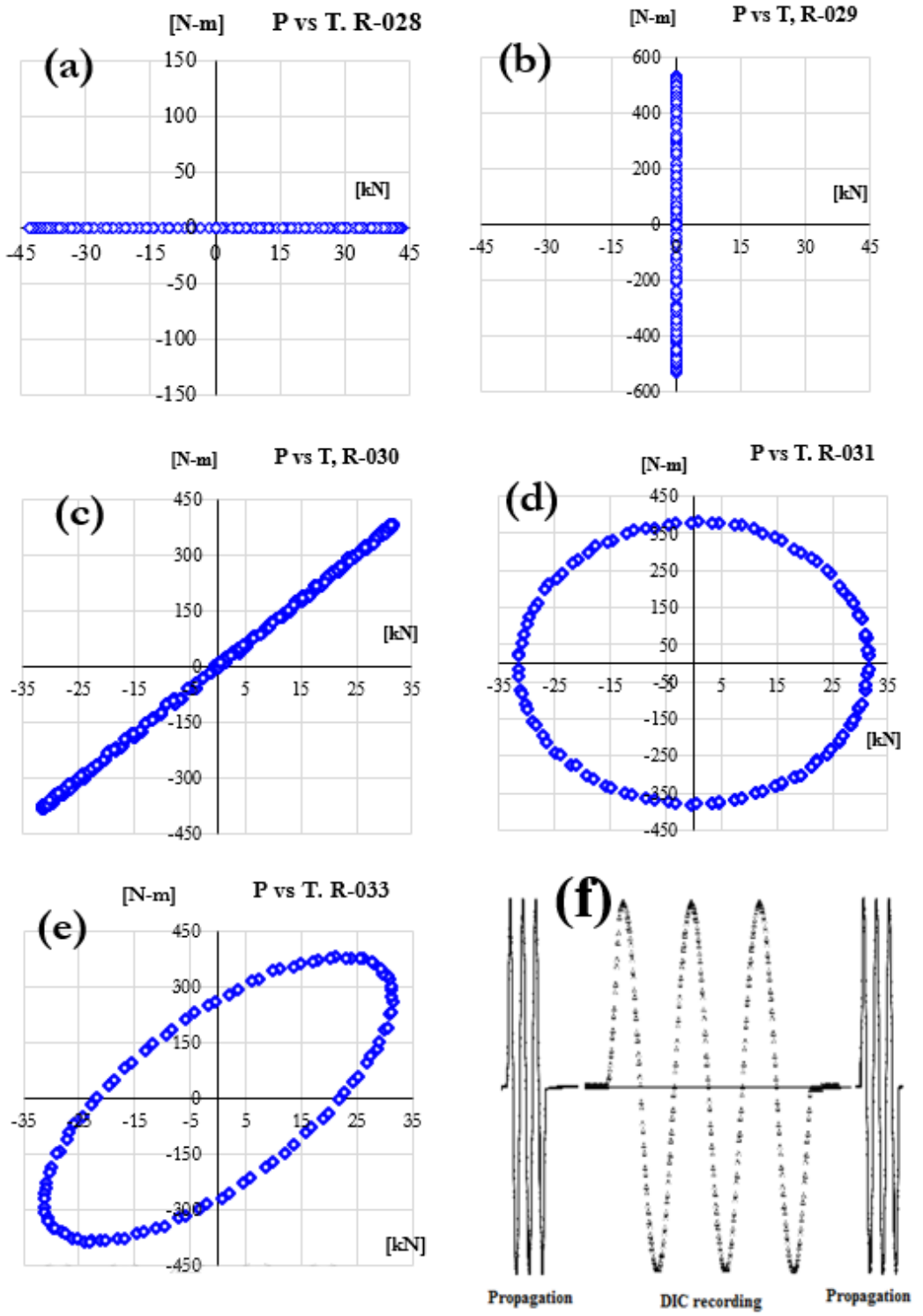

Figure 4-6. Applied loads for thin tubes. a) R-028, b) R-029, c) R-030, d) R-031, e) R-033 and e) procedure for recording DIC pictures.

In the thin tubes, the data for the COD method using Eq. (7) was taken between one and two millimeters behind the crack tip to minimize the error due to the cylinder's curvature when approximating an arc length with a straight line formed between the CTL and the chosen points, as seen in Figure 4-8b. That distance also, ensures the reading are out of the plastic zone. In the DCT and C(T) samples, as they can be treated as a plate, displacement data was taken parallel to the crack lines. In section 5.1 is shown and explained the importance of choosing carefully the data points to extract displacement data.

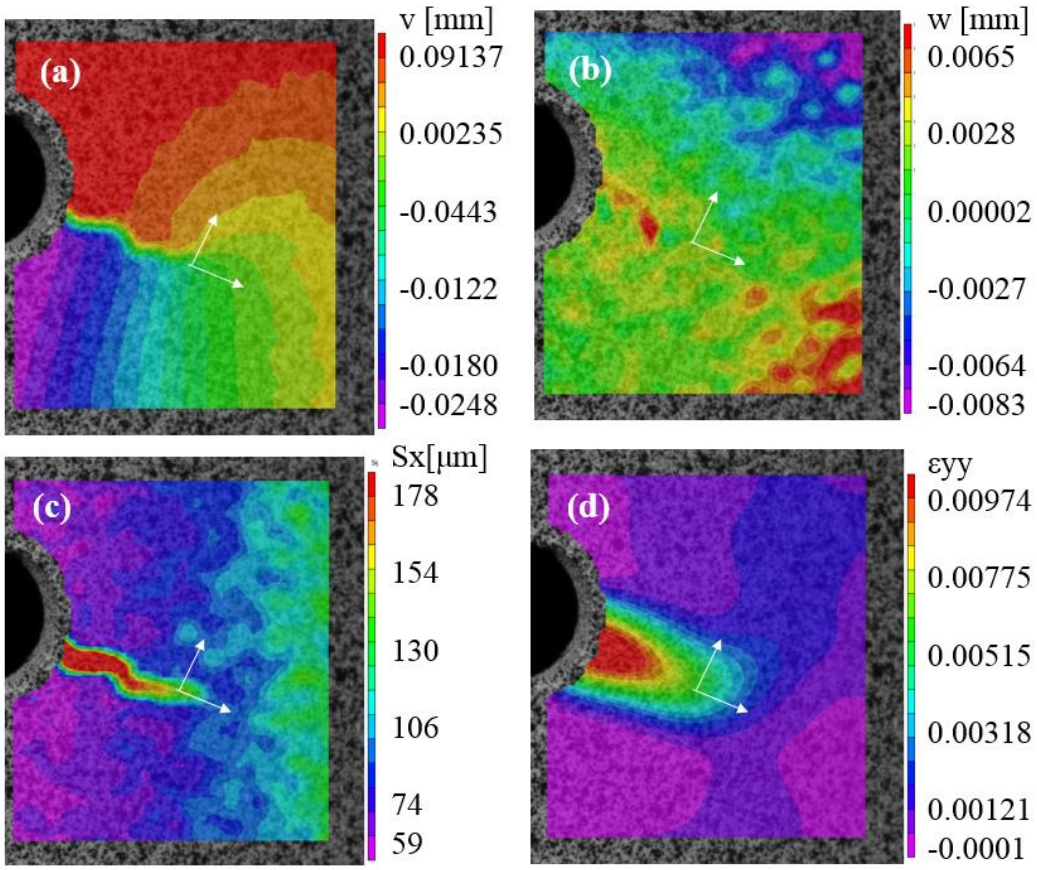

Figure 4-7. Exemplary results for DIC displacement data for sample R-030 at 10400 cycles, crack length of 3.66 mm, a) v, b) w, c) parallel to crack error, and d) principal strain fields.

For the LSM method, shown in Eq. (5), the area close to the crack lips and ahead of the crack tip was cropped out to avoid the noise mentioned previously.

The method used data from behind and ahead of the crack tip. For CTL, all the field was used.

Finally, displacement field data was exported to be further processed in a Matlab® routine [49] to calculate mixed mode SIFs values. It has to be highlighted here that in order to comply with Williams expansion series, Figure 2-2 and Eq. (5), the displacement data was rotated to coincide with the crack´s edges; this is crack the edges were parallel to the X axis.

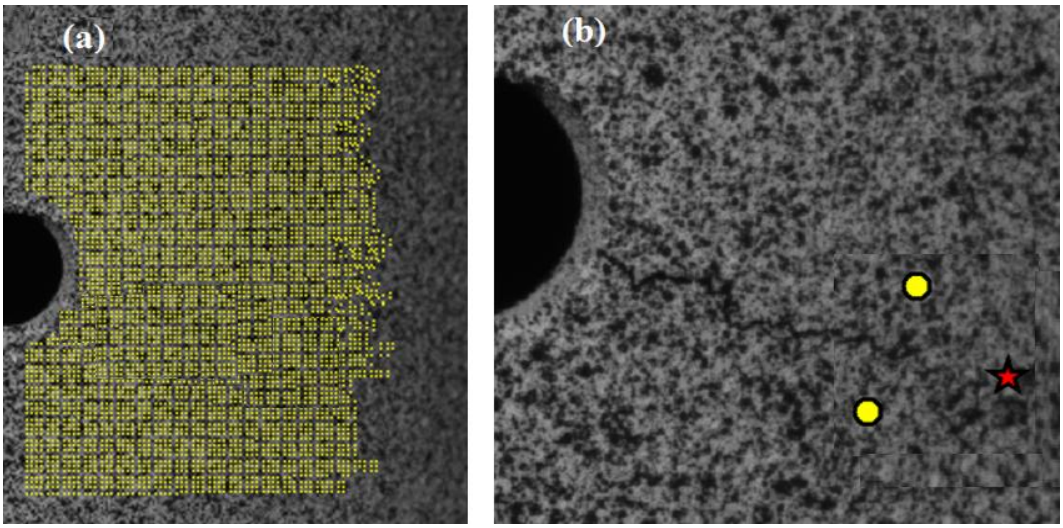

Figure 4-8 .Exemplary data for thin tubes (R-030 specimen after 10400 cycles and crack length of 3.66 mm) at maximum loads, a) data used for CTL and b) location of points used for COD method.

4.5
Evaluation of SIF and SIF ranges

The equivalent SIF models presented in section 3.4, strictly speaking apply for monotonic proportional loading. However, several authors [51, 68, 73, 83] suggest they can be extended to alternating proportional loading. In other words, SIF becomes SIF range. There are two models that include the crack kinking angle in their formulation: the ES SIF equivalent model presented in Eq. (52), and Schöllmann et. al. equivalent SIF model described by Eq. (53). Therefore, the equivalent ES SIF range is described by Eq. (55).

$$\Delta K_{ES} = \frac{\Delta K_I}{4}\left(3\cos\frac{\theta^*}{2} + \cos\frac{3\theta^*}{2}\right) - \frac{3\Delta K_{II}}{4}\left(\sin\frac{\theta^*}{2} + \sin\frac{3\theta^*}{2}\right) \quad (55)$$

whereas, the Schöllmann et. al. SIF range is described by Eq. (56).

$$\Delta K_{S3D} = \frac{1}{2}\cos\left(\frac{\theta}{2}\right)\left[\begin{array}{l}\Delta K_I \cos^2\left(\frac{\theta}{2}\right) - \frac{3}{2}\Delta K_{II}\sin\theta + \ldots \\ \ldots + \sqrt{\left[\Delta K_I \cos^2\left(\frac{\theta}{2}\right) - \frac{3}{2}\Delta K_{II}\sin\theta\right]^2 + 4\Delta K_{III}{}^2}\end{array}\right] \quad (56)$$

Eq. (55) and Eq. (56) can be used straightforward as long as the mixed-mode SIF ratios do not change inside a loading cycle. Therefore, for non-proportional loading is necessary to find the θ^* which maximizes ΔK_{ES} and ΔK_{S3D}. So next, it is presented how Eq. (55) and Eq. (56) are used to extract the crack kinking angle from the assumption [51, 68, 73, 83] that SIF is exchangeable with SIF range.

To find the θ^* angle in the ΔK_{ES}, Eq. (55), there were given values to θ within an interval to identify the angle that made K_{ES} maximum along one mixed-mode loading cycle. The procedure can be graphically summarized in Figure 4-9, as follows. For each ***j*** row (load), the maximum and minimum values of $K_{ES(\theta)}$ were extracted when θ was varied from -75 to +75º. Then, the respective θ at which $\Delta K_{ES(\theta)\ MAX}$ occurs was identified. So, the equivalent ES SIF range was adopted by subtracting the maximum from the minimum found SIF.

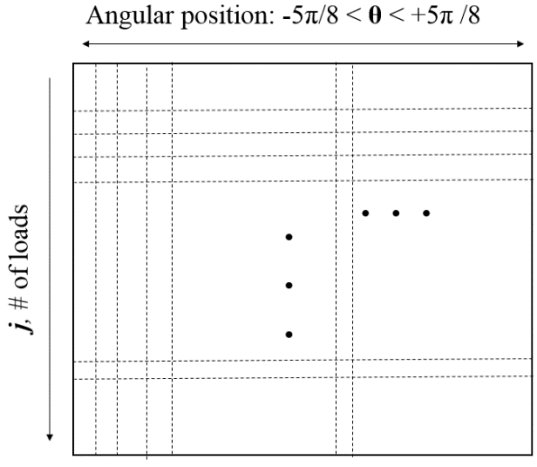

Figure 4-9. Schema to evaluate $K_{ES(\theta)}$

Conversely, the Schöllmann et. al. equivalent SIF model, ΔK_{S3D} Eq. (56), is not explicit. The square root term makes all terms positive allocating them in the

first quadrant of a Cartesian plane. Therefore, calculating ΔK_{S3D} by direct evaluation of Eq. (56) may lead to smaller amplitudes due to possible negative K_{II} values. However, K_{S3D}, Eq. (53), can be evaluated by rewriting it as Eq. (57), which for the case of negative K_{II} loading situations, it will keep the sign.

$$K_{S3D} = \frac{1}{2}\cos\left(\frac{\theta}{2}\right)\left\{X_j + \sqrt{X_j^{\,2} + (2Y_j)^2}\right\}$$
$$X_j = K_I \cos^2\left(\frac{\theta}{2}\right) - \frac{3}{2}K_{II}\sin\theta \qquad (57)$$
$$Y_j = K_{III}$$

Then, Eq. (57) is plotted in a Cartesian plane representing the X_j and Y_j quantities for any triple of SIFs I, II and III at any time as seen in Figure 4-10. To find the maximum range, one needs to find the maximum distance (ΔK_{S3D}) between any two points, namely $K_{S3D\text{-}p}$ for point *p*, and $K_{S3D\text{-}q}$ for point *q* as seen in Figure 4-10. In other words, subtraction of the vectors representing instant *p* and *q* for a trial angle gives the vector range ΔXY, and its algebraic addition to ($X_p - X_q$) results in the equivalent range $\Delta K_{S3Dp,j}$ as shown in Eq. (58).

$$\Delta K_{S3D\,p,q} = \left(X_p - X_q\right) + \sqrt{\left(X_p - X_q\right)^2 + \left(Y_p - Y_q\right)^2} \qquad (58)$$

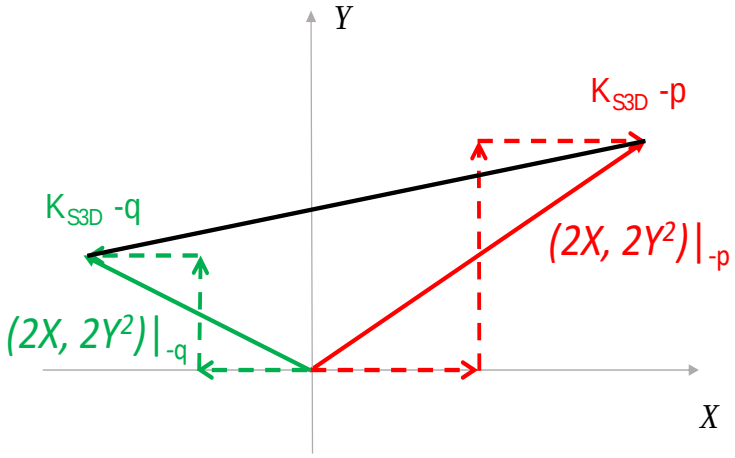

Figure 4-10. Explanation of graphic schema to evaluate K_{S3D} and ΔK_{S3D}.

The representative equivalent SIF range for the cycle is the result for the maximum value of $\Delta K_{S3Dp,q}$, after the entire θ range (-75 to +75º) is been swept.

Such procedure finds not only the maximum ΔK_{S3D} value, but also the crack kinking angle at which it occurs.

4.6 Evaluation of crack kinking models

This section presents how the described crack kinking models were evaluated. It has to be noted that despite the models mentioned in section 3.1 to 3.3 use SIF (monotonic load), in literature [22, 48] is found that an exchange between SIF and SIF ranges, for proportional load, is assumed valid.

The crack kinking models in sections 3.1 and 3.2 are explicit. Therefore, they were evaluated directly as follows. For the modified C(T) specimen, the models were evaluated with maximum SIF at each crack length (a pair of SIFs), whereas for the thin tubes the models were evaluated using all the measured SIF ranges during each measured crack length (concurrent triplets of SIFs). Therefore, Eqs. (32), (34), (35), and (38), (43), and (45) were evaluated directly. This process furnished an angle value with respect to the crack axis. The reported value here is with reference to an axis perpendicular to the axial load.

On the other hand, the crack kinking models in section 3.2, Eqs. (39), (41) and (42) are implicit. So that, a schema similar to the one presented in Figure 4-9 was followed. For each pair of SIFs (modified C(T) specimen) or triplet of SIFs (thin tubes), θ was varied from -75 to +75º plotted, and picked the value that produced the minimum SED, the maximum MEER, and the maximum MTSN accordingly. Then, the respective θ at which said parameter occurs was identified. Such approach was used in [48] to evaluate crack propagation under non-proportional loading.

Because of the influence on SED criterion evaluation, a note on Ψ has to be explained here. Table 9 presents the observed values for Ψ used in the SED criterion, Eq. (39).

Table 9. Observed out-of-plane (Ψ) angle

Specimen	C(T)	R-029	R-030	R-031	R-033
Observed Ψ	0	0	0	20	0

The presented Ψ values correspond to the angle initially formed at the slit inner surface, which is the only observable angle. An example of this is shown in Figure 5-43a where a Ψ value of approximately 20^o is seen.

This chapter presented the experiments performed detailing materials, geometries and loading characteristics. On top of that, the course of action to process the displacement fields before LEFM data fitting was also described, along with the schemas used to evaluate crack kinking models from the SIF and SIF range results.

5. Results

This chapter presents SIF, SIF range, and equivalent SIF range results for the DCT, holed C(T), and the five loading cases for the thin tubes.

5.1 DCT

DCT coupons with a/W= 0.25 and a crack size of 4.7mm, were tested under a quasi-static mode I load up to 14400 N with an applied K_I max of 34 MPa$\sqrt{m}$, calculated via ASTM E-399 as shown in Eq. (54), with a R=0.1 until the crack was about 0.1 mm, when the loading frequency was adjusted to 20Hz. So, the sample underwent fatigue crack growth. DIC displacement data was taken on 101 points along two lines parallel to the crack edge. The location of such points are plotted over the perpendicular-to-crack displacement field as seen in Figure 5-1c. Figure 5-1b shows the variation of K_I, using the COD method or Eq. (6), with horizontal distance measured from the CTL. It can be seen how, in this case, K_I stabilizes after about 1.5 mm. That variation is attributed to the fact that points closer than 1.5 mm to the CTL do not fit the $\pm\pi$ angular position with respect to the CTL as it is assumed in the COD simplification, Eq. (6). Another deviation is seen after 3.0 mm aprox. As one can see in Figure 5-1b, the crack is not completely straight, which makes the drafted lines not simetric with the crack edges.

Additionally, Williams' solution for displacement was fitted to experimental data using the LSM, or Eq. (16). First, it was calculated the influence of *n-terms* on K_I results by varying the number of terms in Williams' expansion for displacement evaluated at maximum load. This analysis, of course, depends on how far from the CTL the data is from.

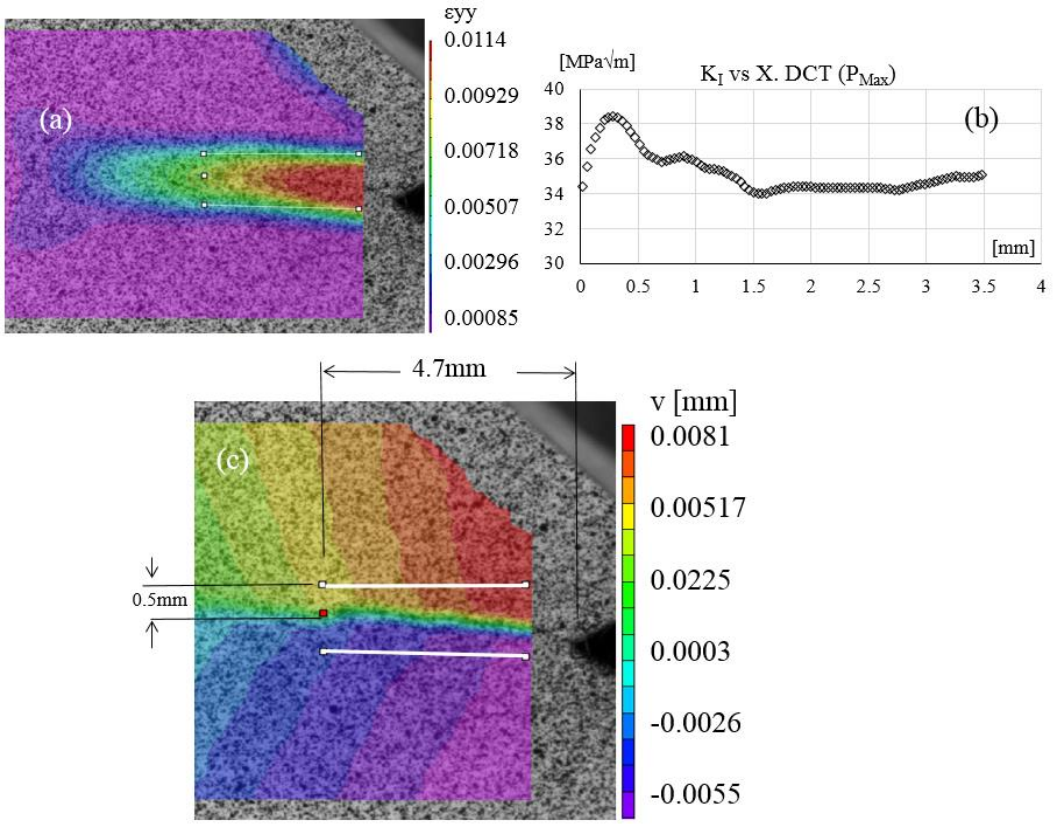

Figure 5-1. a) Perpendicular-to-crack strain; b) K_I vs. horizontal distance from CTL via COD, c) Perpendicular-to-crack displacement field on DCT sample.

The input data, for the results in Figure 5-2, was the yellow square with an internal lenght of 2 mm, as shown in Figure 5-3. Results, shown in Figure 5-2, agree with literature [84, 85] on the number of converging terms.

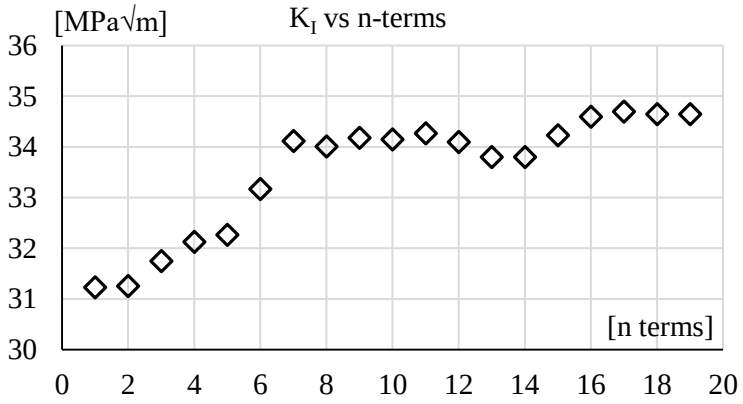

Figure 5-2. K_I variation with number of terms in Williams's expansion

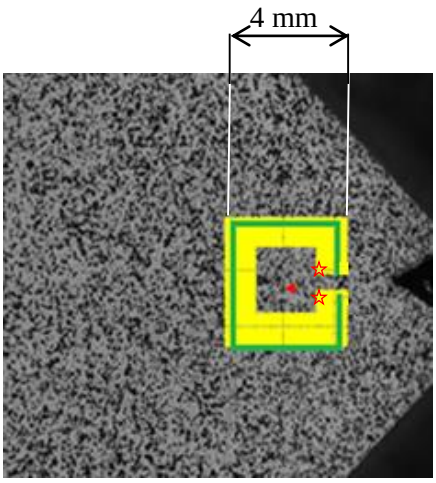

Figure 5-3. Path, points, and area used to extract data for K_I for DCT sample

To validate SIF calculations, results were compared to FEM simulations performed with ANSYS using a mesh as described in section 4.1, and depicted in Figure 5-4 where the first countour around CTL can be seen in detail.

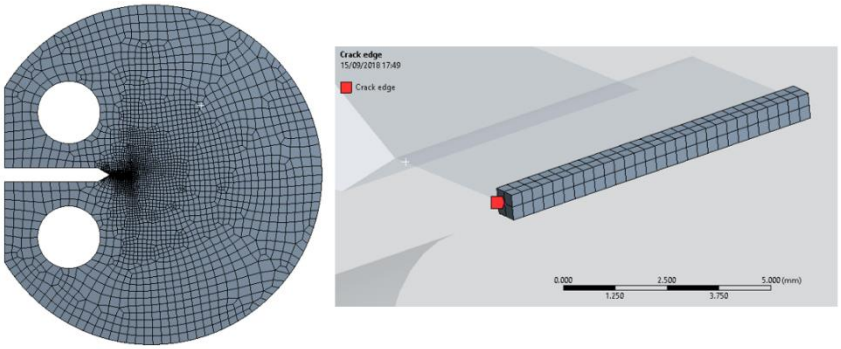

Figure 5-4. General view and zoom of first countour around CTL of DCT sample´s mesh

Figure 5-5 shows the comparison of K_I against applied force P. K_I values were obtained with the LSM shown in Eq. (16), ⌡ shown in Eq. (10), and COD shown in Eq. (6) methods, ASTM values with Eq. (54) and FEM results. For DIC data LSM, ⌡ and COD, the input data was the yellow square with an internal lenght of 2 mm, the rectangular path (about 4 mm in lenght) around the 4.7 mm crack, and an example of a pair of points (hollow stars) behind the CTL, as shown in Figure 5-3.

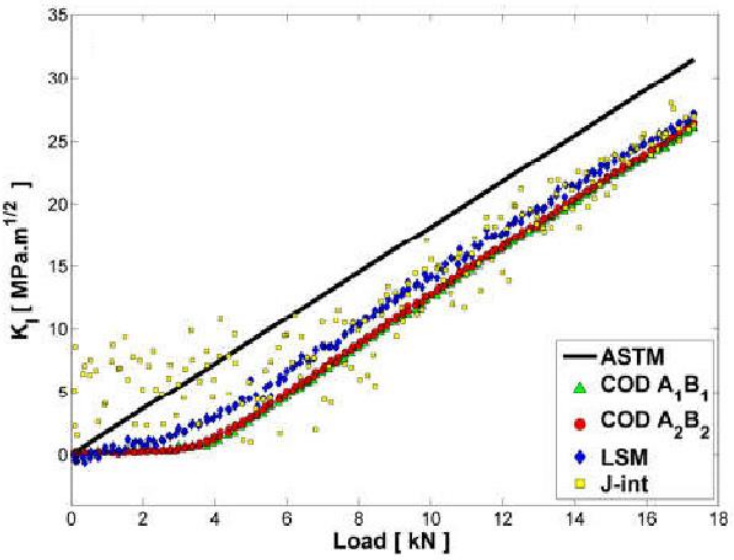

Figure 5-5. Comparison of K_I from DIC (COD and LSM), and ASTM values for DCT sample [49].

The crack closure phenomena can be seen clearly in the DIC measured curve (COD and LSM) in Figure 5-5 as indicated by the arrow in the horizontal axis. It should be noted from the plot in Figure 5-5 that the crack stays pretty much closed, albeit there is a positive applied load, until about 3.8 kN for LSM and COD methods when the crack opens and the SIF starts showing positive values. This is expected due to the residual deformation the sample experienced during previous fatigue crack growth. Crack closure results obtained here agree with similar studies using DIC [86, 87] and other studies using the TSA technique [88]. In addition, this pseudo-K_I should be interpreted carefully as a sum of elastic and plastic SIF [86, 89] SIF as non linear phenomena such crack closure and blunting are present [49].

Moreover, values for ⌡ were calculated for a rectangular path around the crack tip, as depicted in the green dashed path of Figure 5-3. Because there were linear elastic conditions along the selected path, K_I is computed with the elastic relation between ⌡ and SIF ($J=K_I^2/E$). Figure 5-6 shows the comparison of ⌡ values for DIC, ANSYS and ASTM. The *J teor* value uses the K_I value calculated via ASTM E-399 for plain strain, as shown in Eq. (54). The presented *J ANSYS* value is taken from the surface in the same numerical simulation used to calculate K_I, whereas ⌡ is the experimental value obtained with Eq. (10). One can see how the values agree after the crack is open, about 6kN. However, one has be carefull when

interpreting ⌡ DIC results. At low loads, the crack is not open, therefore the physical phenomena cannot be described by experimental ⌡ values whereas the numerical simulation assumes the crack is always open.

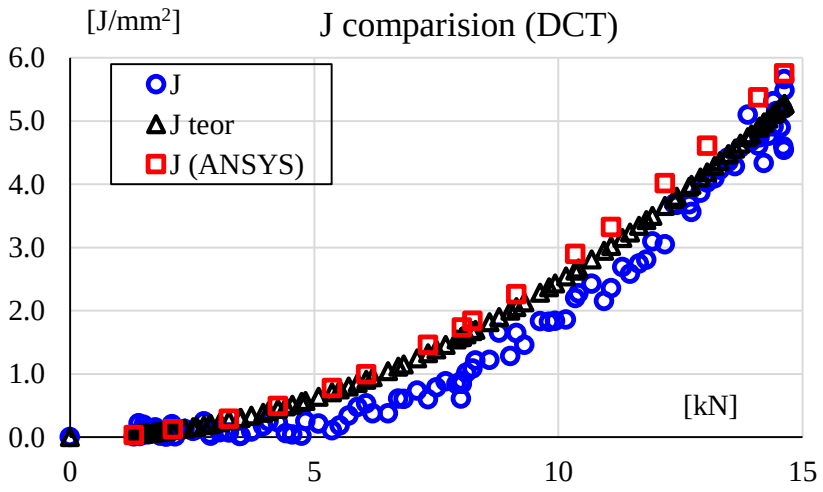

Figure 5-6. Comparison of ⌡ for DIC, FEM and ASTM values.

In this section, it was shown a comparison of SIF experimentally obtained with the COD, LSM and ⌡ methods. The COD and LSM methods are validated, see Figure 5-5 and Figure 5-6, as the values for COD and LSM coincide with original numerical simulations, ASTM values and ⌡ calculations. It was also verified how the crack closure phenomena observed by Elber was present in the sample as measured by the DIC technique using LEFM formulations. The offset between numerical and experimental values is attributed to the crack closure phenomena.

5.2
Holed C(T)

The modified C(T) specimen initially grew a horizontal crack, which later curved due to the influence of the drilled hole. SIFs were calculated at total crack lengths of 2.1, 4.1, 6.3, 8.2, 10.2, and 11.9 mm, named 0, a, b, c, d, and e respectively, with location depicted in Figure 5-7. Those six crack lengths were used to collect data to perform SIF evaluation.

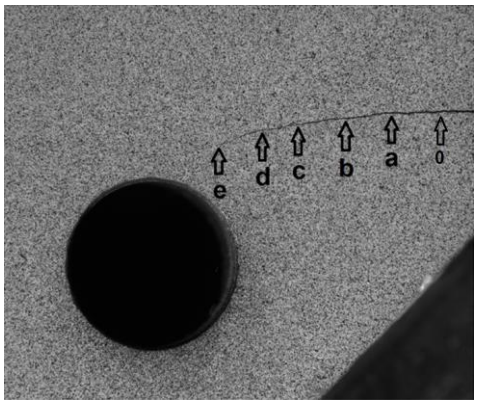

Figure 5-7. Location of the six measured points for the C(T) sample

Figure 5-8a depicts v-component of the displacement field for a crack length of 4.1 mm at maximum applied load where only mode I is expected to influence on the crack. It can be seen that the displacements are perpendicular to the crack faces corresponding to the opening mode. Figure 5-8b depicts u-component of the displacement field at maximum applied load for a crack length of 11.85 mm. In this situation mode I and also mode II are expected. It is observed that the displacements were oriented in such way that they are normal to the crack edge and parallel to the crack faces corresponding to the opening and sliding mode, respectively.

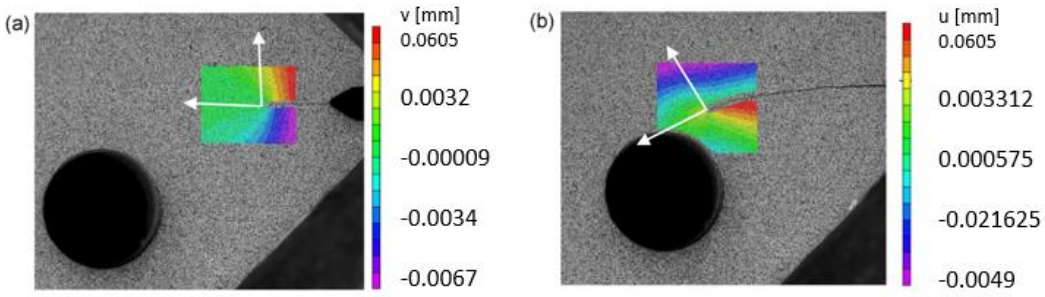

Figure 5-8. Exemplary results of measured displacement fields via DIC: a) Vertical displacement field for total crack length of 4.1 mm b) Horizontal displacement field for total crack length of 11.9 mm.

Moreover, Figure 5-9a (for total crack length of 4.1mm) and Figure 5-9b (for total crack length of 11.85 mm) depict the expected plastic butterfly-like strain field ahead of the crack tip at maximum applied load, where the highest strain values are found.

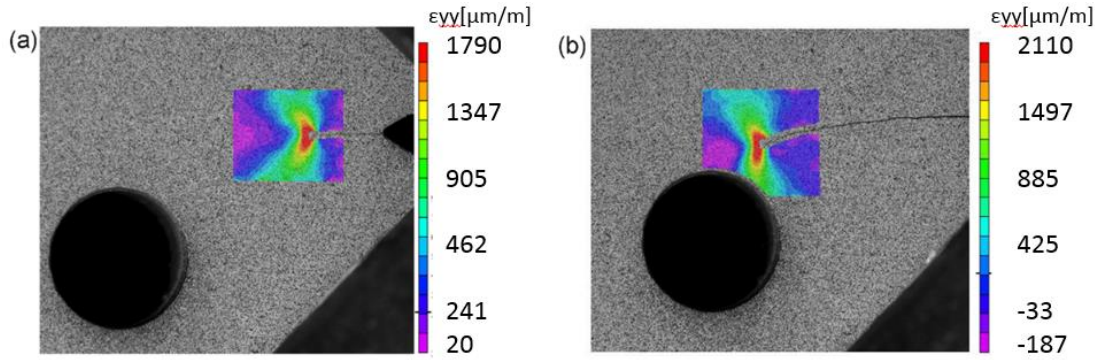

Figure 5-9. Exemplary results for measured strain distribution via DIC on the perpendicular-to-the-crack direction for: a) total crack length of 4.1 mm b) total crack length of 11.9 mm.

For the COD method, as shown in Eq. (7), the symmetrical points were located starting at a distance of about 1 mm behind the crack tip and at about ±0.5 mm from the crack faces to avoid the high noise level resulting from abrupt changes in displacement when the crack opens and closes during the fatigue loading. Figure 5-10 a, b, and c depict the CTL (represented by a red star) and four data points used in the COD method for 4.1, 8.2 mm, and 11.86 mm crack lengths respectively.

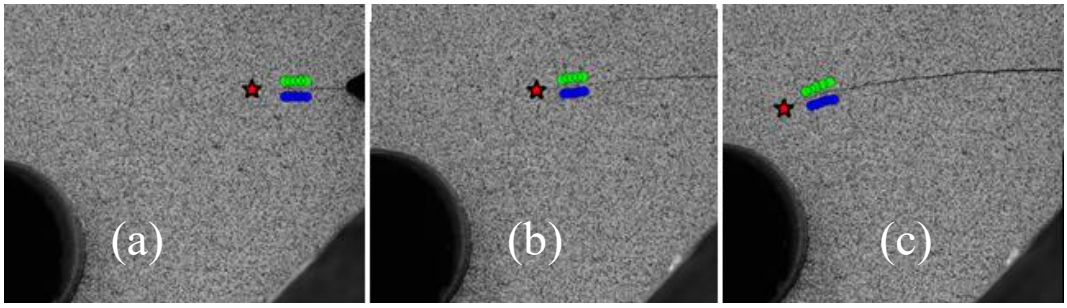

Figure 5-10. Exemplary data used for COD-LSM for crack length (a) 4.1 mm, b) 8.2 mm, c) 11.86 mm.π

In Figure 5-11a, b, and c are shown the areas of inspection used for acquisition of data to apply the over-deterministic LSM formulation, as shown in Eq. (16), for 4.1, 8.2 mm, and 11.86 mm crack lengths respectively along with their CTL represented by a red star. In order to avoid the intensively non-linear behavior ahead of the crack tip and around the crack edges, those data points were excluded from the DIC analyses. Notice that in order to comply with Williams' equations, the

displacement fields u and v were rotated to coincide with the crack propagation angle.

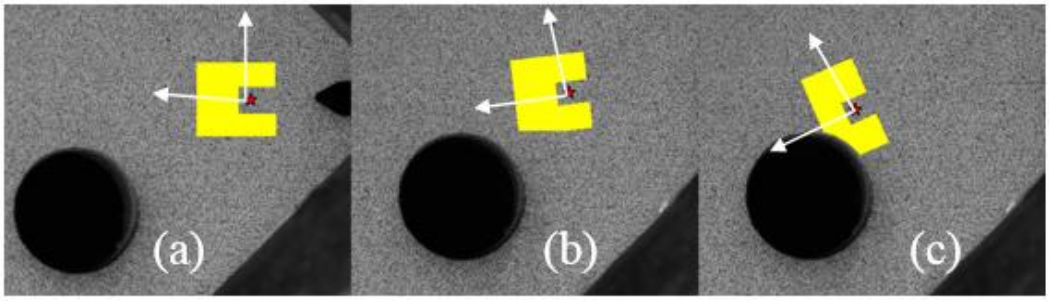

Figure 5-11. Exemplary displacement data used for LSM method a) 4.1 mm, b) 8.2 mm, c) 11.86 mm

In a similar manner to the DCT sample, a 3D finite element analysis was performed using the Autodesk Simulation Multiphysics ® software, performed by doctoral student Julian Andrés Ortiz González. The material properties were assumed to be linear isotropic. The mesh used was about 3 mm tetragonal, and tetrahedral elements in the general body, whereas a mesh refinement was made around the crack tip in a 10 mm radius, with quarter-point elements of approximately 0.37 mm. Figure 5-12 shows results for the parallel-to-load stress field for a 10.2mm crack length.

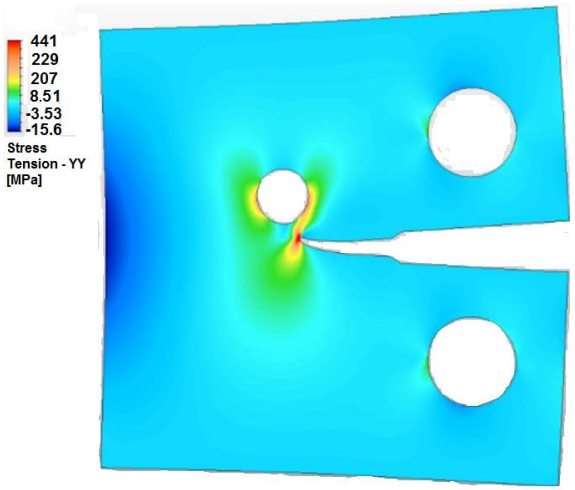

Figure 5-12. Modified C(T)´s FEM parallel-to-load stress field for a 10.2 mm crack

A Matlab® routine [49, 82] was used to obtain the SIF values using the two approaches from experimentally acquiered DIC displacement data. From Figure 5-13 through Figure 5-18, it can be seen a comparison of SIFs values obtained from COD, LSM and FEA simulations performed at total crack lengths of 2.1 mm, 4.1 mm, 6.3 mm, 8.2 mm, 10.2 mm and 11.9 mm, respectively. Both experimental methods (COD and LSM) show very close behavior. The ⌡ method was not used in this sample for two reasons: the rotated fields made the shifted path (as described in Figure 2-5) overlap with one another generating random results. Additionally, and as mentioned in section 2.4, under mixed-mode loading, ⌡ is the result of the contribution of each mode. A method to separate them, as suggested in [60, 61], needs to be implemented.

It can be seen in Figure 5-13, for a 2.1 mm straight crack, that the K_I values exhibit a nonlinear behavior at low loads, which is compatible with crack closure as identified by Elber [3]. For FCG at low load ratios (R = 0.1 in this case), crack closure is expected to be visible. This phenomenon causes an offset between the FEM simulation and the experimental SIF values. It is understood that the FEM simulation assumes that the crack is fully open at any point, neglecting the non-linear effects induced by crack closure and crack rugosity. The crack faces start to open at about 0.27 P/P_{MAX}. Additionally, it is observed that the K_{II} values are zero for FEM and near-to-zero for experimental data, as the crack is straight, and it still is away from the stress concentration region induced by the drilled hole. A very similar behavior, showing crack closure, an offset with the FEM results and K_{II} non-existent, but this time with larger SIF values, is seen in Figure 5-14 for a 4.1 mm crack length.

Although the crack has turned about 5 degrees, similar results - as the two previous points - are still observed in Figure 5-15 for a crack length of 6.3 mm. K_I follows the same line while loading and unloading. However, at low loads, it shows a smaller slant than at bigger loads. The crack starts to open at about 0.2 P/P_{MAX}. As the crack propagates, it grows towards to the hole staring to curve its path.

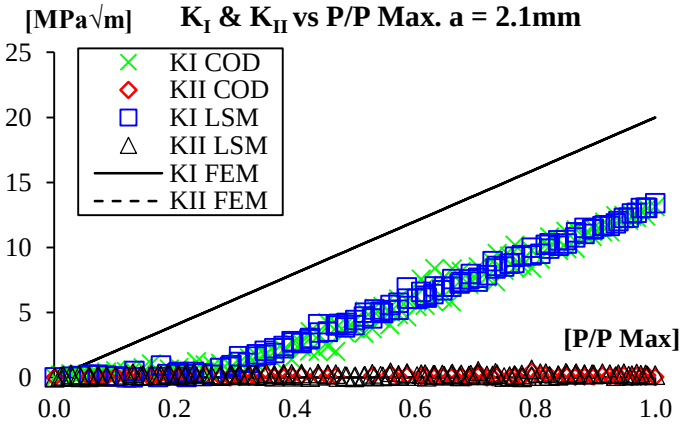

Figure 5-13. SIF for a 2.1 mm crack on modified C(T) specimen

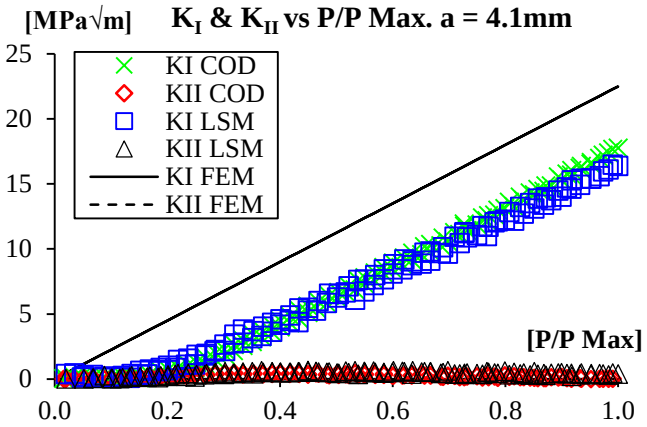

Figure 5-14. SIF for a 4.1 mm crack on modified C(T) specimen

In Figure 5-16, it is seen that K_{II} values are slightly different from zero, but the crack closure phenomenon is still visible. The offset between experimental and FEM results is still clearly visible. It is seen the crack faces start to open at about 0.15 P/P_{MAX}. Note that the maximum K_I value clearly increases with crack length increase.

In Figure 5-17 (total of 10.2 mm crack length), the crack has turned 7º and the crack closure phenomenon can be observed in the non-linear behavior displayed by K_I, measured by both COD-LSM and LSM methods. The crack starts to open at about 0.1 P/P_{MAX}. However, the offset with FEM becomes smaller than in the previously measured points, and K_{II} values are now clearly different from zero. It can also be seen that for K_I, the loadin up and loading down routes follow a slightly different path.

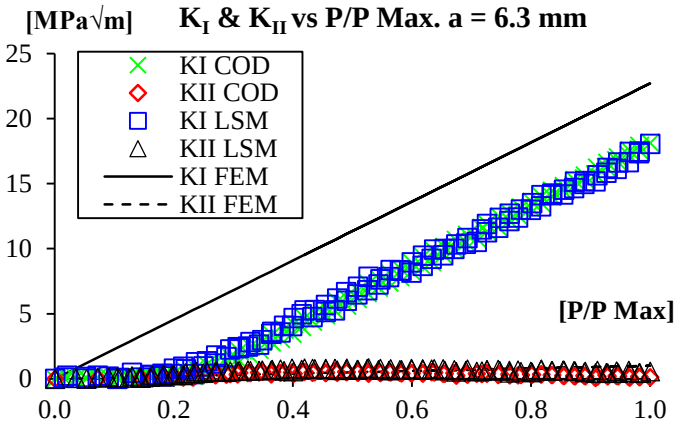

Figure 5-15. SIF for a 6.3 mm crack on modified C(T) specimen

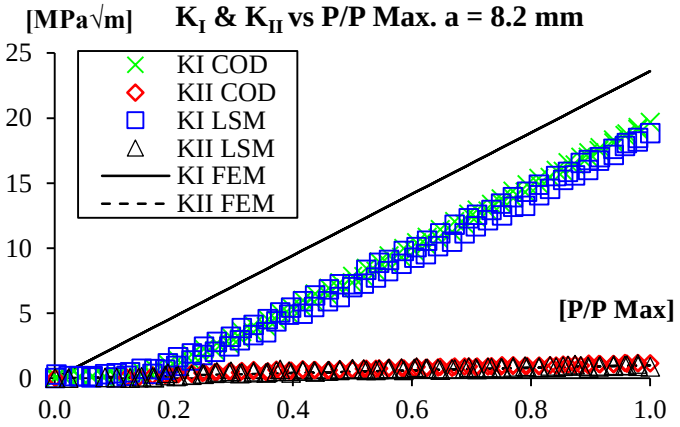

Figure 5-16. SIF for an 8.2 mm crack on modified C(T) specimen

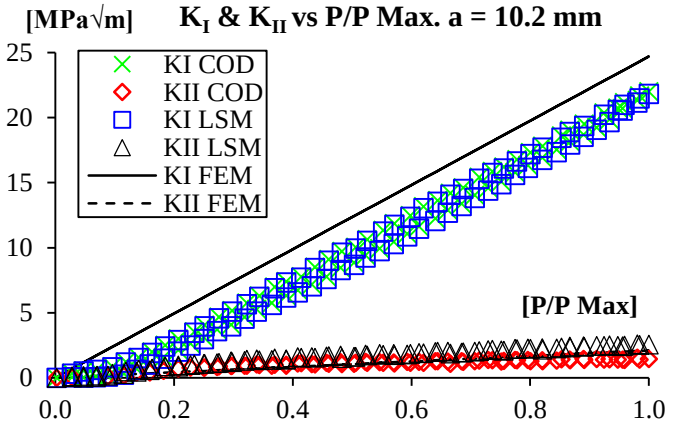

Figure 5-17. SIF for a 10.2 mm crack on modified C(T) specimen

In Figure 5-18a (total of 11.9 mm crack length), the crack has turned about 24º, and the K_I curve shows a nonlinear behavior as it does not follow the same path when opening and closing the crack. This could be an indicator that there is blunting as the crack stays open when the load is dropping. Additionally, there is no evidence of crack closure, therefore the K_I values agreed with the FEM simulation values. Moreover, K_{II} values are larger than those previously measured. At this point, there is a clearly visible mixed-mode SIF (K_{II} and K_I) under which the crack grows. K_{II} presence, different than zero and the asymmetric stress conditions produced by the stress concentration factor caused by the drilled hole, would - at least partially - explain the crack kinking seen in the experiment. Also, in Figure 5-18b is seen the crack opening displacement parallel (COD-x), and crack opening displacement perperdicular (COD-y) to the crack, which were taken at about 2 mm before the CTL, where one can clearly see the proportionality between SIF and COD.

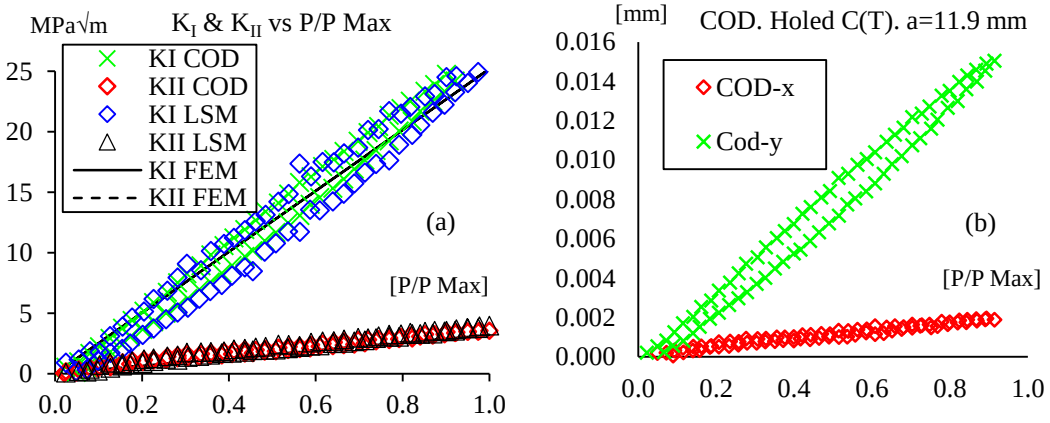

Figure 5-18. Results for 11.9 mm crack on modified C(T) specimen. a) SIF modes I and II obtained with differente methods b) COD

Figure 5-19 presents a comparison of mode II versus normalized load for three different crack lengths (8.2, 10.2 and 11.9 mm). Just like in mode I, there is visible change of slope in K_{II} around the opening load seen for K_I. This could be explained by the fact that when the crack is closed, or partially closed, its faces are still in contact making crack roughness, and interlocking, interfere with mode II (in plane sliding mode), as suggested in [90] [51] , so there is needed a bigger K_{II} before the crack opens. Particularly Kibey et. al. [90] affirmed that slanted cracks may

have the capacity to propagate in mode II, although crack lips are in contact, due to complete slip. In such case, mode I is not the only source of crack growth, which would, at least partially, explain the deviation from a straight path seen in this test. Moreover, Tong et. al. [91] admited that due to the nature of actual crack roughness surfaces, and ideal SIF mode II cannot be seen because wedging interferes with crack opening possibly augmenting mode I, whereas friction impacts crack sliding, weakening mode II SIF development. The previous discussion is supported by the crack models presented in section 3 and developed in section 6.3.

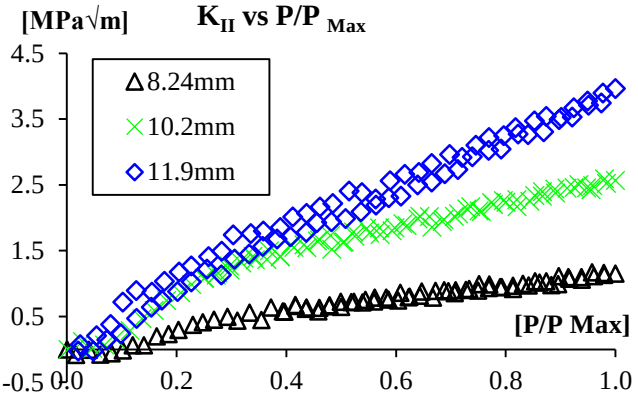

Figure 5-19. SIF mode II versus normalized applied load for modified C(T)

Figure 5-20 shows the evolution of crack angle and SIF (mode I and II). It is seen the influence of K_{II} as the crack kinks when K_{II} becomes present. It is also seen that K_{II} slope is less steep after the opening load has been surpassed. This behavior is due to the fact that the crack faces partially or completely slip in mode II after or before crack opening in mode I. When the crack opens, crack closure is overcomed, leaving the crack edges free to slide, hence they are not afected by their rugosity [51] making K_{II} less steep. At the same time however, such rugosity may amplify K_I as the crack flanks slide parallel to the inclined planes. Furthermore, Kibey et. al. [90] suggested that corrosion and grain size might hinder K_{II} development.

Figure 5-20 shows a comparison of, both experimental SIF schemes and FEM, maximum SIF with the observed kinking angle (θ*). It is observed a relation between the crack kinking angle and K_{II} presence. However, the effect of mode-

mixity (K_{II}/K_I ratio) is more visible in Figure 5-21. One case see that when the ratio K_{II}/K_I grows, the crack path starts curving.

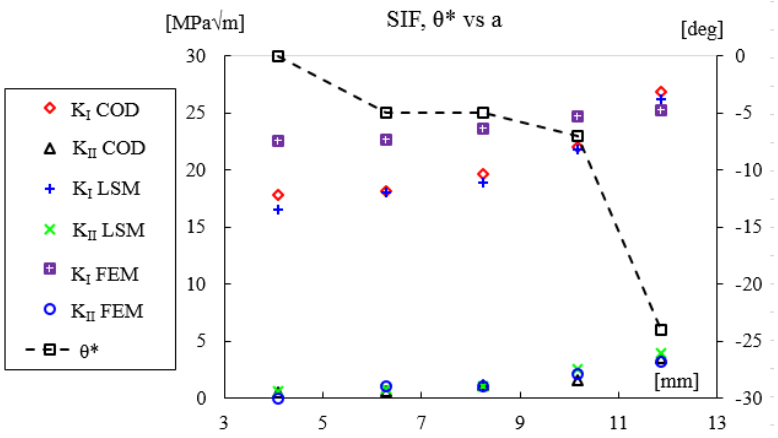

Figure 5-20. SIF and θ* vs. crack kinking angle for modified C(T) specimen

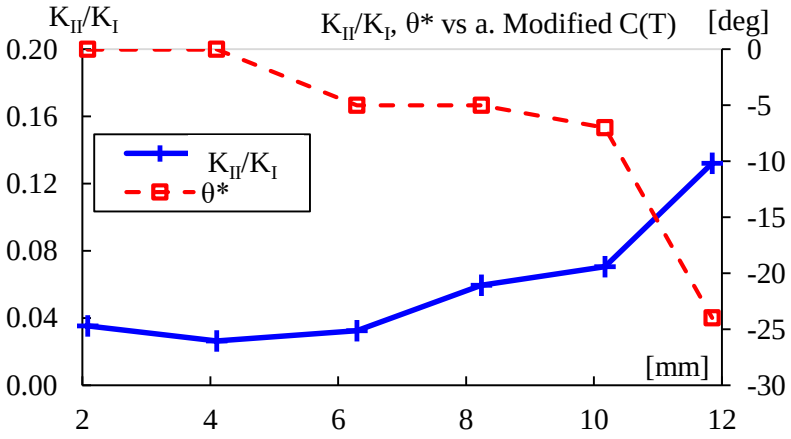

Figure 5-21. Mode mixity (K_{II}/K_I) versus crack kinking angle for modified C(T) specimen

Figure 5-22 depicts the variation of mixed-mode ratios during a cycle and from cycle to cycle for the six crack lengths presented in Figure 5-7. It can be seen how the ratio within a cycle remains quasi constant but grows from one crack length to the next one. Additionally, it is and more visible for the longer cracks where K_{II} is more perceptible, it is depicted the role of crack closure. If the crack faces are in contact, rugosity affects the ratio at lower loads, as for the same crack length, the ratio K_{II}/K_I exhibits a slightly different slope before the crack opens. Finally, it is observed how for the 4.1 and 6.3 mm crack lengths (points *a* and *b* from Figure 5-7) there is a drop in K_{II} after the crack seems to open. This may be attributed to the

crack being small enough so that rugosity, and crack flanks locking (induced by the crack's curvature) interfere with in-plane sliding.

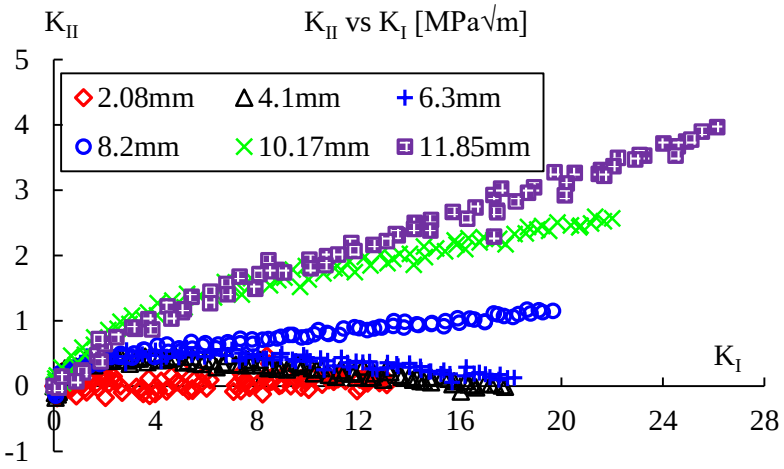

Figure 5-22. Variation of mixed-mode ratio, K_{II}/K_I for modified C(T) specimen

Finally, a summary of SIF results, experimental and numerical, is presented in Table 10 for the six measured points. Notice how as the crack length increases, the crack tip curves and gets closer to the stress concentration factor produced by the hole, K_I and K_{II} augment as well.

Table 10. C(T)´s maximum SIF for crack lengths depicted in Figure 5-7

Point	**a [mm]**	**θ***	**K_I COD**	**K_{II} COD**	**K_I LSM**	**K_{II} LSM**	**K_I FEM**	**K_{II} FEM**
0	2.1	0	13.12	0.46	13.41	0.61	21.2	0
a	4.1	0	17.78	0.47	16.48	0.65	22.5	0
b	6.29	-5	18.14	0.59	18.05	0.83	22.7	1.0
c	8.24	-5	19.67	1.17	18.83	1.09	23.6	1.0
d	10.17	-7	22.0	1.55	21.82	2.59	24.7	2.1
e	11.85	-24	26.85	3.55	26.14	3.96	25.2	3.2

5.3
Thin tubes

This section presents results and analysis for the five loading cases, described in Table 8, performed on the thin tubes. The exhibited results are: angle of principal stress calculated from the applied nominal stresses, SIF and SIF range calculated via the COD method, Eq. (7), with data from the experimentally obtained fields. An analysis on how to evaluate the equivalent SIF ranges, from the ES and Schöllmann et. al. models, with corresponding angle at which they happen is presented. The samples presented two or four cracks. However, the DIC data presented here is for the left crack only.

5.3.1
Specimen under tensile alternated loading (R-028)

The sample presented two initial cracks which grew perpendicular to the applied nominal stress. They were noticed starting at about 9,200 cycles from the outer most, left and right, notch boundaries. Figure 5-23 shows the angle of principal stress (calculated with nominal stress), $\theta_i=-2\tau_{xy}/(\sigma_{xx}- \sigma_{yy})$, not changing with the variation of applied principal nominal normal stress ($\sigma_{yy}=P/A$). In this case, the initiatial crack propagation angle coincided with the angle of principal stress. It has to be noted that no change in the angle of principal stress is seen when adding the stress concentration factor produced by the notch.

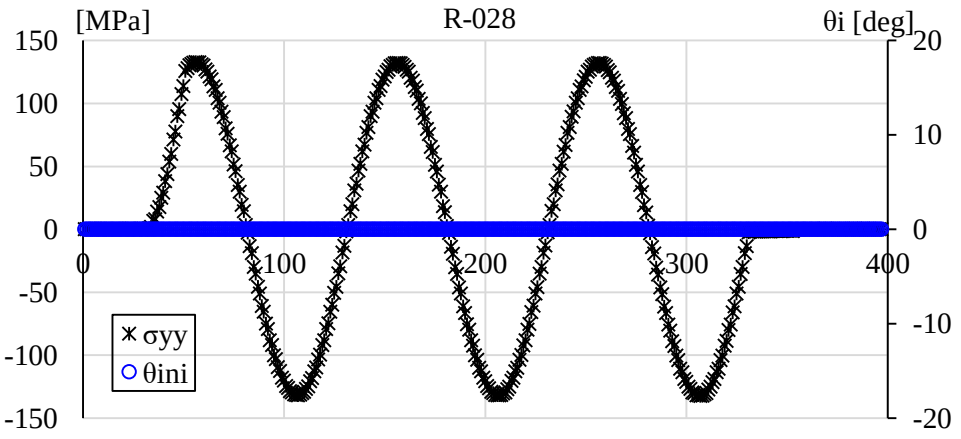

Figure 5-23. Variation of principal stress and corresponding angle for sample R-028.

Figure 5-24a shows the left-hand-side speckled photograph with the artificially highlighted 8.27 mm left crack at maximum applied load. Figure 5-24 (b), (c), and (d) show u, v and w DIC displacement fields, respectively. Figure 5-24e shows how three loading cycles are applied. It can be seen that the torsion load was zero. About 100 pairs of images were determined at a rate of 10 pairs of images/s for each of the three cycles. Load frequency for these image acquisition cycles was 0.1 Hz.

Figure 5-25a shows loading and SIFs values determined from the methods described in section 2: LSM method Eq. (16), relative crack flank opening displacements COD Eq. (7), and ⌡ Eq. (10). It can be seen that SIFs K_I and K_{II}, the later practically zero, are proportional to the axial and torsional load, respectively. Results for the three methods agree for most of the loading range except for negative load where the crack flanks touch and are stressed in compression (by the external axial load), therefore ⌡ would not make sense under a close crack hence is only presented when the crack is belived to be open. Figure 5-25b depicts the analyzed Y total strain data as given by the software VIC-3D®. Figure 5-25b also shows the total (elastic plus plastic) strain data at maximum axial load. It is observed a red contour delimiting total strains equal to 0.2%. Figure 5-25c, Figure 5-25d, and Figure 5-25e present data collection points for COD, LSM using seven Williams´ terms, and LSM using one Williams´ term, respectively. Furthermore, Figure 5-25d, shows the path used to evaluate ⌡, superimposed on the image as a continuous red

line, and how the AOI used for the LSM method using 7 terms was cropped to avoid the very large fictitious strains in the region near the crack flanks.

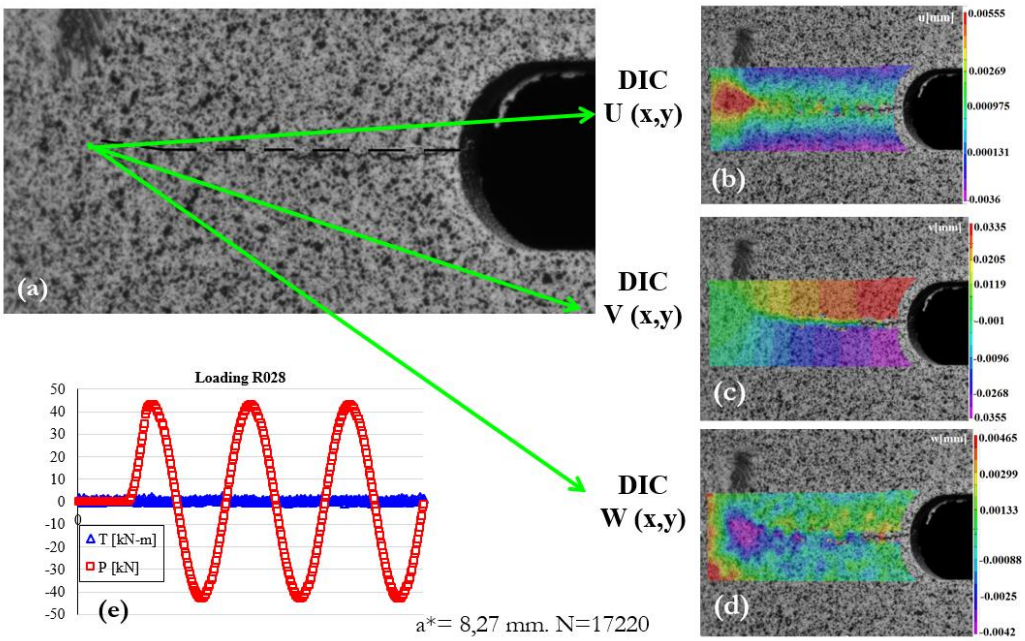

Figure 5-24. Representative R-028 specimen's results for an 8.27mm crack length (17720 cycles) (a) crack length (b) u displacement DIC field, (c) v displacement DIC field, (d) w displacement DIC field, (e) applied load.

COD variations with applied external load are presented in Figure 5-26a, whereas a comparison between K_I results determined from the LSM, COD and ⌡ methods is depicted in Figure 5-26b and calculated SIFs (both methods, COD and LSM). The load and crack geometry caused that the parallel-to-crack and out-of-plane direction relative COD to be zero as seen in Figure 5-26a. COD orthogonal-to-the crack direction is also presented in Figure 5-26a. The non-linear behavior (characteristic of plasticity, hysteresis, and crack closure opening) is observed in the plot where the applied load varies from low negative values to high positive values. Relative crack flank displacements for increasing and decreasing loads are respectively represented by the bottom and top branches of the COD-load loop, shown in Figure 5-26a. A closed crack is seen for the major part of the negative load represented by the COD-load curve being almost completely horizontal in that part of the plot; see section 6.1 for a deailed explanation. Figure 5-26c presents the

perpendicular-to-crack total strain variation versus load for a point distant about 1 mm ahead of the CTL.

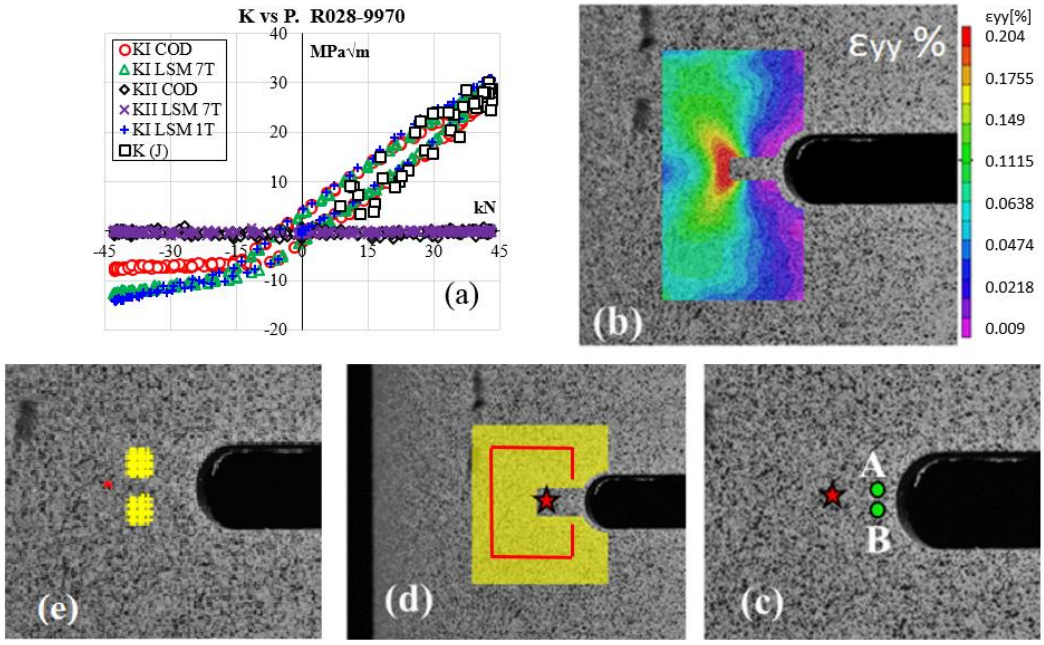

Figure 5-25. R-028 specimen's results for a 2.85 mm crack length at 9,970 cycles; (a) SIFs obtained with COD, ⌡,and LSM; (b) total orthogonal to the crack path DIC strain distribution; (c) CTL and pair of points A and B locations used to determine COD and related SIF; (d) CTL, area of inspection used to determine SIF using the LSM method with seven terms in Williams´s series, and path used to determine ⌡; (e) CTL and area of inspection used to determine SIF using the LSM method with one term in Williams´s series.

From the simmetry, load and crack geometry, it can be inferred that this behavior is representative for the area ahead of the crack tip. This strain-load loop displays a very close appearance to the COD-load, ⌡ and LSM-load loops for the positive loads, but for the negative part of the load. A more evident slope on the lower negative part of the loop, just where the crack is closed, is seen for the LSM-loops. In this case, a portion of the positive plastic strains that occurred when the crack was opened are reversed. Therefore, for points near the crack tip, the observed-by-DIC strains (caused by the negative load) is a superposition of plasticity reversion and elastic compression. This behavior is the cause of the differences between the SIF values when calculated by the LSM, and COD methods

for the crack-closed part of all curves. Therefore, the calculated SIF values are very similar for the three methods for the open crack, but disagree for the closed part of the crack. Besides, with the crack closed, the singularity expected by the Westergaard stress function simply does not exist.

The outcome obtained with the ⌡ deserve a note of its own. Although, and as stated above, the results for positive load values are the same for the SIF calculated with the LSM, COD and ⌡ methods, there is a substantial difference for the negative loads. Such result comes from the fact that when the load is negative, the crack lips are in touch so technically there is no crack. Thus, for negative loads, the sample´s configuration simply does not comply with Rice´s formulation. Such analysis is also extended for the lower portion of the positive loads. At that stage, the crack is still closed or partially closed, most likely due to crack closure, so again, Rice´s formulation will not work. Therefore, those values are omitted from the ⌡ plot here.

Figure 5-27 shows the three SIF mode variations and how their respective ranges were calculated from the COD method after 17,220 load cycles for a 7.8 mm crack. It can be seen that, although there is a dominant mode I SIF, there is also a slim mode III sliding that appears actuating, which did not appear at previous measurements. It also can be seen that mode III shows behavior similar to mode I opening, especially for the negative part of the load. This is attributed to the fact that for the crack is more difficult to slide when the crack flanks are touching, as discussed previously for the holed C(T) specimen in section 5.2, making out-of-plane displacement zero or near zero.

Figure 5-28a shows the evolution of SIF equivalent ranges versus crack size. It is clear that the mode I and equivalent range values are identical due to mode II and III ranges being absent or very small. Figure 5-28b shows the variation rate of the maximum mode II and mode III ranges over maximum mode I range with crack size along with experimentally determined crack-path tangent angle θ^*_o. Figure 5-28c shows experimentally measured (θ^*_o) and calculated (Erdogan-Sih θ^*_o ES and Schöllmann et al. θ^*_o S3D) crack-path tangent angles for each crack length. Figure 5-28d shows how mixed-mode behave during one cycle and from cycle to cycle.

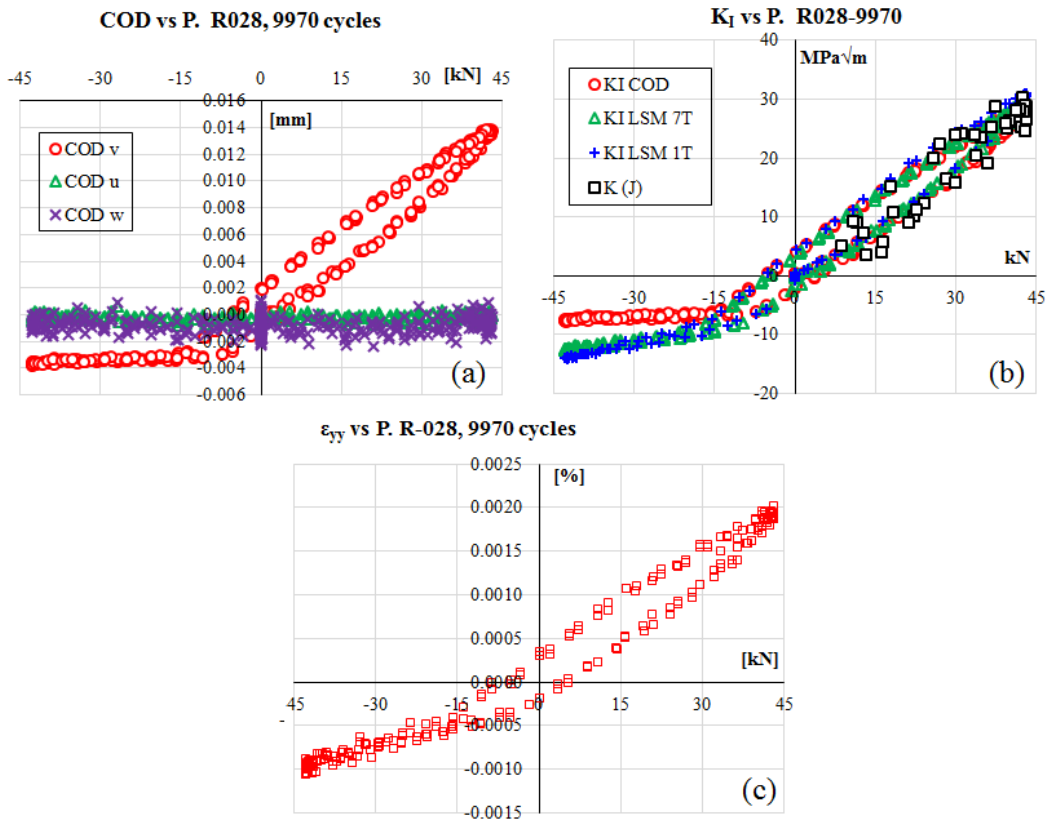

Figure 5-26**.** R-028 specimen's results for a 2.7mm crack length at 9,970 cycles; (a) COD for mode I, mode II, and mode III; b) SIF mode I calculated with LSM, COD and ⌡methods; c) normal-to-axis strains for a point 1 mm ahead of CTL.

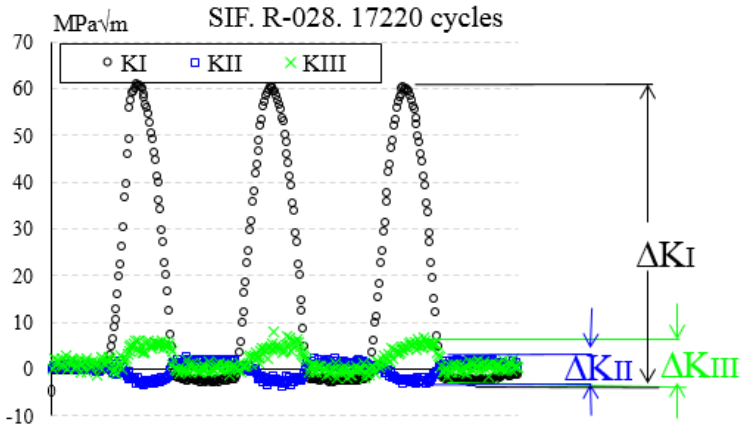

Figure 5-27. All mode SIF variations and ranges as calculated from the COD method after 17220 load cycles for a 7.8 mm crack length.

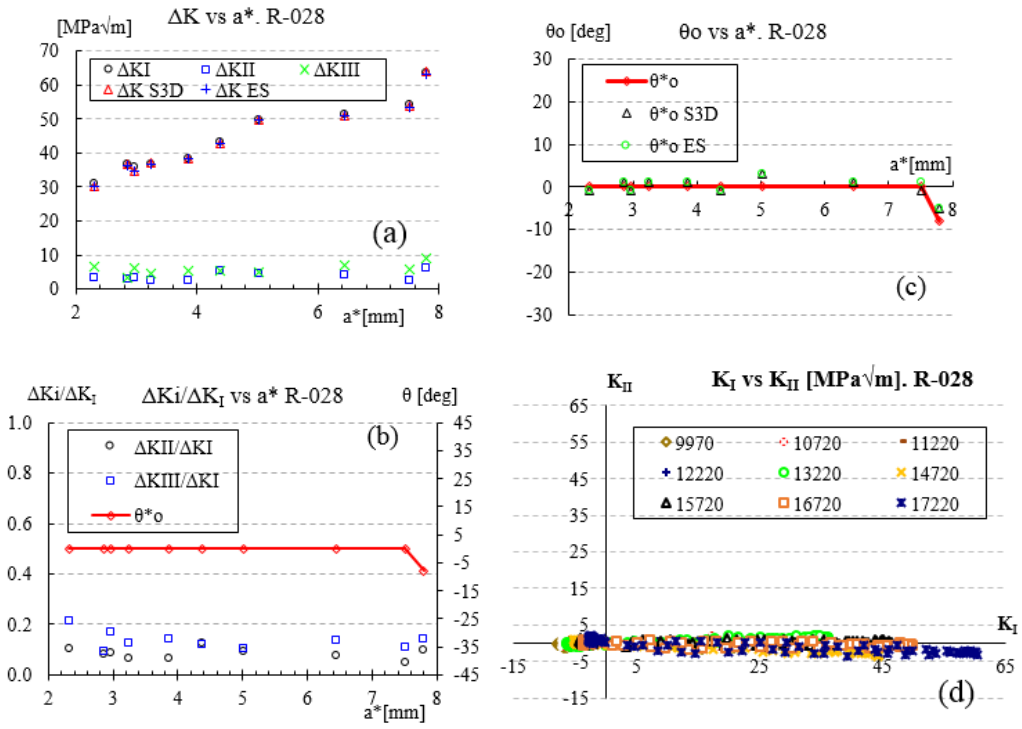

Figure 5-28. Crack tip parameters measured and calculated for specimen R-028; (a) evolution of mode I, II and III and equivalent SIF ranges versus crack length (b) variation of the maximum II and III over maximum mode I ranges and θ*o versus crack size, (c) θ*o, θ*o ES and θ*o S3D versus crack length (d) mode-mixity ratio during one cycle and from cycle to cycle.

Table 11 shows experimental results for specimen R-028: number of cycles (N), crack length (a*) in mm, SIF ranges in MPa√m that occur when maximum ΔK_I occur as shown in Figure 5-27, experimental angle θ*o, Erdogan-Sih (θo ES) Schöllmann et al (θo S3D), Erdogan-Sih and Schöllmann SIF ranges in MPa√m. The last two are the SIF ranges produced by the evaluation of Eq. (55) and Eq. (56), as described in section 4.5.

As a comparison, the same quantities are presented in Table 12, but this time using the maximum SIF range for each cycle regardless when they happen or in other words, SIF ranges that do not occur simultaneously. It shows results for specimen R-028: number of cycles (N), accumulated crack length (a*) in mm, maximum SIF ranges in MPa√m, Erdogan-Sih (θo ES), Schöllmann et al (θo S3D), Erdogan-Sih and Schöllmann et al SIF (ranges in MPa√m). It can be seen how, in this case, neither ES and S3D SIF ranges nor ES and S3D kink angles differ substantially from the presented values in Table 11.

Table 11. Experimental and calculated parameters for specimen R-028

N	a*	ΔK_I	ΔK_{II}	ΔK_{III}	θ*o	θo S3D	θo ES	ΔK S3D	ΔK ES
9420	2.32	30.87	3.27	6.6	0	-1	-1	30.4	30.4
9970	2.85	36.55	2.89	3.35	0	1	1	36.5	36.4
10720	2.97	35.84	3.12	6.04	0	-1	-1	34.8	34.8
11220	3.24	36.86	2.51	4.54	0	1	1	36.9	36.8
12220	3.85	38.3	2.44	5.38	0	1	1	38.3	38.2
13220	4.38	43.27	5.53	5.2	0	-1	-1	42.9	42.9
14720	5.02	49.84	4.58	5.06	0	3	3	49.9	49.9
15720	6.45	51.17	3.98	7.07	0	1	1	51	50.9
16720	7.51	54.06	2.65	5.85	0	-1	1	53.8	53.5
17220	7.8	63.73	6.36	9.0	-8	3	-5	63.9	63.3

Table 12. Experimental and calculated parameters for specimen R-028 using maximum SIF ranges for each cycle

N	a*	ΔK_I	ΔK_{II}	ΔK_{III}	θo S3D	θo ES	ΔK S3D	ΔK ES
9420	2.32	30.87	3.27	6.60	-11	-11	32.70	31.38
9970	2.85	36.55	2.89	3.35	-7	-7	37.67	36.89
10720	2.97	35.84	3.12	6.04	-6	-6	37.21	36.24
11220	3.24	36.86	2.51	4.54	-7	-6	37.66	37.11
12220	3.85	38.30	2.44	5.38	-8	-5	39.26	38.53
13220	4.38	43.27	5.53	5.20	-14	-14	44.89	44.30
14720	5.02	49.84	4.58	5.06	-8	-6	50.58	50.46
15720	6.45	51.17	3.98	7.07	-8	-7	52.57	51.62
16720	7.51	54.06	2.65	5.85	-8	-6	55.00	54.25
17220	7.80	63.73	6.36	9.00	-11	-11	66.10	64.66

5.3.2
Specimen under alternated torsional load (R-029)

This section presents exemplary and typical results determined for specimen R-029. As expected, four symmetrical initial cracks started from both (left and right) notch boundaries at about 45º from the horizontal slit axis. Figure 5-29 shows the angle of principal stress, $\theta_i=-2\tau_{xy}/(\sigma_{xx}-\sigma_{yy})$, which is proportional with the sign of applied principal nominal stress (τ_{xy}). In this case, the initiatial crack propagation angle coincided with the angle of principal stress.

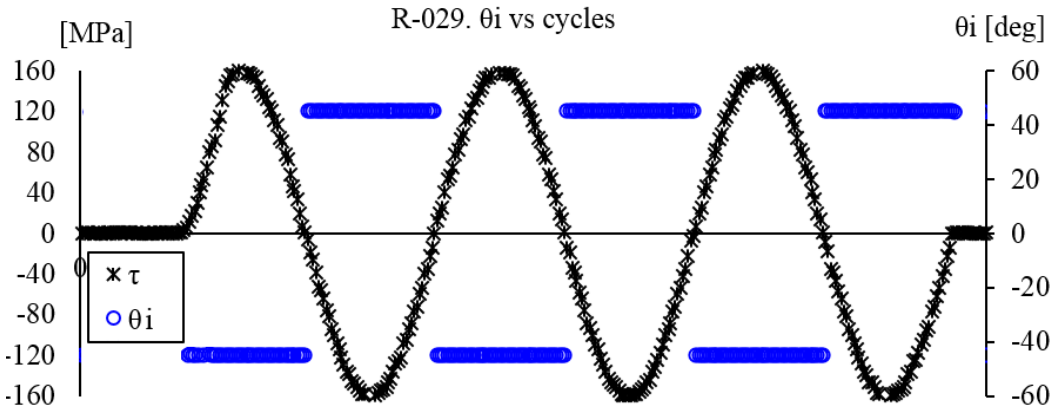

Figure 5-29. Variation of principal stress and angle with principal stress for sample R-029

Figure 5-30a shows the left top crack of 3.2 mm artificially highlighted for the sake of visualization. In Figure 5-30b and Figure 5-30c, it can be seen how displacement fields u and v are positioned parallel and perpendicular-to-the-crack, respectively, whereas the out-of-plane displacement field w is seen in Figure 5-30d. Additionally, Figure 5-30e shows the applied torsional load during 3 cycles. It can be seen that the axial force is zero.

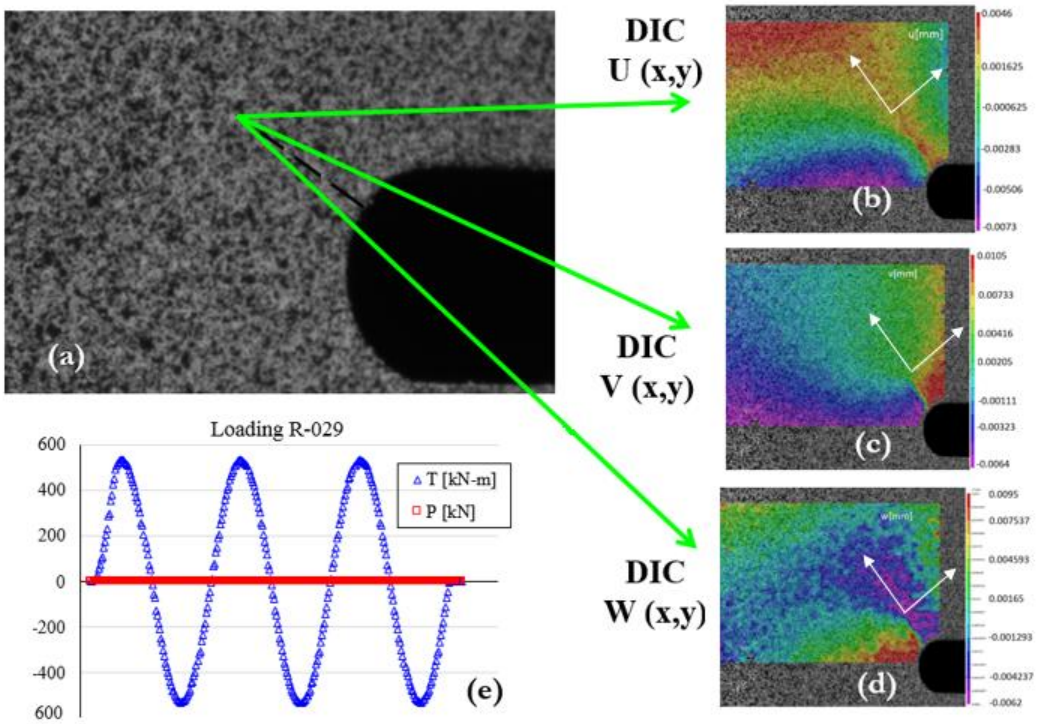

Figure 5-30. Representative R-029 specimen's results for crack length of 3.2mm at 18000 cycles (a) crack length (b) parallel-to-the-crack path DIC displacement distribution; (c) perpendicular-to-the-crack path DIC displacement distribution; (d) DIC out-of-plane displacement distribution; (e) applied loads.

Figure 5-31a presents three loading cycles for a 3.2 mm crack length at 18000 cycles. About 100 pairs of images were determined at a rate of 10 pairs of images/s for each of the three cycles. Load frequency for these image acquisition cycles was 0.1 Hz. It can be seen that the torsional load induces K_I and K_{II} and K_{III} different from zero, with all of them varying in phase with the torsional load. Figure 5-31a also shows SIFs values determined from LSM method (modes I and II) and COD method (modes I, II, and III). Results for both methods agree for the entire load range. Figure 5-31b depicts the analysed *Y* (parallel to the specimen axis) total strain data as given by the software VIC-3D®. Figure 5-31b also shows the total (elastic and plastic) strain data at maximum torque, 532N-m. It can be seen a red contour delimiting total strains equal to 0.07%, which is the maximum at that applied torque. In this case, symmetry occurs when four cracks (two on right and two on the left to the slit) propagate. Tensile and compressive strains alternate for each crack zone depending on the signal of the torsional load. Figure 5-31c shows the data points A

and B (located about 1.8 mm from the CTL) used to calculate SIFs applying the COD method. Figure 5-31d exhibits the AOI from which full-field displacement data were collected to determine the SIFs using the LSM method. This type of AOI was selected to avoid the very large fictitious strains in regions near the crack flanks.

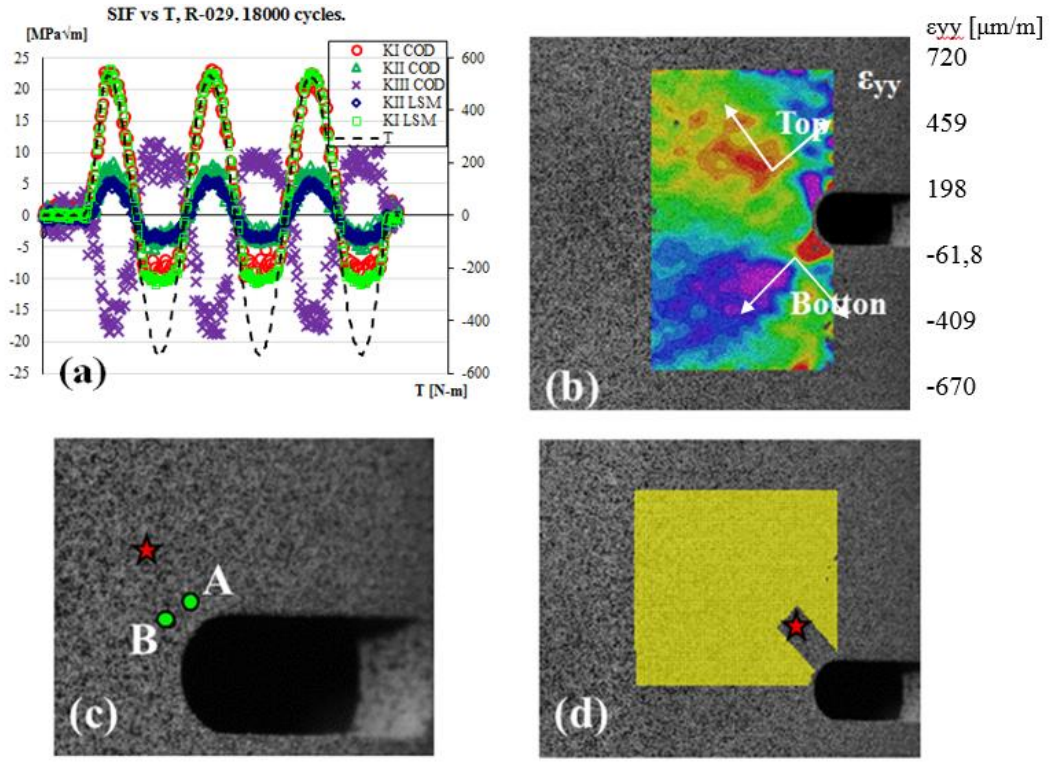

Figure 5-31. Representative R-029 specimen's results for a 3.2 mm crack at 18000 cycles; (a) applied loads and determined SIFs using both methods; (b) orthogonal to the specimen´s axis DIC total strain distribution; (c) CTL and pair of points A and B locations used to determine COD and related SIF; (d) CTL and cropped AOI used to determine SIF using the LSM method.

A comparison between SIF results (mode I and II) determined from the LSM and COD methods versus applied torque is presented in Figure 5-32a for the crack depicted in Figure 5-30a. Differently from specimen R-028, there are not observed relevant differences among SIFs calculated using both methods for the negative part of the loading. Furthermore, in Figure 5-32b is seen the perpendicular-to-crack strain taken about 1 mm ahead of the CTL. Opposite to what happened in specimen

R-028, the strain slant for negative torque values is almost flat. This behavior could explain the similar values and shapes for SIF measured by COD and LSM methods.

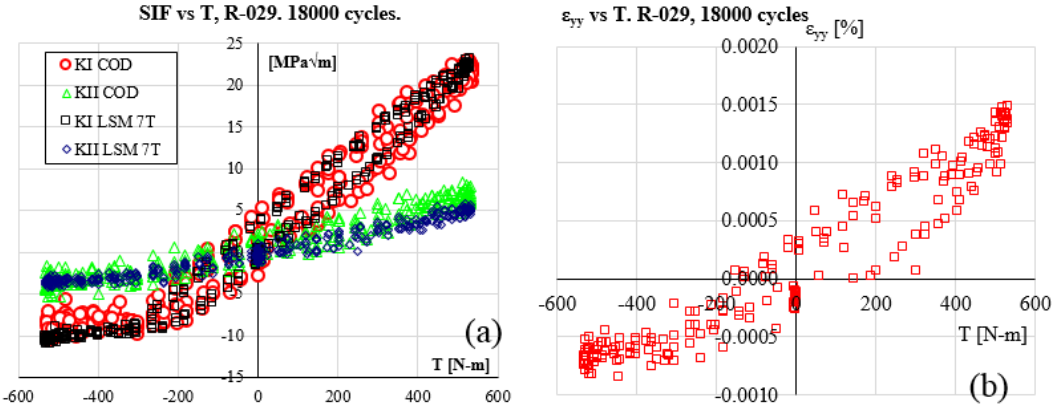

Figure 5-32. Specimen R-029 at a 3.2 mm crack length at 18000 cycles; a) SIF variation (calculated with COD and LSM) with the applied torsional load, b) perpendicular to crack strain.

An example of crack flank relative displacements (orthogonal-to-the crack, parallel to-the crack, and out-of-plane) for the top left versus applied torque are shown in Figure 5-33a, whereas in Figure 5-33b the same relative displacements are shown for the bottom left crack. One can easily observe the symmetry the relative displacements exhibit for the alternating torsional load signal.

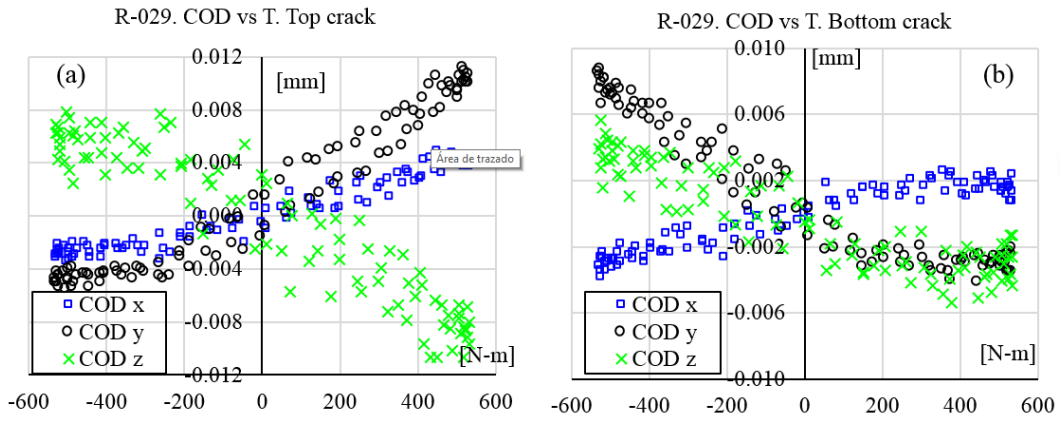

Figure 5-33. Exemplary relative crack flank displacements for specimen R-029 at 18000 cycles (a) top crack, (b) bottom crack.

Figure 5-34 shows SIF variation for modes and respective ranges calculated from the COD method after 18000 load cycles for a 3.2 mm crack. It can be seen

that, although there is a prominent mode I SIF and a medium mode II SIF, a mode III sliding is also present with high SIF values. It also can be seen that modes I and II actuate in phase.

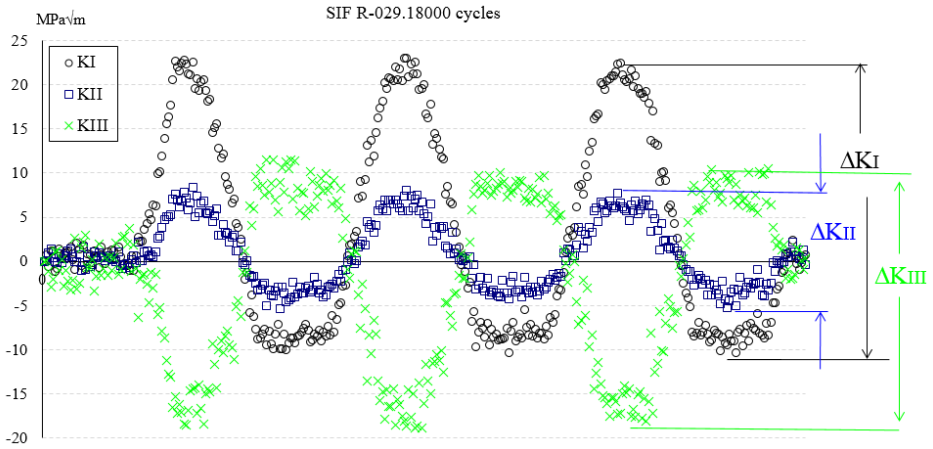

Figure 5-34. SIF variations and ranges for the three modes as calculated from the COD method after 18,000 load cycles for a 3.2 mm crack size

Figure 5-35a shows the evolution of SIF equivalent ranges versus crack size. It can be seen that mode III sets apart equivalent range values, as the Schöllmann et al, Eq. (56), is the only evaluated criterion that considers mode III. Figure 5-35b shows the variation rate of the maximum II and III mode ranges over maximum mode I range with crack size along with experimentally determined crack-path tangent angle θ^*_o. Figure 5-35c shows experimentally measured (θ^*_o) and calculated (Erdogan-Sih θ^*_o ES and Schöllmann et al. θ^*_o S3D) crack-kinking angles for each crack length with respect to the sample´s horizontal axis. Figure 5-35d shows how mixed-mode ratios change during one cycle and from cycle to cycle for specimen R-029.

Table 13 shows experimental results for specimen R-029: number of cycles (N), crack length (a*) in mm, SIF ranges in MPa√m that occur at maximum ΔK_I as shown in Figure 5-34, θo, Erdogan-Sih (θo ES) calculated angle, Schöllmann et al (θo S3D) calculated angle, Erdogan-Sih and Schöllmann et al SIF ranges in MPa√m. The last two are the SIF ranges produced by the evaluation of Eq. (55) and Eq. (56), as described in section 4.5.

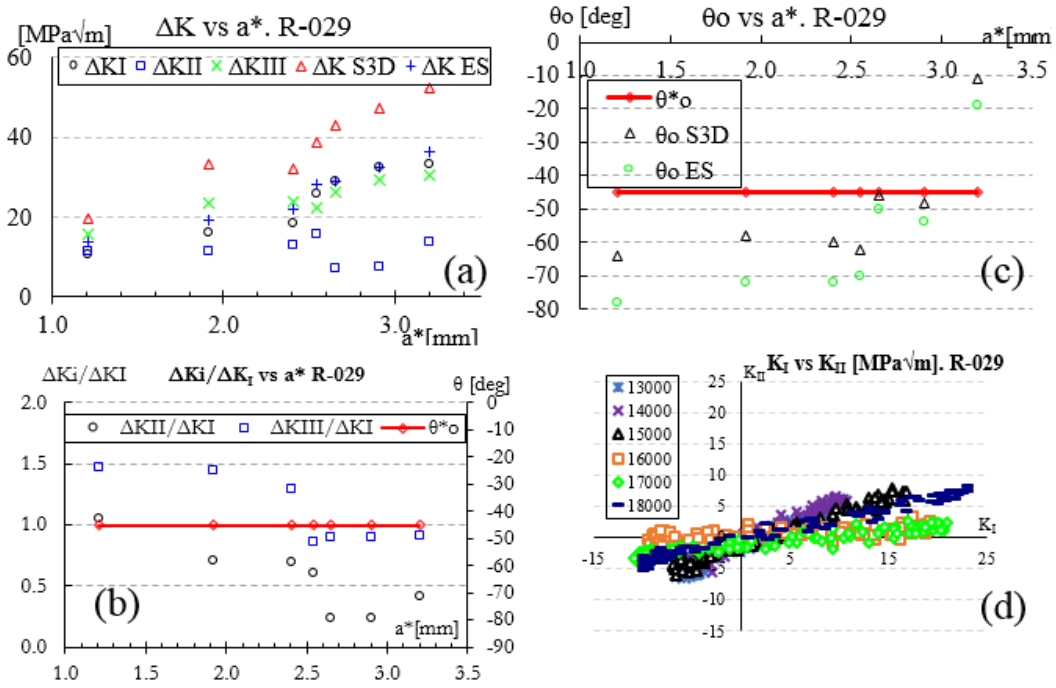

Figure 5-35. Crack tip parameters measured and calculated for specimen R-029, 532N-m max. torque (a) Evolution of mode I, II and III and equivalent SIF ranges versus crack length (b) variation of the maximum II and III over maximum mode I ranges and θ*o versus crack size, (c) θ*o, θo ES (Erdogan-Sih) and θo S3D (Schöllmann et al.) versus crack length (d) mode-mixity ratio during one cycle and from cycle to cycle.

As a comparison in Table 14 are presented the same quantities but this time using the maximum SIF range for each cycle, regardless where they occur. It shows results for specimen R-029: number of cycles (N), crack length (a*) in mm, maximum SIF ranges in MPa√m, Erdogan-Sih (θo ES) calculated angle, Schöllmann et al (θo S3D) calculated angle, Erdogan-Sih and Schöllmann et al SIF (ranges in MPa√m). It can be seen how both ES and S3D SIF ranges and kink angles differ from the presented values in Table 13. This could be explained by the fact that although the values presented in Table 13 are calculated with the concurrent SIF, and the values of Table 14 are done so with the maximum SIF values regardless of when they occur, the noise in the SIF results makes the values vary, i.e., see the plot of K_{III} in Figure 5-34, where is also seen that at the time of maximum K_I K_{II}, and K_{III} present a smaller value than their respective ranges. Therefore, the difference observed in ΔK ES and ΔK S3D between Table 13 and Table 14.

Table 13. Experimental and calculated parameters for specimen R-029

N	a*	ΔK_I	ΔK_{II}	ΔK_{III}	θ*o	θo S3D	θo ES	ΔK S3D	ΔK ES
12000	1.21	10.6	5.5	12.4	-45	-19	-33	19.6	13.9
13000	1.92	16.2	10.5	17.8	-45	-13	-27	33.4	19.4
14000	2.4	18.5	12.5	15.7	-45	-15	-27	32.2	21.9
15000	2.55	26.0	15.6	19.1	-45	-17	-25	38.6	28
16000	2.65	29.2	3.2	18.9	-45	-1	-5	43	28.9
17000	2.91	32.7	5.0	24.9	-45	-3	-9	47.3	32.5
18000	3.2	33.3	13.1	27.4	-45	-11	-19	52.2	36.4

Table 14. Experimental and calculated parameters for specimen R-029 using maximum SIF ranges for each cycle

N	a*	ΔK_I	ΔK_{II}	ΔK_{III}	θo S3D	θo ES	ΔK S3D	ΔK ES
12000	1.21	10.63	11.24	15.62	-17	-31	24.79	16.59
13000	1.92	16.23	11.50	23.53	-13	-25	35.27	21.45
14000	2.40	18.51	12.95	23.97	-13	-25	37.59	24.37
15000	2.55	26.03	15.85	22.32	-17	-23	43.31	32.74
16000	2.65	29.15	7.00	26.26	-1	-5	44.74	29.98
17000	2.91	32.66	7.71	29.44	-3	-9	50.42	34.14
18000	3.20	33.34	13.73	30.40	-9	-21	53.43	38.37

5.3.3
Specimen under in-phase alternated axial-torsional load (R-030)

Two symmetric cracks started at the slit notch boundaries, one at the left and another at the right notch boundary at about 20°. Figure 5-36 shows how the angle of principal stress, $\theta_i=-2\tau_{xy}/(\sigma_{xx}-\sigma_{yy})$, does not change with the variation of applied nominal stress (σ_{yy} and τ_{xy}). In this case, the initiatial crack propagation angle was very close to the angle of principal stress.

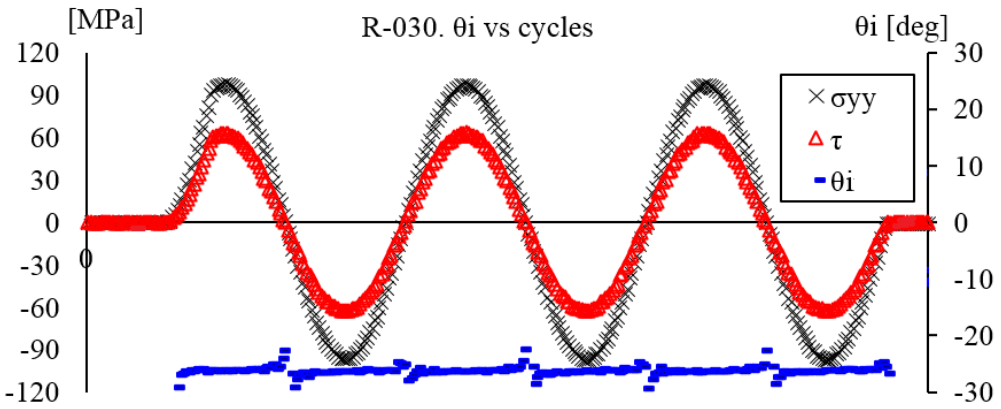

Figure 5-36. Angle of principal stress with applied stress for specimen R-030

Figure 5-37a shows the right-hand-side speckled photograph for a 9.21 mm crack at 14250 cycles artificially highlighted. Figure 5-37b, Figure 5-37c, and Figure 5-37d show parallel-to-the-crack, perpendicular-to-the-crack, and out-of-plane DIC displacement fields, respectively. The fields u and v are positioned parallel and perpendicular-to-the-crack. Figure 5-37e shows how three loading cycles are applied. The loads can be seen acting in phase. About 100 pairs of images were determined at a rate of 10 pairs of images/s for each of the three cycles. Load frequency for these image acquisition cycles was 0.1 Hz. Figure 5-38 and Figure 5-39 show results obtained for a 3.86 mm crack at 10000 cycles that emanated from the right boundary point located at an angle of approximately 18° relative to the horizontal slit-notch machined in the specimen. Figure 5-39 shows SIFs for modes

I and II determined from the LSM and COD methods and opening strains (*Y* direction, perpendicular to crack axis) during one cycle for a point near the CTL.

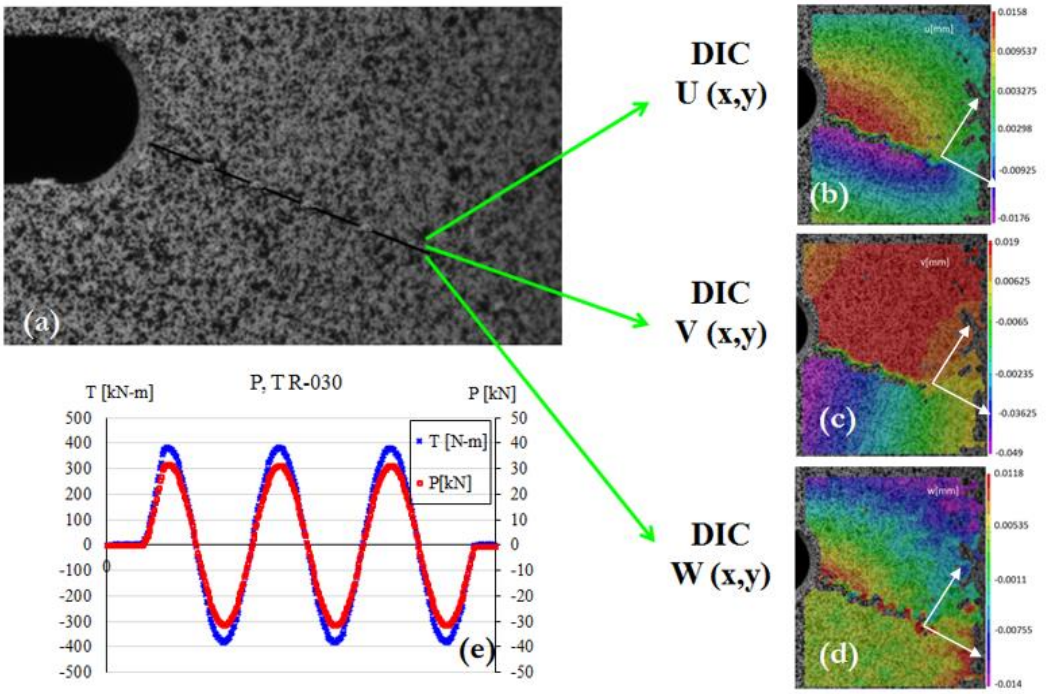

Figure 5-37. Representative R-030 specimen's results for a 9.21 mm crack at 14250 cycles (a) crack length (b) u DIC displacement field; (c) v DIC displacement field; (d) w displacement field; (e) applied loads.

Figure 5-38a presents three loading cycles relative to a 3.86 mm crack and 10000 cycles. It can be seen that the torsional load induces K_I and K_{II} different from zero, the later higher than the former, both varying in phase with the torsional load. Figure 5-38a also shows SIFs values determined from both methods, LSM and COD. Results for both methods agree for the positive part of the load range but there are observed relevant differences for the negative load range. Similar effects occurred for specimen R-028, and they are related with the parts of the load range that caused the phenomena of crack closing-opening, and crack flank roughness in phase with relative displacements and crack blunting.

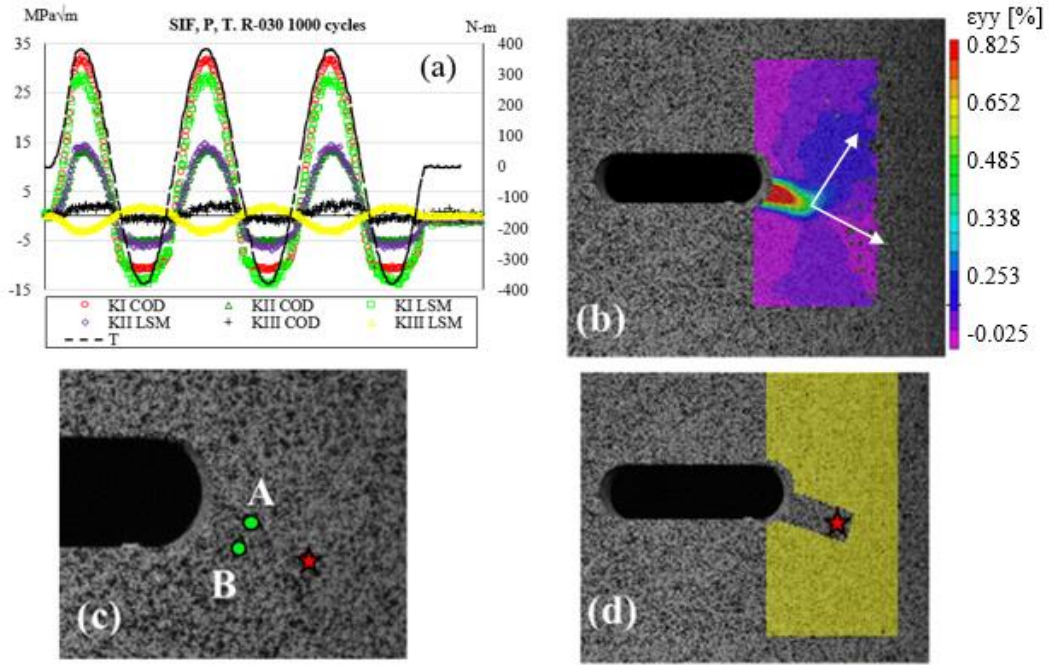

Figure 5-38. Representative R-030 specimen's results for a 3.86 mm crack at 10000 cycles; (a) applied loads and determined SIFs for mode I, II and III; (b) orthogonal-to-the-crack DIC total strain distribution, (c) CTL and pair of points A and B locations used to determine COD and related SIF; (d) CTL and cropped AOI used to determine SIF using the LSM method

Figure 5-38b shows an AOI without excluding the crack zone flanks. Executing an analysis with such AOI would cause the determination of very large fictitious strains along the crack length due to the very high relative displacements that occur inside a DIC subset near or at the crack lips. Figure 5-38b also shows the fictitious total (elastic plus plastic) strain data at maximum axial load. It can be seen a red contour delimiting total fictitious strains as high as 0.82%. Figure 5-38c depicts the data points A and B (located in this case about 3.0 mm from the CTL) used to calculate SIFs applying the COD method. Figure 5-38d presents the AOI from which full-field displacement data were collected from to determine the SIFs using the LSM method. This cropped AOI was selected to avoid very large fictitious strains in regions near the crack flanks.

Figure 5-39a presents a comparison of SIF using the COD and the LSM method for the modes. For mode I, the values are pretty much the same and the behavior is very close to what was seen on specimen R-028 for both, the positive

and negative parts of the load. The SIF mode I for the COD method shows none or little slant for the negative part of the load, whereas the same component for the LSM method a slant is clearly visible. Figure 5-39b shows perpendicular-to-crack strain-as given by the software VIC-3D. There is a slope difference at the negative part of the load for the SIF mode I determined values. Plasticity ahead of CTL causes difference between COD (when using exemplary points shown in Figure 5-38c) and LSM (when using AOI shown in Figure 5-38d). Mode II SIF show very close values and similar shapes. Although there is an apparent contradiction in the SIF for mode III sign, both methods present near zero values, as the same for other crack lengths. So that, such small difference can be disregarded as noise.

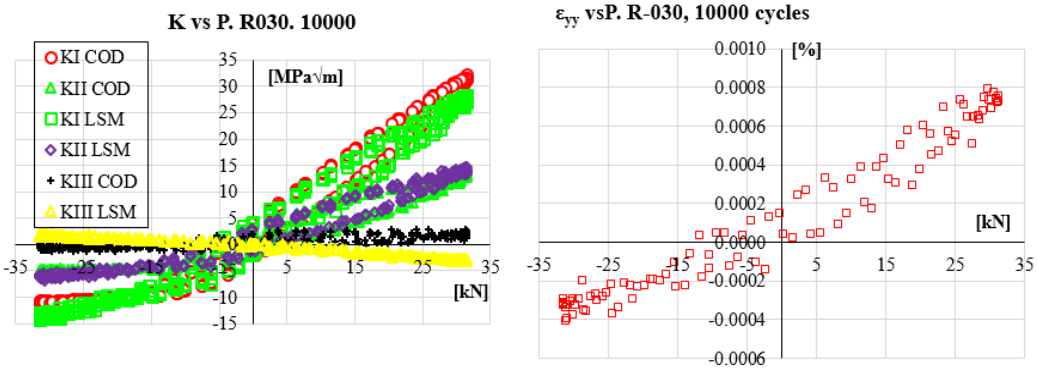

Figure 5-39. Specimen R-030 for a 3.86 mm crack at 10000 cycles, a) LSM and COD calculated SIF, b) perpendicular-to-crack strain

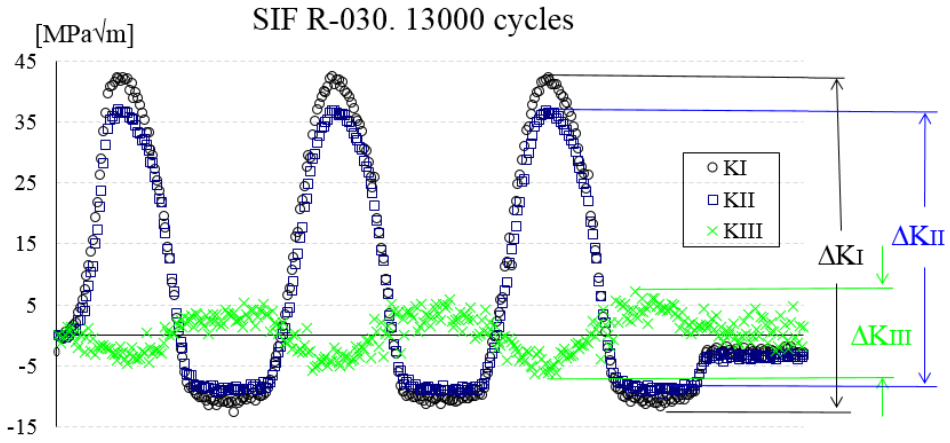

Figure 5-40. All mode SIF variations and ranges as calculated from the COD method after 13000 cycles for a 6.5 mm crack.

Figure 5-40 shows the three COD-determined SIF mode variations after 13000 load cycles for a 6.5 mm crack. It can be seen that SIFs for modes I and II SIF are about the same order of magnitude, whereas SIF mode III range is very small compared to them. It can also be noted that SIFs mode I and II occur in-phase, as expected by the applied type of loading.

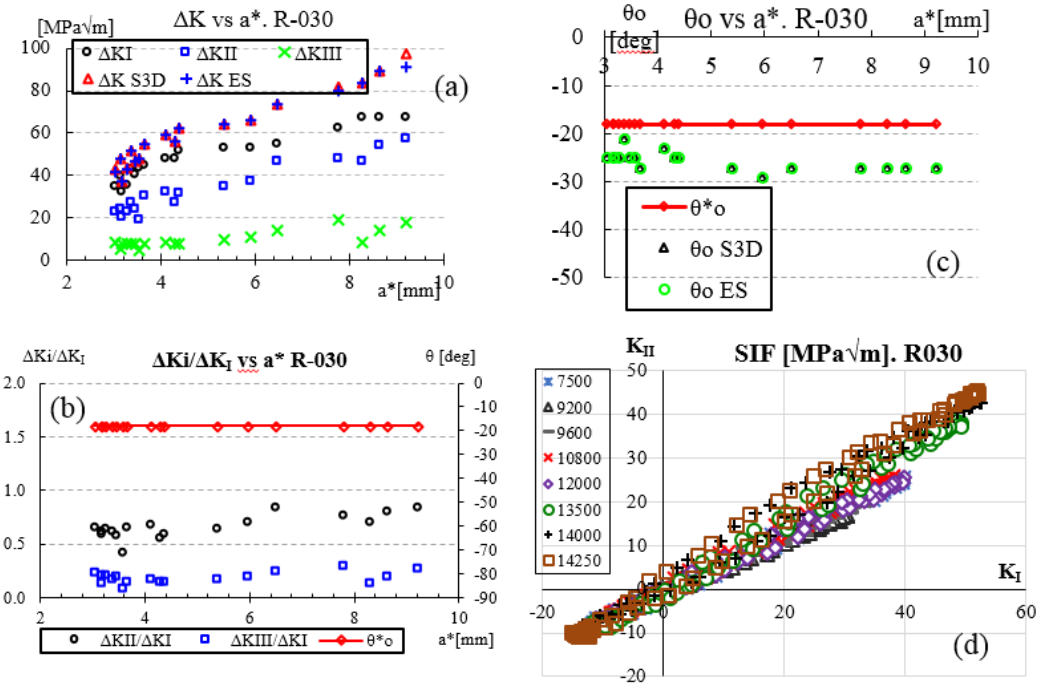

Figure 5-41. Crack tip parameters for specimen R-030 (a) Evolution of mode I, II and III and equivalent SIF ranges versus crack length (b) variation of maximum mode II and III over maximum mode I ranges and θ*o versus crack size, (c) θ*o, θo ES and θ*o S3D versus crack length (d) mode-mixity ratio during one cycle and from cycle to cycle.

Figure 5-41a shows the evolution of SIF equivalent ranges versus crack size. Figure 5-41b shows the variation rate of the maximum II and III mode ranges over maximum mode I range with crack size along with experimentally determined crack-path tangent angle θ^*_o. It is noted how the ratios do not change as the crack growths. Figure 5-41c shows experimentally measured (θ^*_o) and calculated (Erdogan-Sih θ_o ES and Schöllmann et al. θ_o S3D) crack-path tangent angles for

each crack length. Figure 5-41d shows how mixed-mode ratios change during one cycle and from cycle to cycle. It is observed how the variations occurring during the cycle and from cycle to cycle are small due to reasonably proportional mixed-mode I and II ratios.

Table 15 shows experimental results for specimen R-030: number of cycles (N), accumulated crack length (a*) in mm, SIF ranges in MPa√m that occur at maximum ΔK_I as depicted in Figure 5-40, experimental angle θ*o, Erdogan-Sih (θo ES) calculated angle, Schöllmann et. al. (θo S3D) calculated angle, Erdogan-Sih and Schöllmann et. al. SIF ranges in MPa√m. The last two are the SIF ranges produced by the evaluation of Eq. (55) and Eq. (56), as described in section 4.5.

As a comparison, the same quantities are presented in Table 16, but this time using the maximum SIF range for each cycle. It shows results for specimen R-030: number of cycles (N), accumulated crack length (a*) in mm, maximum SIF ranges in MPa√m, Erdogan-Sih (θo ES) calculated angle, Schöllmann et al (θo S3D) calculated angle, Erdogan-Sih and Schöllmann et. al. SIF (ranges in MPa√m). It can be seen how both ES and S3D SIF ranges and kink angles differ from the presented values in Table 15. This difference could be explained by the fact that whereas the values presented in Table 15 are calculated with the simultaneous SIF, the values presented in Table 16 are done so with the maximum values regardless of when they occur. In Figure 5-40 is seen that at the time of maximum K_I, K_{II}, and K_{III} present a smaller value than their respective ranges. Therefore, the difference observed in ΔK ES and ΔK S3D between Table 15 and Table 16.

Table 15. Experimental and calculated parameters for specimen R-030

N	a*	ΔK_I	ΔK_{II}	ΔK_{III}	θ^*o	θo S3D	θo ES	ΔK S3D	ΔK ES
7500	3.17	31.7	18.8	1.5	-18	-25	-25	37.6	37.55
8000	3.03	33.6	21.7	3.8	-18	-25	-25	41.9	41.37
8400	3.26	34.8	21.2	4.0	-18	-25	-25	43.2	42.51
8800	3.45	39.8	22.2	0.9	-18	-25	-25	46.7	46.74
9200	3.16	39.6	22.8	0.3	-18	-25	-25	47	46.98
9600	3.36	42.5	26.3	3.9	-18	-25	-25	51.9	51.35
10000	3.56	43.5	18.3	2.3	-18	-21	-21	47.8	47.67
10400	3.66	44.4	28.8	0.4	-18	-25	-25	54.9	54.8
10800	4.12	47.0	31.6	1.1	-18	-27	-27	58.7	58.59
11200	4.3	47.6	26.0	0.2	-18	-23	-23	55.9	55.86
11600	4.38	51.3	29.6	0.3	-18	-25	-25	61.6	61.64
12000	5.38	52.7	32.5	2.0	-18	-25	-25	63.9	63.88

12500	5.95	53.1	36.3	2.8	-18	-27	-27	65.7	65.67
13000	6.5	55.0	45.6	7.9	-18	-29	-29	73.8	73.17
13500	7.8	61.7	45.2	12.4	-18	-27	-27	81.1	79.26
13750	8.3	66.8	45.6	2.2	-18	-27	-27	83.8	83.67
14000	8.65	67.2	52.2	7.7	-18	-27	-29	89.1	88.3
14250	9.21	67.4	55.3	27.7	-18	-27	-29	96.6	90.36

Table 16. Experimental and calculated parameters for specimen R-030 using maximum SIF ranges for each cycle

N	a*	ΔK_I	ΔK_{II}	ΔK_{III}	θo S3D	θo ES	ΔK S3D	ΔK ES
7500	3.17	31.7	19.7	6.7	-44	-44	45.20	44.34
8000	3.03	33.6	22.4	8.0	-44	-45	49.57	48.47
8400	3.26	34.8	22.4	7.7	-42	-45	50.41	49.40
8800	3.45	39.8	23.3	7.6	-40	-40	55.14	54.23
9200	3.16	39.6	23.4	5.5	-41	-40	54.68	54.20

9600	3.36	42.5	26.5	7.7	-44	-44	60.34	59.50
10000	3.56	43.5	18.6	4.2	-37	-38	53.25	52.95
10400	3.66	44.4	29.4	6.9	-43	-42	64.46	63.84
10800	4.12	47.0	32.3	8.3	-45	-40	69.53	68.69
11200	4.30	47.6	26.8	7.3	-43	-41	64.56	63.85
11600	4.38	51.3	31.2	7.6	-44	-43	71.75	71.06
12000	5.38	52.7	33.7	9.0	-44	-44	75.52	74.62
12500	5.95	53.1	37.0	10.7	-47	-47	79.40	78.20
13000	6.50	55.0	46.4	13.5	-50	-50	90.92	89.28
13500	7.80	61.7	47.6	18.2	-46	-48	98.28	95.49
13750	8.30	66.8	46.3	8.2	-46	-47	98.73	98.15
14000	8.65	67.2	54.0	13.6	-48	-49	107.68	106.25
14250	9.21	67.4	56.5	28.2	-48	-50	114.73	109.00

5.3.4
Specimen under 90º phase axial-torsional alternated load (R-031)

This specimen presented two cracks that started at the slit notch boundaries, one at the left and another at the right notch boundary. Figure 5-42 shows how the angle of nominal applied principal stress, $\theta_i=-2\tau_{xy}/(\sigma_{xx}- \sigma_{yy})$, changes with the variation of applied nominal stress (σ_{yy} and τ_{xy}). As opposed with the previous specimens, the initial crack propagation angle did not coincide with the angle of the nominal principal stress.

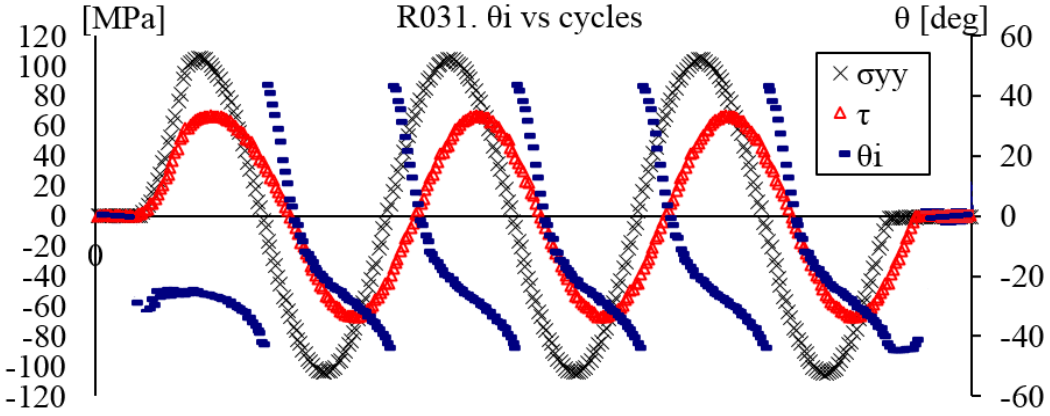

Figure 5-42. Angle of principal stress with applied stress for specimen R-031

Figure 5-43a presents the entire path of the left crack. Selected points were marked and denoted from A to I to highlight the path. Two abrupt kink angles are shown at points D and F. The crack initiates from the slit left boundary and propagates (along points A, B, C) making an angle equal to 45º with the horizontal axis. At approximately 9.28 mm length and after 30000 cycles, point D, the path kinks and the crack grows following an angle of 14º for 1500 cycles until point F. After this second kink, it continues growing following a path with angle -22º. The u, v and w displacement components at maximum axial load for point I, given by the VIC-3D® output (rigid motion already compensated), are depicted respectively in Figure 5-43b, Figure 5-43c and Figure 5-43d respectively. Relative (opposite) motion of the crack flanks can be clearly seen. Mode III opening is evidently

depicted in Figure 5-43d, whereas Figure 5-43e shows how three loading cycles were applied. It can be observed that axial force and torsion load are out of phase. About 100 pairs of images were determined at a rate of 10 pairs of images/s for each of the three recorded cycles. Load frequency for these image acquisition cycles was 0.1 Hz.

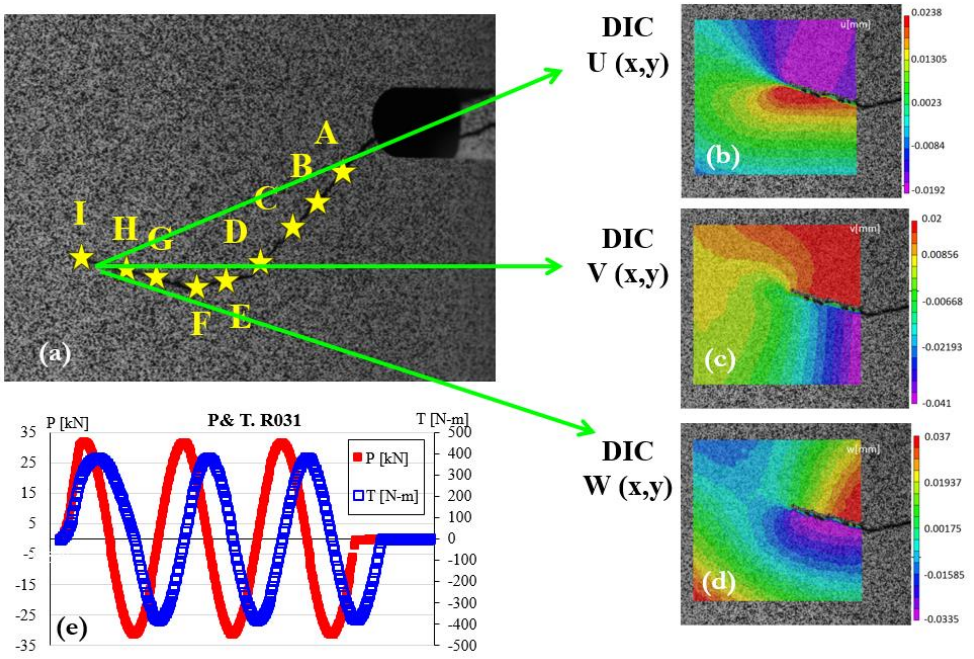

Figure 5-43. Representative R-031 specimen's results: (a) the entire crack path with respective number of cycles for points A to I shown in Table 17. (b) parallel-to-the-crack path DIC displacement field for F to I crack path; (c) perpendicular-to-the-crack path DIC displacement field for F to I crack path; (d) DIC out-of-plane displacement field for F to I crack path; (e) applied out-of-phase loads.

For this specimen, SIF values in all three modes, using the LSM method, were calculated using the displacements in each direction as shown in Eq. (5). Due to the specimen radius, there is an error when approximating a distance between two points in a curved surface by the simple subtraction of coordinates between them, just like it has to be done when calculating the distance from CTL. The AOI for the LSM with 1 term was chosen by selecting two 1 x 1 mm squares located at oposite sides of the crack edges and about 1 mm behind the CTL, as seen in Figure 5-44d.

Figure 5-44a, Figure 5-44c, and Figure 5-44e show the comparison for K_I, K_{II}, and K_{III} respectively obtained with COD, LSM method with one term, and LSM method with seven terms with their respective AOI.

By keeping the AOI close to the CTL, the error when calculating the $1/\sqrt{r}$ distance is lowered. Additionally, the compressive applied axial load would create negative strains ahead of the crack tip, possibly generating fictitious K_I values (see section 6.1 for details about the interpretation of negative K_I), so the AOI to gather displacement data should be kept behind the CTL. It can be seen that K_I obtained with 7 terms (using AOI data shown in Figure 5-44f) shows larger values than the ones obtained the LSM method. For those reasons, the COD values are more representative of the stress field than the LSM 7 terms. Figure 5-44 depicts the non-linear behavior usually seen when there is accumulated plasticity and crack closure represented by the negative K_I non-linear variation for both negative axial and torsional loads as seen in Figure 5-44a. It can also be seen the almost straight lines of almost constant K_{II} and K_{III} values, in Figure 5-44c and Figure 5-44f respectively for both COD and LSM method. They can be interpreted as the crack permanently slides (or stays open) in those modes regardless of change in the loading condition. Moreover, the three SIF modes do not express a proportional behavior to neither axial nor torsional loads, showing dependence on both of them.

In Figure 5-44a and according to the COD method, it is observed when crack opens in mode I at about -7kN, stays open all the way to the maximum axial load, to finally close at about -17kN during the unloading stage. Therefore, SIF mode I must depend on both axial and torsional loads for the crack to stay open at such high compressive load. During that axial load range, if K_I shows positive values, the sample crack faces are not touching each other allowing K_{II} and K_{III} to slide freelier. That assumption would explain the relatively high values for K_{II} and K_{III}, in addition to the cyclic strain hardening increase produced by the non-proportional loading. It can be also seen how the change of sign for K_{II} and K_{III} represents the crack shifting sliding directions, which occurs even when the crack is closed probably making the crack surfaces get smoothed under compressive forces.

The variation of all SIF modes during only cycle for selected crack lengths versus applied axial load are depicted in Figure 5-45a for point C for 28000 cycles, Figure 5-45b for point E for 31500 cycles, and Figure 5-45c for point H for 32600

cycles. All SIF values were calculated using the COD method. Finally, in Figure 5-45d is shown perpendicular-to-crack strains for points ahead about 1 mm of CTL.

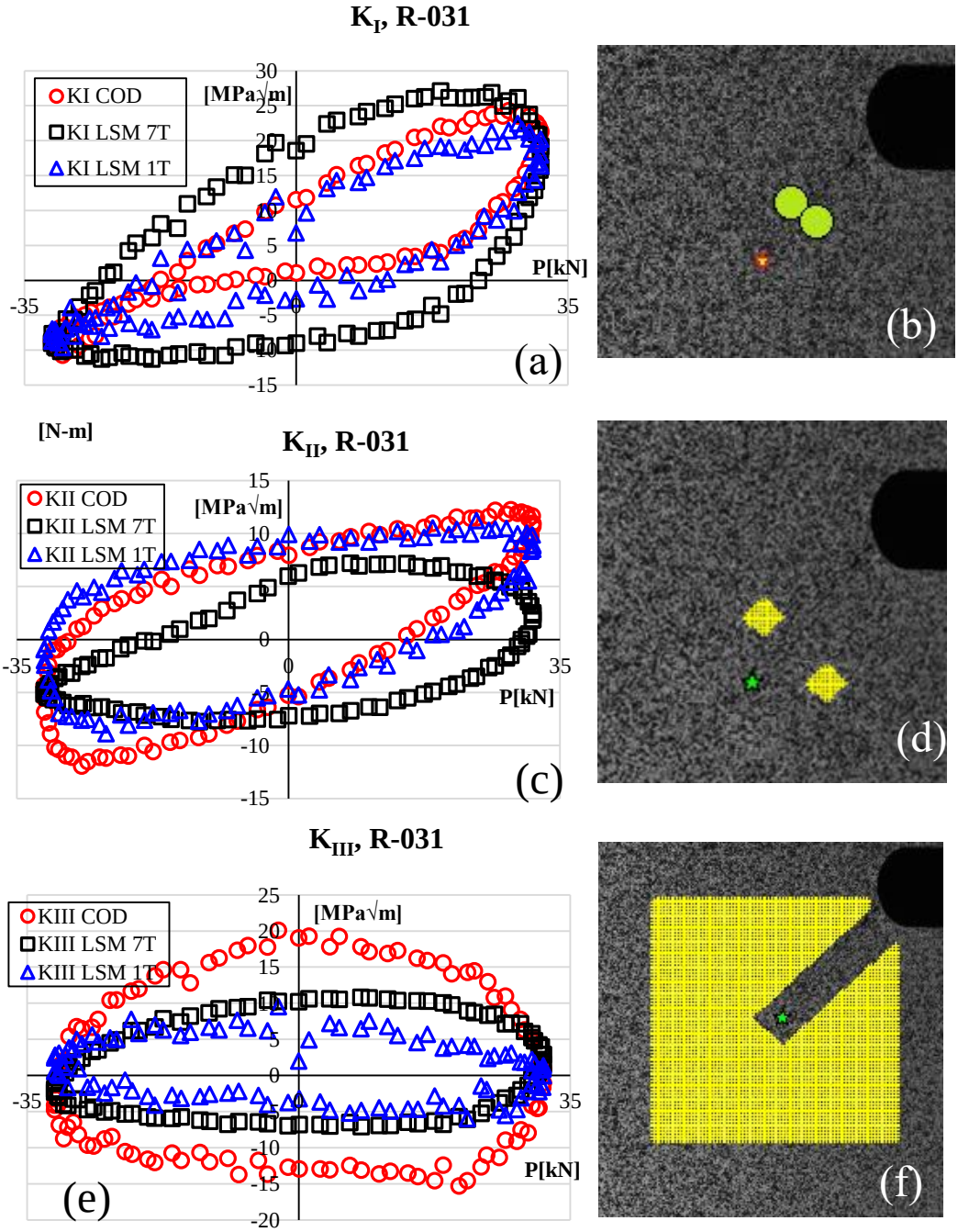

Figure 5-44. Three modes SIF for specimen R-031 at 28000 cycles: a) K_I results from COD, LSM with 7 terms and LSM with 1 term; b) points used for COD method; c) K_{II} results from COD, LSM with 7 terms and LSM with 1 term; d) AOI for LSM with 1 term; e) K_I results from COD, LSM with 7 terms and LSM with 1term; f) AOI for LSM method with 7 terms.

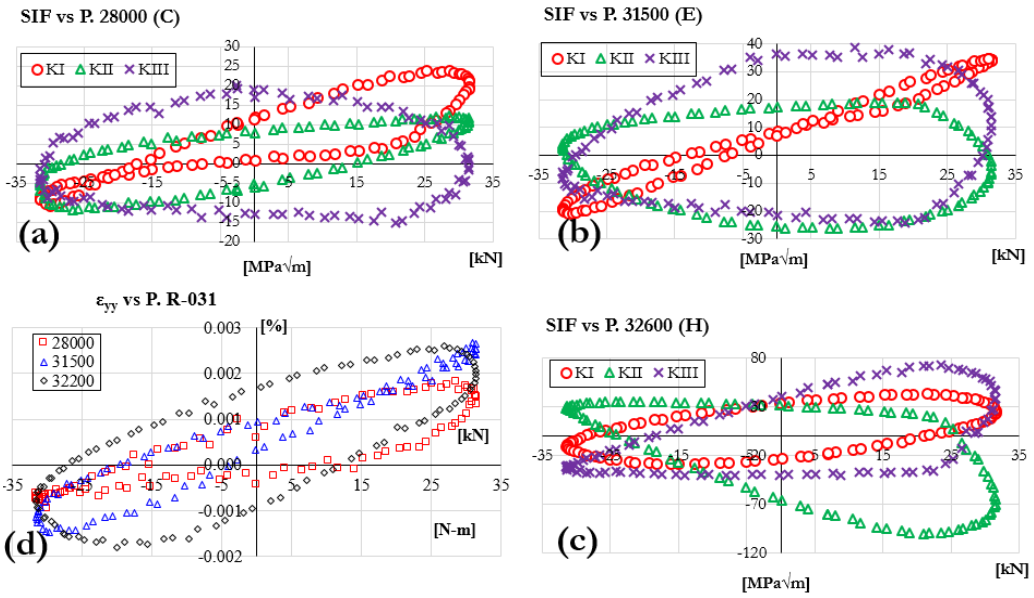

Figure 5-45. SIF (from COD method) versus axial force for selected crack lengths along the kinked crack path (a) 28000 cycles or point C in Figure 5-43a; (b) 31500 cycles or point F in Figure 5-43a; (c) 32600 cycles or point H in Figure 5-43a; (d) applied axial load versus torque for specimen R-031.

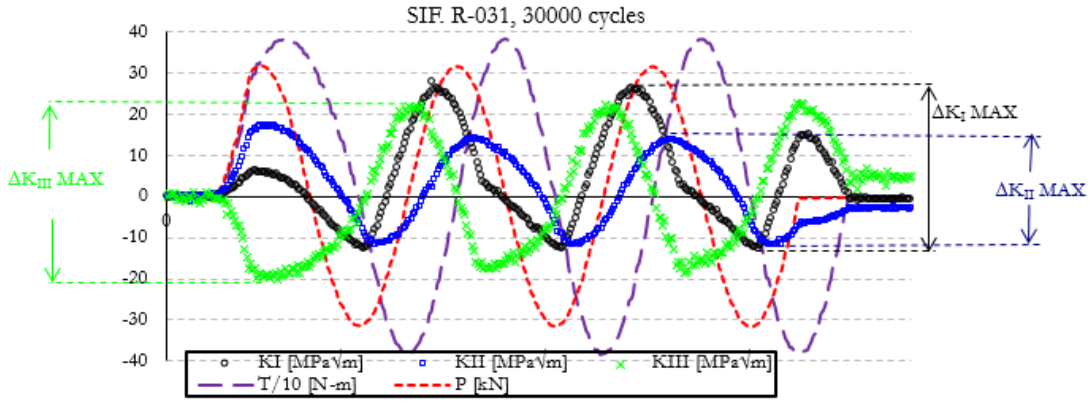

Figure 5-46. SIFs variation and maximum SIF ranges as calculated from the COD method after 30000 load cycles for a 9.28 mm crack, point D in Figure 5-43a.

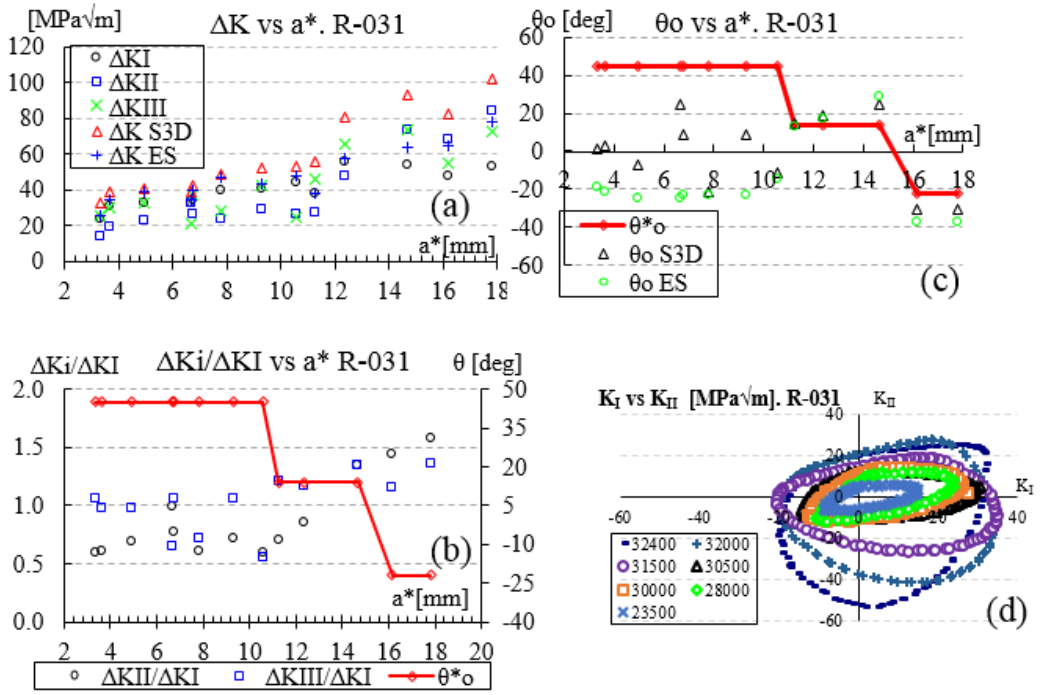

Figure 5-47. Crack tip parameters measured and calculated for specimen R-031, axial load 32 kN and 382N-m max. torque (a) Evolution of mode I, II and III and equivalent SIF ranges versus crack length (b) variation of the maximum II and III over maximum mode I ranges and θ*o versus crack size, (c) θ*o, θo ES (Erdogan-Sih) and θo S3D (Schöllmann et. al.) versus crack length; (d) mode-mixity ratio during one cycle and from cycle to cycle.

Figure 5-47a shows the evolution of SIF and equivalent SIF range values along the crack growth. The influence of ΔK_{III} turns out to be very important, making the equivalent 2D and 3D SIF calculated ranges differ reasonably. The ratios between cycle maximum values of ΔK_{II} and ΔK_I change (and grow) considerably. Figure 5-47b shows the variation rate of the maximum II and III mode ranges over maximum mode I range with crack size along with experimentally determined crack-path tangent angle θ*o. It can be seen that the ratio $\Delta K_{II} / \Delta K_I$ is above 0.5 for the first path kink and above 1.0 after the second path kink. Additionally, it is clearly noted that for this case of out-of-phase loading the ratio $\Delta K_{II} / \Delta K_I$ changes not only during a cycle but also from cycle to cycle. It is noteworthy to remember that in these experiments, the nominal out-of-phase loading ratio, $\Phi = \tau / \sigma = T / F$, was maintained constant from cycle to cycle; in

other words, it was not changed abruptly, see Figure 5-46. Therefore, local conditions, as local specimen geometry and crack path were the significant variables influencing change in mode-mixity rates K_{II}/K_I and $\Delta K_{II} / \Delta K_I$. Figure 5-47c shows the experimentally observed θ*o angle and the calculated (Erdogan-Sih θo ES and Schöllmann et al. θo S3D) crack-path tangent angles for each crack length. The way these angles are presented would enforce coincidence with experimentally measured and calculated path-directions. That is seen in some cases for the determined Schöllmann et. al. angles, but it is not seen for the Erdogan-Sih angles. The explanation comes from the fact that the 3D analyses take into consideration the large ΔK_{III} values which are not accounted for in the ES model. Figure 5-47d shows how mixed-mode ratios (K_{II} versus K_I) change during one cycle and from cycle to cycle for specimen. Mode-mixity variation occurs inside each cycle and gets accentuated when the crack grows with the number of cycles.

Table 17 shows experimental results for specimen R-031: named points as in Figure 5-43a number of cycles (N), crack length (a*) in mm, SIF ranges in MPa√m that occur at maximum ΔK_I as depicted in Figure 5-46, experimental angle θ*o, Erdogan-Sih (θo ES) calculated angle, Schöllmann et. al. (θo S3D) calculated angle, Erdogan-Sih and Schöllmann et al SIF ranges in MPa√m. The last two are the SIF ranges produced by the evaluation of Eq. (55) and Eq. (56) and the method proposed in section 4.5, using the schema shown in Figure 4-10 and calculations from Eq. (57) and Eq. (58), as shown in section 4.5.

As a comparison, the same quantities are presented in Table 18, but this time using the maximum SIF range for each cycle regardless of when they occur. It shows results for specimen R-031: number of cycles (N), accumulated crack length (a*) in mm, maximum SIF ranges in MPa√m, Erdogan-Sih (θo ES) calculated angle, Schöllmann et. al. (θo S3D) calculated angle, Erdogan-Sih and Schöllmann et. al. SIF (ranges in MPa√m). It can be seen how both ES and S3D SIF ranges and kink angles differ from the presented values in Table 17. This is explained by the fact that, whereas the values presented in Table 17 are calculated with the concurrent SIF, the values of Table 18 are done so with the maximum values in spite of when they happen. In Figure 5-46, it is seen that at the time of any K_I, K_{II}, and K_{III} present a smaller value than their respective ranges. Therefore, the difference observed in ΔK ES and ΔK S3D between Table 17 and Table 18.

Table 17. Experimental and calculated parameters for specimen R-031

Point	N	a*	ΔK_I	ΔK_{II}	ΔK_{III}	θ*o	θo S3D	θo ES	ΔK S3D	ΔK ES
-	23500	3.34	24.1	6.8	12.0	45	1	-19	33.2	26.07
A	24000	3.66	31.2	12.7	6.4	45	3	-21	39	34.86
B	26000	4.93	33.3	17.6	2.4	45	-7	-25	40.8	39.1
-	27000	6.68	33.1	4.0	8.9	45	25	-25	39.4	34.97
C	28000	6.76	35.0	16.5	7.0	45	9	-23	42.9	40.33
-	28500	7.79	39.9	22.3	11.3	45	-21	-23	49.3	47.12
D	30000	9.28	40.6	10.9	15.8	45	9	-23	52.6	43.66
-	30500	10.58	44.8	11.2	17.2	45	-11	-15	53	47.55
-	31000	11.26	38.2	5.9	16.9	14	15	13	56	38.63
E	31500	12.38	55.9	2.1	15.5	14	19	17	80.9	57.32
F	32000	14.67	54.6	9.9	27.6	14	25	29	93.1	64
-	32200	16.17	47.6	15.4	7.1	-22	-31	-37	82.9	64.57

G	32400	17.81	53.5	49.0	29.6	-22	-31	-37	101.9	78.51
H	32600	22.06	75.0	64.9	55.4	-22	-31	-39	171	123.3

Table 18. Experimental and calculated parameters for specimen R-031 using maximum SIF ranges for each cycle

N	a*	ΔK_I	ΔK_{II}	ΔK_{III}	θo S3D	θo ES	ΔK S3D	ΔK ES
23500	3.34	24.09	14.41	25.69	-37	-43	45.83	33.12
24000	3.66	31.23	19.23	30.51	-37	-44	57.63	43.48
26000	4.93	33.26	23.09	32.54	-38	-47	63.29	48.88
27000	6.68	33.06	33.02	21.55	-51	-52	64.88	59.10
28000	6.76	35.01	26.91	36.96	-41	-48	70.57	54.10
28500	7.79	39.86	24.41	28.48	-40	-43	66.04	55.36
30000	9.28	40.61	29.03	43.09	-41	-47	80.40	60.53
30500	10.58	44.83	26.65	25.07	-40	-44	69.35	61.48
31000	11.26	38.25	27.18	46.44	-39	-46	80.14	56.84

31500	12.38	55.85	48.13	65.61	-46	-50	121.48	91.70
32000	14.67	54.57	73.54	73.43	-50	-58	147.31	118.34
32200	16.17	47.64	68.48	55.26	-54	-58	126.85	108.06
32400	17.81	53.51	84.79	72.90	-55	-60	156.50	130.17
32600	22.06	75.02	142.96	122.34	-56	-61	254.46	209.59

5.3.5
Specimen under 45º phase axial-torsional alternated load (R-033)

This section presents exemplary and typical results determined for specimen R-033. Two cracks started at the slit notch boundaries, one at the left and another at the right notch boundary. Figure 5-48 shows how the angle of principal stress, $\theta_i=-2\tau_{xy}/(\sigma_{xx}-\sigma_{yy})$, changes with the variation of applied nominal stress (σ_{yy} and τ_{xy}).

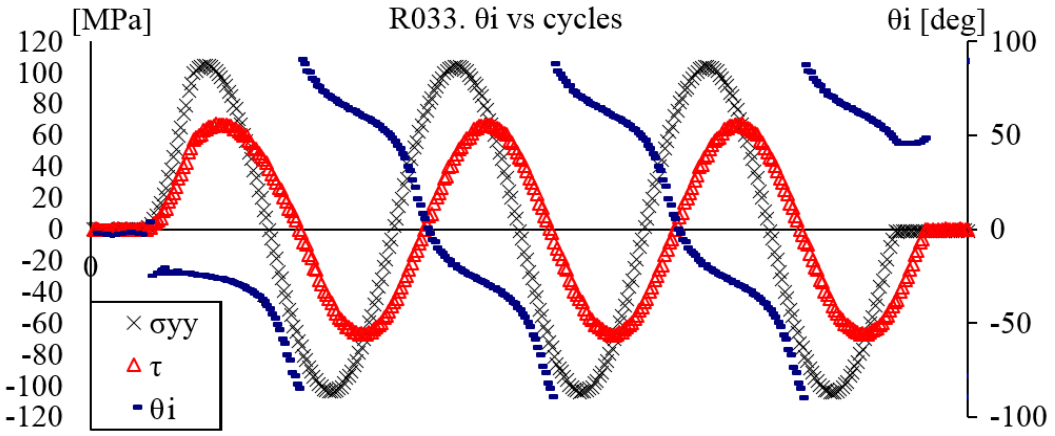

Figure 5-48. Angle of principal stress with applied stress for specimen R-033

Figure 5-49 shows results obtained for the crack that emanated from the slit left notch boundary. The crack initiated at the slit boundary, at 40º, but it continued propagating along an angle direction of approximately 0º relative to the horizontally machined slit-notch. Figure 5-50 shows the AOI and exemplary results for SIF in three modes. Figure 5-51 shows variations of SIFs determined for the three opening modes for three different crack lengths along the kinked crack path. Figure 5-52 depicts SIF variation and ranges after 15,000 load cycles for a crack corresponding to 15000 cycles. Figure 5-53 shows measured and calculated crack tip parameters. Table 18 shows experimental and calculated values for R-033´s parameters. Finally, Table 19 shows maximum SIF ranges and calculated parameters regardless when they occur.

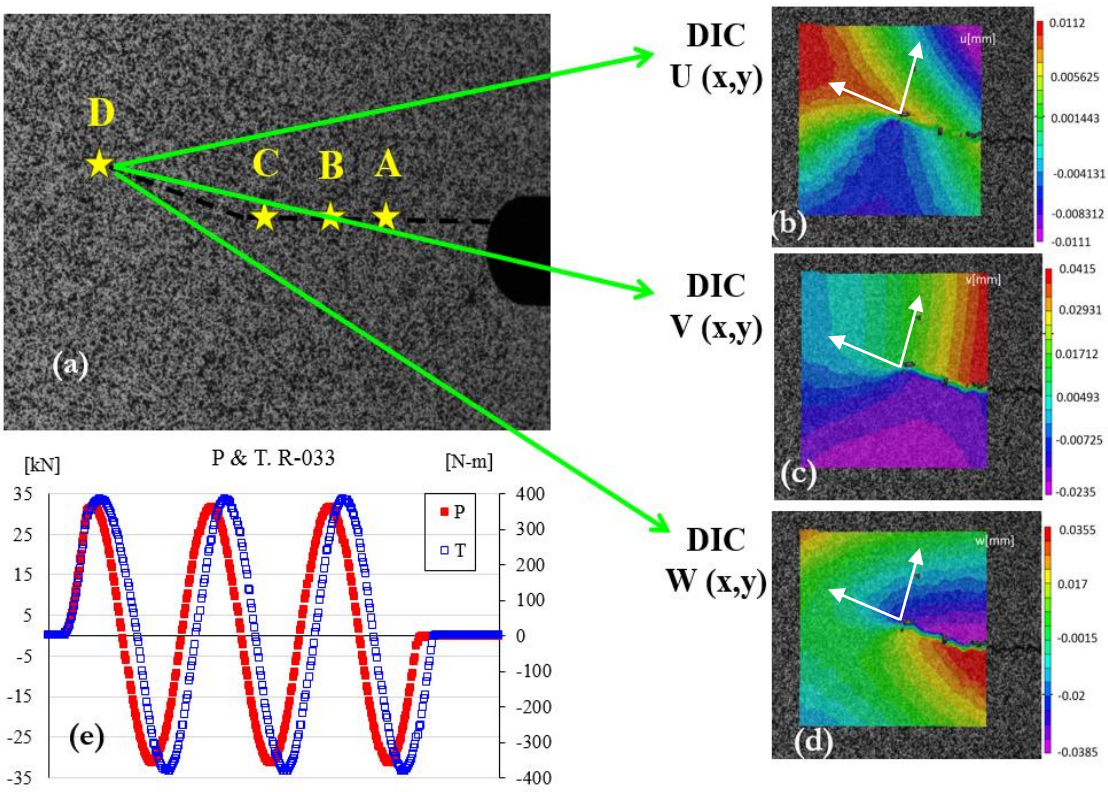

Figure 5-49. Representative R-033 specimen's results: (a) crack path with named CTLs from A to D; (b) parallel-to-the-crack path DIC displacement field for C to D crack path; (c) perpendicular-to-the-crack path DIC displacement field for C to D crack path; (d) DIC out-of-plane displacement field for C to D crack path; (e) applied out-of-phase loads.

Figure 5-49a presents the entire path of the left crack. Some points were marked and denoted from A to D to highlight the path. One abrupt kink angle is shown, about one mm after point C. After kinking, the crack continued growing following a path with angle of about -20º. The u, v and w displacement fields at maximum axial load for point D, given by the VIC-3D® output (rigid motion already compensated), are depicted respectively in Figure 5-49b and Figure 5-49c and Figure 5-49d respectively. Relative motion of the crack flanks can be clearly seen in said figures, as the fields are symmetric over the crack lips. Mode III opening is clearly depicted in Figure 5-49d, in the same way it was seen for specimen R-031. Figure 5-49e shows the nominal 45º out-of-phase loading cycle that was repeated for the entire experiment. About 100 pairs of images were determined at a rate of 10 pairs of images/s for each of the three cycles. Load frequency for these image acquisition cycles was 0.1 Hz.

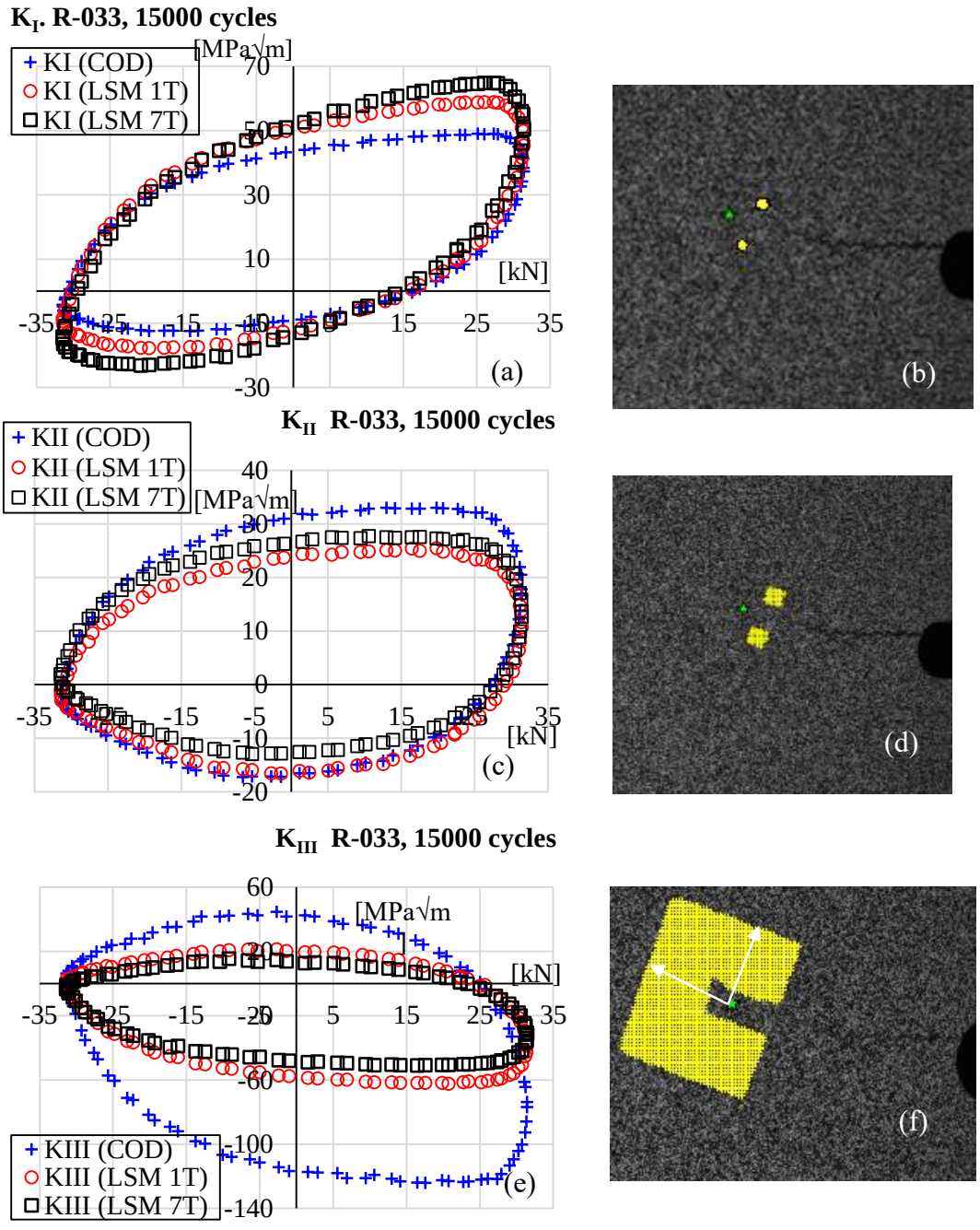

Figure 5-50. SIF for specimen R-033 at 15000 cycles using different data: a) K_I results from COD, LSM with 7 terms and LSM with 1 term; b) points used for COD method; c) K_{II} results from COD, LSM with 7 terms and LSM with 1 term; d) AOI for LSM with 1 term; e) K_{III} results from COD, LSM with 7 terms and LSM with 1term; f) AOI for LSM method with 7 terms.

Additionally for this specimen, SIF values in all three modes using LSM method was performed using the out of plane displacement component as shown in Figure 5-50 for a crack length corresponding to 15000 cycles. Due to the specimen radius, there is an error when approximating a distance between two points in a curved surface by the simple subtraction of coordinates between them, just like it has to be done when calculating the distance from CTL. By keeping said points close, that error is lowered, which has been the idea of the COD method Additionally, and because the compressive applied axial load would create negative strains ahead of the crack tip, possibly generating fictitious K_I values (see section 6.1 for explanation about possible K_I results), the AOI was chosen by selecting two 1 x 1 mm squares located about 1 mm behind the crack tip, as seen in Figure 5-50d. Figure 5-50a, Figure 5-50c, and Figure 5-50e show the comparison for K_I, K_{II}, and K_{III} respectively obtained with COD and LSM methods, using just one and seven terms along with their respective AOI. However, the almost-elliptical K_I variation with both, axial and torsional, loads in Figure 5-50a depicts a non-linear behavior, which is attributed to accumulated plasticity and crack closure.

According to the K_I(COD) curve in Figure 5-50a, the crack opens at about 14kN, it stays open all the way to the maximum axial load, and it closes at about -29kN during the unloading stage. So, SIF mode I must depend on both axial and torsional loads for the crack to remain open at such high compressive load. During that axial load range, if K_I(COD) shows positive values, the crack faces are open therefore they are not touching each other making K_{II} and K_{III} less shielded from rugosity, which would explain the relatively high values for those SIF modes, in addition to the cyclic strain hardening increase produced by the non-proportional loading. It can be also seen how the elliptical behavior for K_{II} and K_{III}, in Figure 5-50c and Figure 5-50e, respectively for both COD and LSM method, represents the crack exhibiting a lag in sliding in those modes while axial unloading occurs. Moreover, the change in sign for K_{II}(COD) and K_{III}(COD) represents the crack shifting sliding directions, which occurs even when the crack is closed probably making the crack surfaces get smoothed under compressive forces.

When comparing SIF performance between specimens under proportional load (R-028, R-029, and R-030) with non-proportional load (R-031 and R-033) one

can see in the second group their behavior does not depend exclusively on either load. The plots of SIF vs. load show one straight and one slightly curved part for the proportional loaded samples, whereas for the non-proportionally loaded samples (Figure 5-44 for specimen R-031 and Figure 5-51 for specimen R-033) is not observed a straight line. That shows SIF dependency on axial and torque loads. While for proportional load, K_I shows a proportionality to the positive part of loading, non-proportionally load specimens (R-031 and R-033) show an elliptical behavior.

The chosen area for LSM method, Figure 5-50f, has to be carefully chosen as to make sure the displacement field is rotated with the crack. In other words, the part of the displacement field perpendicular to the straight part of the crack, until point C in Figure 5-49a, needs to be left out for the subsequent crack lengths after the kink.

The variation of all SIF modes during one cycle for three selected crack lengths versus applied axial load are depicted in Figure 5-51a for point B for 13000 cycles, Figure 5-51b for point C for 14000 cycles, and Figure 5-51c for point D for 15000 cycles. All SIF values were calculated using the COD method. The perpendicular-to-crack strains taken about 1 mm ahead of CTL for crack lengths before (13000 cycles) and after the kink (14500 cycles), are shown in Figure 5-49d. The strains follow a path very different for ascending and descending loads. It seems the kink created blunting represented by the strains showing a rather elliptical behavior after the kink than the sharper shape seen before.

Figure 5-52 shows the three SIF mode variations and respective ranges calculated from the COD method after 14,000 load cycles for a crack sizing 4.96 mm, point C of Figure 5-49a. It can be seen that peaks of the three opening mode SIFs occur out-of-phase and that mode III SIF is larger than SIFs for mode I and II. The peak of mode III SIF occurs for the positive parts of mode I SIF, which is when the crack was completely opened. Furthermore, K_I(COD) seems to show the crack faces did not close, as it does not present a flat slope at axial load negative values as opposed to specimens R-028 and R-030.

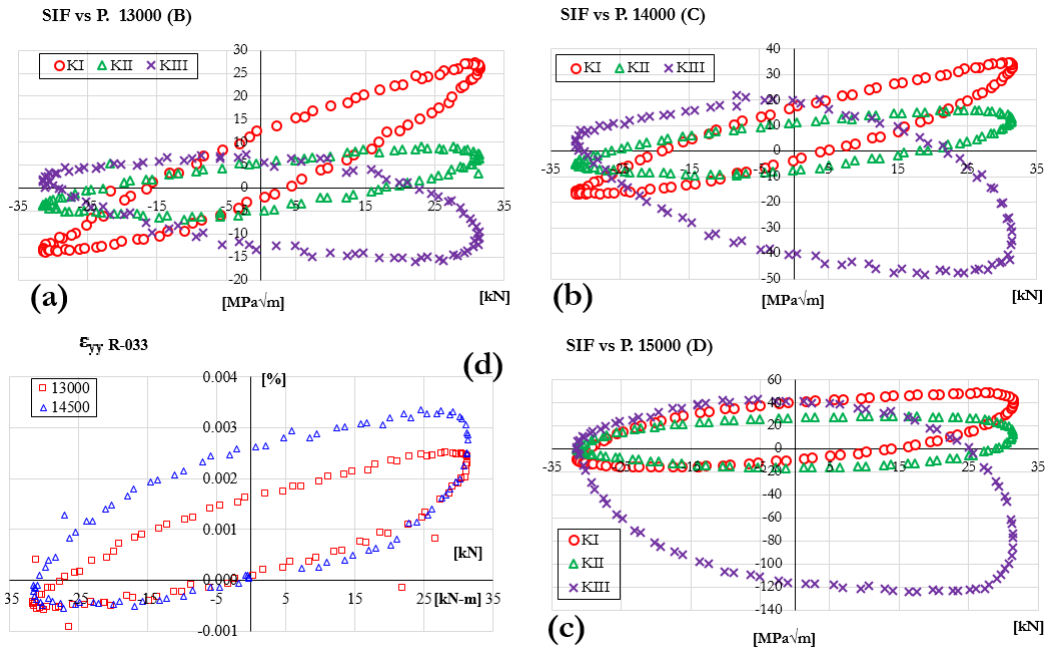

Figure 5-51. Specimen R-033´s SIF for three crack lengths along the kinked crack path (a) 13000 cycles or point B in Figure 5-49a; (b) 14000 cycles or point C in Figure 5-49a; (c) 15000 cycles or point D in Figure 5-49a; (d) perpendicular-to-crack strains for crack lengths before and after the kink.

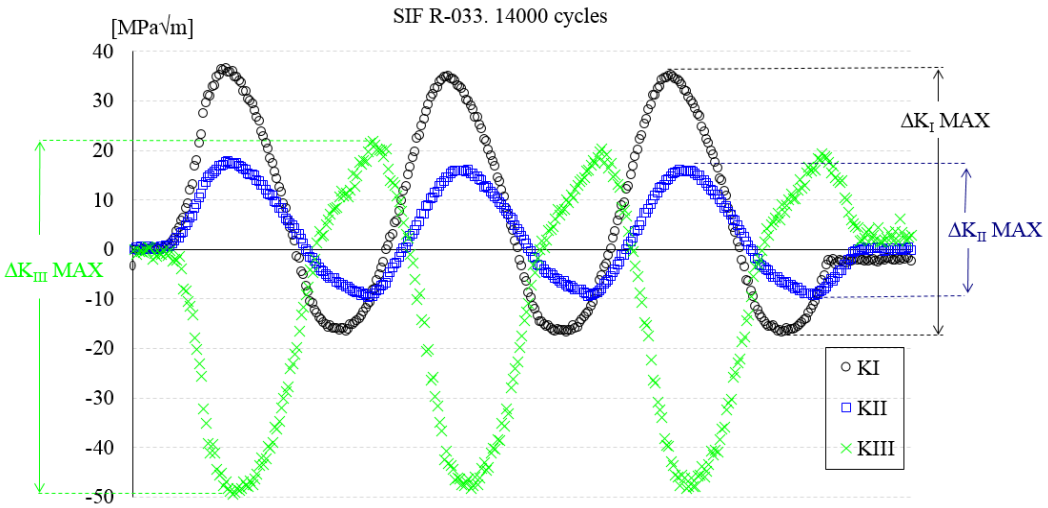

Figure 5-52. All mode SIF variations and ranges calculated from the COD method for specimen R-033 after 14,000 load cycles for a crack sizing 4.96 mm, point C of Figure 5-49a

Figure 5-53a shows the evolution of SIF and equivalent SIF range values along the crack growth. All SIF values were calculated using the COD method. The

ratios between cycle maximum values of ΔK_{II} and ΔK_{I} change (and grow) considerably. Again, and just like in specimen R-031, the influence of ΔK_{III} turns out to be very important, making the equivalent 2D and 3D SIF calculated ranges differ reasonably. Figure 5-53b shows experimentally observed θ*o angle and calculated (Erdogan-Sih θ*o ES and Schöllmann et al. θ*o S3D) crack-path tangent angles for each crack length. Calculated θ*o S3D angles are closer to observed angle than θ*o ES. Again, and just like in specimen R-031 the explanation comes from the fact that the 3D analyses take into consideration the large ΔK_{III} values. Figure 5-53c shows the variation rate of the maximum II and III mode ranges over maximum mode I range with crack size along with experimentally determined crack-path tangent angle θo. It can be seen that the (interpolated) ratio $\Delta K_{II} / \Delta K_{I}$ is bigger than 0.5 before the crack kinks, and also the ratio $\Delta K_{II} / \Delta K_{I}$ changes not only during a cycle but also from cycle to cycle as the slopes vary for the different measured points.

Figure 5-53d shows how mixed-mode ratios (K_{II} versus K_{I}) change and grow during one cycle and from cycle to cycle for the specimen. As commented above, the present set of experiments always maintained constant the nominal out of phase loading ratio $\Phi = \tau / \sigma = T / F$ from cycle to cycle. Hence, local conditions, such as local specimen geometry and crack path were the significant variables affecting the change in mode-mixity rates K_{II} / K_{I} and $\Delta K_{II} / \Delta K_{I}$. This nonstop mode-mixity change is clearly illustrated in Figure 5-53d.

Table 19 shows experimental results for specimen R-033 concurrent SIF: named points as in Figure 5-49a number of cycles (N), accumulated crack length (a*) in mm that occur at maximum ΔK_{I} as depicted in Figure 5-52, SIF ranges in MPa√m, experimental angle θ*o, Erdogan-Sih (θo ES) calculated angle, Schöllmann et. al. (θoS3D) calculated angle, Erdogan-Sih and Schöllmann et al SIF ranges in MPa√m. The last two are the SIF ranges produced by the evaluation of Eq. (55) and Eq. (56), and the method proposed in section 4.5, using the schema shown in Figure 4-10 and calculations from Eq. (57) and Eq. (58), as described in section 4.5.

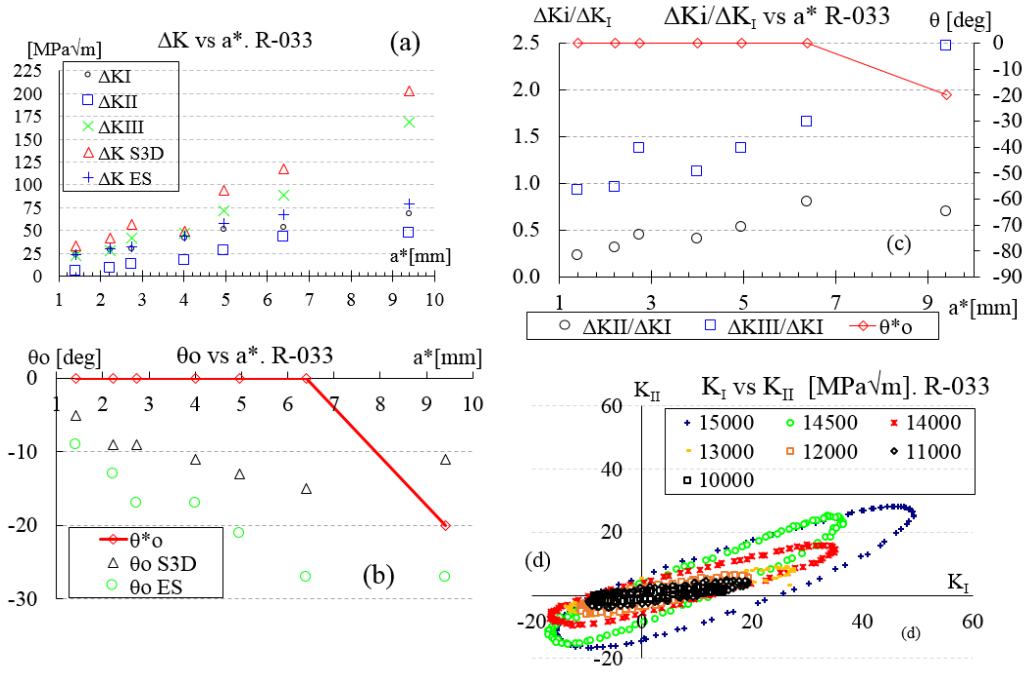

Figure 5-53. Crack tip parameters measured and calculated for specimen R-033, axial load 32 kN and 382N-m max. torque (a) Evolution of mode I, II and III and equivalent SIF ranges versus crack length (b) variation of the maximum II and III over maximum mode I ranges and θ*o versus crack size, (c) θ*o, θo ES (Erdogan-Sih) and θo S3D (Schöllmann et. al.) versus crack length; (d) mode-mixity ratio during one cycle and from cycle to cycle.

As a comparison, the same quantities are presented in Table 20 but instead using the maximum SIF range for each cycle. It shows results for specimen R-033: number of cycles (N), accumulated crack length (a*) in mm, maximum SIF ranges in MPa√m, Erdogan-Sih (θo ES) calculated angle, Schöllmann et. al. (θo S3D) calculated angle, Erdogan-Sih and Schöllmann et. al. SIF (ranges in MPa√m). It can be seen how both ES and S3D SIF ranges and kink angles differ from what is presented in Table 19. This is explained by the fact that, whereas the values presented in Table 19 are calculated with the concurrent SIF, the ones in Table 20 are done so with the maximum values regardless of when they occur. In Figure 5-52, it is seen that at the time of any K_I K_{II}, and K_{III} present a smaller value than their respective ranges. That is the difference observed in ΔK ES and ΔK S3D between Table 19 and Table 20.

Table 19. Experimental and calculated parameters for specimen R-033

Point	N	a*	ΔK_I	ΔK_{II}	ΔK_{III}	θ*o	θo S3D	θo ES	ΔK S3D	ΔK ES
-	10000	1.41	23.8	3.6	11.3	0	-5	-9	33.2	24.03
-	11000	2.22	29.3	6.4	16.2	0	-9	-13	41.4	29.96
A	12000	2.74	30.5	9.8	26.3	0	-9	-17	56.5	32.69
B	13000	4.01	42.2	13.3	15.1	0	-11	-17	49.7	43.57
C	14000	4.96	51.9	22.0	53.0	0	-13	-21	93.7	57.71
-	14500	6.39	53.6	34.4	71.1	0	-15	-27	117.9	67.16
D	15000	9.4	68.6	40.6	147.7	-20	-11	-27	203.3	78.92

Table 20. Experimental and calculated parameters for specimen R-033 using maximum SIF ranges for each cycle

N	a*	ΔK_I	ΔK_{II}	ΔK_{III}	θo S3D	θo ES	ΔK S3D	ΔK ES
10000	1.41	23.83	5.57	22.19	-18	-24	38.11	25.63
11000	2.22	29.27	9.25	28.17	-25	-29	48.55	33.08
12000	2.74	30.46	13.49	41.98	-28	-37	63.27	37.52
13000	4.01	42.24	17.12	23.79	-33	-35	59.41	50.69
14000	4.96	51.92	27.55	71.36	-34	-40	109.97	68.06
14500	6.39	53.59	42.94	88.69	-38	-49	134.91	84.61
15000	9.40	68.56	47.49	168.89	-29	-46	218.18	100.65

This section presented SIF results for a DCT sample under mode I, for a modified C(T) under proportional mixed mode (I and II), and for five thin tubes subjected to different loading combinations, pure tension, pure tension-compression loading, pure alternated torsion loading, proportional loading resulting from the superposition of these two, and out-of-phase loading with phase angles of 45° and 90°, which showed a combination of the three opening modes. The SIF were calculated by fitting DIC displacement fields to the Westergaard´s stress function. A way to establish SIF range was also presented.

Finally, the experimentally observed crack angles are reported, as well as the angles predicted by two equivalent SIF criteria.

6. Discussion

6.1 Analysis of SIF and SIF range

In order to extract a suitable SIF and SIF range, an appropriate analysis has to be performed. But before that is discussed, it is noteworthy to clear out that because the SIF is estimated from displacement fields calculated from the reference image taken at load zero, the measured SIF should be interpreted as a SIF [82]. On the contrary, if the selected reference image has a load different than zero, the measured SIF should be interpreted as a SIF range [87]. Moreover, in literature there are plenty of cases where the COD is used to quantify SIF and crack openening with different techniques [40, 67, 88, 92, 93]. Therefore, the measures reported here use widely accepted practices.

For the holed C(T) specimen, in Figure 5-13 one can see that despite the applied load is positive, the crack faces remains closed until about 0.27 P/Pmax. This is due to the fact that the crack was grown under cyclic loading, and the material was an AISI/SAE 1020 steel (a ductile metal with chemical composition shown in Annex A) which created a hardened plastic zone ahead of the CTL as measured by DIC and seen in the strains depicted in Figure 5-9. So, part of the applied load has to be spent overcoming the residual strain, and when it does, the SIF mode I grows proportional to the applied load. In Figure 5-13 the experimentally measured SIF is seen parallel to the numerically calculated SIF by FEM. This is the same phenomena described by Elber in 1970, although measured with a different technique. Therefore, in this thesis, the SIF range is the difference between the maximum and minimum SIF.

The plasticity mechanisms that govern crack closure are directly related to COD [90], which in turn are proportional to SIF. Figure 6-1 shows a comparison of K_I calculated with COD, Eq. (6), and SIF from numerical formulas referenced in

[3], named K Teor, for specimen R-028 for a crack sizing 3.24mm after 11220 cycles. It is observed a difference in values and curve shape, in a similar manner how it was described for Figure 5-18. Results for 11.9 mm crack on modified C(T) specimen. a) SIF, but in this case, the reversal load ratio is -1, giving negative K_I values that need to discussed here.

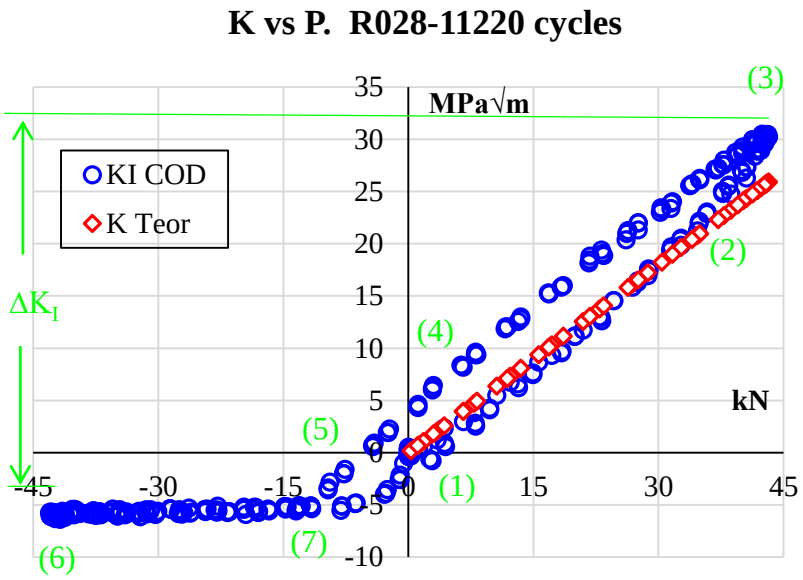

Figure 6-1. Comparison of K_I via COD and numerical formulas for specimen R-028 for a crack sizing 3.24mm and 11220 cycles.

The points 1 to 7 in Figure 6-1 are numbered in order of appearance, and they represent the following: Point 1 represents the reference image used to compare displacements with. It has axial load = 0. So, all displacements, therefore strains, stresses, and SIF are mapped with respect to it. For each measured crack length, the reference image is the initial image at zero load for a selected crack crack lenght instead of using just one image for all the measured crack lengths. That way, the plastic deformation accumulated during fatigue crack growth and not recorded by DIC, is accounted for. Without that precaution, the SIF curve would not start at zero for crack lengths different that the first one, but at positive values. Point 2 denotes the end of the linear elastic deformation therefore, the area around the CTL shows Yield behavior. Point 3 shows the maximum SIF value reached, matching the maximum axial load, and the beginning of load reversal. Point 4 shows the instant

when applied axial load reaches zero, but the crack is still open. It is noted that despite the load is zero, the crack remains open as K_I (COD) is positive, therefore the crack experiences blunting. Point 5 represents the instant when the crack closes as K_I (COD) is zero. At this point, the crack technically does not exists anymore. It is seen there is a need for a compression load to achieve that stage. At point 6, the applied load is minimum and the crack is still closed, compressing its faces therefore making the specimen increase its rigidity. Going from minimum negative, loading is inverted reaching point 7. At point 7, the crack is still closed, its faces experience less compression, and the specimen losses rigidity. Finally at point 1 again, the applied axial load is 0, but the crack is still closed as K_I does not show positive values.

Now, what happens from point to point can be described as follows: from point 1 to point 2, the crack opens with K_I proportional to applied axial load following a straight or quasi-straight line meaning there are linear elastic conditions. From point 2 to point 3, K_I increases more rapidly than from points 1 to 2 with the applied axial force until reaching the maximum crack opening. Plastic deformation is accumulated between those two points. From point 3 to 4, the unloading path is parallel, or quasi-parallel, to the elastic loading path seen from point 1 to point 2. From point 4 to point 5, there is a need to close the open crack even though the applied axial force is zero, as depicted in Figure 6-2. Hence, the accumulated plastic deformation between points 2 and 3 is reversed. From points 5 to 6, the crack is already closed and it does transmit compression between its faces. The applied axial load is consumed on initially deforming the crack rugosity peaks. After that is achieved, the load is spent on compressing the specimen, which is what makes it more rigid. Such rise in rigidity is observed as the quasi-horizontal line from points 5 to 6. As the load decreases, the relative displacement between opposite-to-the-crack points, therefore SIF (calculated from COD) as described in Eq. (6), stays almost constant. From point 6 to point 7, as the load increases, the relative displacement between opposite-to-the-crack points stays the same (the line is almost horizontal). Finally, from point 7 to 0, the line presents an almost imperceptible slope, but it needs to occur in order for the crack to open as the applied axial load is increasing.

With that in mind, the observed negative K_I values represent the closed crack under compression due to the applied negative axial load, inducing negative perpendicular-to-the-crack displacements. Such displacements remain quasi-constant from point 6 to point 7. The crack starts to open at point 7, which for all practical reasons has the same value of point 6, making the SIF range as the difference between the maximum and the minimum measured SIF.

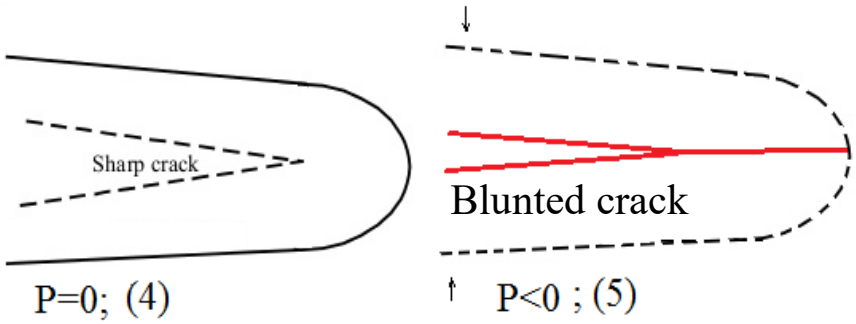

Figure 6-2. Schematic representation of crack experiencing mode I negative relative displacements

Such analysis is correct when the calculated SIF is done using the COD formulation, Eq. (6) or Eq. (7), but for the LSM formulation, Eq. (16), as the SIF versus applied load differ in the compression part as is easily seen in Figure 5-26 for specimen R-028 and Figure 5-39 for specimen R-030. Note that the above analysis is based on observations for specimen R-028 with K_{II} and K_{III} =0.

For specimens R-029 to R-033, where K_{II} and K_{III} are different than zero, the maximum SIF is reduced by crack roughness, and crack friction. On the other hand, they are likely enhanced by crack interlocking as the crack flanks form inclined planes at the micro level increasing the sliding between faces, as suggested by Kibey et. al [90] and Mróz and Mróz [51], especially under negative axial loads. Hence, the SIF range for modes II and III can be calculated by the subtraction of the maximum and the minimum measured SIF.

The thin tubes analyzed here are considered in a plane stress state, so SIF are not expected to vary much along the specimen´s thickness even though the technique used provides surface information only. Moreover, for the three opening modes in the thin tubes, the reported SIF are considered effective SIF, as they already account for non-linearities such as crack closure, crack roughness, crack friction, oxide crack closure, and crack path direction.

6.2
Analysis of equivalent SIF and equivalent SIF range

The evaluation of an equivalent SIF only makes sense when there is more than one SIF mode. As reported in literature crack growth can occur, besides pure mode I, only in mode III [31], mode I and III [32], mode I and II [27] [74] and modes I, II, and III combined [30, 80]. The holed C(T) specimen did not develop visible out-of-plane displacements other than the ones in the very near zone, as described by He and Kotouzov [62]. In the thin tubes and holed C(T) specimens, the displacements in the very near zone were only used to identify the CTL. Besides that, three out of the five thin tubes developed visible out-of-plane displacements that were associated with SIF mode III. So, in order to establish a crack growth law that appropriately describes the experimental results, includes all three SIF modes, accounts for crack kinks, slants, and other non-linearities, an equivalent SIF range model has to be found. This section discusses such results.

The Tanaka, Eq. (46) and Asaro, Eq. (47), equivalent SIF models could only be used to describe loading situations when loads are in-phase and the reversal load ratio is bigger than zero as the square root term would make the equivalent SIF positive. A negative K_I does not make physical sense as the crack faces cannot penetrate each other, so negative perpendicular-to-crack displacements actually do not occur beyond the crack faces. The only possible exception to the previous statement could be the case of crack blunting when the crack is forced to close by a compressive load. In that case, negative K_I values could make sense as reported (from COD method) for the thin tubes in chapter 5. Positive or negative K_{II} and K_{III} values may exist depending on the relative displacements between opposite-to-crack points. Kibey, Sehitoglu, and Pecknold [90] discussed the meaning of negative K_{II} displacements. They stated that when those displacements are different than zero, the crack is slipping forward if $u > 0$, slipping in reverse when $u < 0$ and the crack is said to be sticking if $u=0$. A similar approach could be extended to out-of-plane displacements for the w displacement field. So, negative values of K_{II} and K_{III} are capable of making an equivalent SIF negative. Therefore, in the case of the thin tubes, the Tanaka, Eq. (46) and Asaro, Eq. (47), models cannot be applied as the reverse load ratio is negative, which would produce negative K_{II} and K_{III} values.

The ES equivalent SIF model, Eq. (52), and the Schöllmann et. al., Eq. (53), are implicit equations, as they include the kinking angle, so they cannot be solved directly. Strictly speaking, they were proposed for static or quasi-static loading. However, several authors argue that monotonic loading criteria can be extended to proportional fatigue loading. Highsmith [24], citing work by Tanaka, called it a "straight forward" step. According to Rozumek and Macha [68], who also cited Tanaka´s work, after fitting mixed-mode fatigue test results to Paris rule, a good correlation was found using tensile testing material constants that could be used as well under different loading conditions. This statement supports the claim made in section 6.4, which will be presented ahead. Richard et.al. [22] also claimed that extending the SIF to the SIF range is possible and they also argue that crack propagation will occur when $K_{I,th} < K_{eq} < K_{I,c}$. With those ideas in mind, the validity of ES SIF range, by Eq. (55), and the Schöllmann et. al. SIF range, Eq. (56), is assumed as correct.

The devised schema to evaluate the ES and Schöllmann et. al. SIF ranges presented in section 4.5, using the schema shown in Figure 4-10, and calculations from Eq. (57) and Eq. (58) delivered results shown in Figure 5-28a for specimen R-028, Figure 5-35a for specimen R-029, Figure 5-41a for specimen R-030, Figure 5-47a for specimen R-031, and Figure 5-53a for specimen R-033. For specimen R-028 (pure alternating axial loading) SIF modes II and III were almost non-existent through the measured crack lengths, so there are not evident differences between K_I and ΔK_I. For specimen R-029 (pure alternating torsional loading) the results for the three modes were quite noisy especially for K_{III}, as seen in Figure 5-34. Therefore, there is a visible difference between the ES and the Schöllman et. al. SIF ranges, as K_{III} shows visible values. Despite the noise, the relation K_{II}/K_I remains quasi-constant from cycle to cycle and along the cycle. For the R-030 specimen (in-phase alternating axial and torsional loading), the K_{III} values were very low as shown in Figure 5-40, therefore there is not much of a difference between ES and the Schöllman et. al. SIF ranges and the relation K_{II}/K_I remains quasi-constant from cycle to cycle and along the cycle. According to Highsmith [24], and Yang and Vormwald [80], that ratio could be used to indicate when the crack may curve its path. For the R-031 specimen (out-phase alternating axial and torsional loading with 90^o phase angle), SIF range mode II and III at times presented values larger

than SIF range mode I. Therefore, there is a very visible difference between the ES and the Schöllman et. al. SIF ranges, being the second one larger than the former. The relation K_{II}/K_I changes and grows from cycle to cycle and varies during one cycle, even though the ratio T/F was kept constant during the experiments. If the remote loading ratio does not change, only local conditions could be responsible for the K_{II}/K_I variation. For specimen R-033 (out-phase alternating axial and torsional loading with 45º phase angle), SIFs range mode III presented values larger than SIF range modes I and II. Therefore, there is a very visible difference between the ES and the Schöllman et. al. SIF ranges, being the second one much larger than the first one. The relation K_{II}/K_I changes and grows from cycle to cycle and varies during one cycle though, a little less pronounced than in specimen R-031. Because of the inclined crack, the crack opens perpendicular, slides parallel, and slides out-of-plane to its faces producing K_I, K_{II} and K_{III}, respectively. With and inclined and slanted crack, the three opening modes are not exclusive of individual acting loads, rather than all of them, making K_I and K_{II} vary, giving permanently changing conditions for the crack tip field. That can be seen in figures Figure 5-39a (R-030), where is seen that the crack opens and closes at the same time with either axial or torsional load, while in Figure 5-44 (R-031) and Figure 5-50 (R-033) the crack stays open albeit the axial load is negative but the torque is positive. This means the compressive part of the axial load tends to close the crack but, the torsional load exerts crack sliding. If the crack has rugosity, and when the friction force is surpassed, the torsional load also exerts opening in mode I.

Finally, it can be added that the use of SIF equations for crack on a planar surface on cracks over curved surfaces is acceptable only for short cracks. For long cracks the assumption that points A and B (Figure 2-2) are close enough so the distance to the CTL can be simplified to a straight line loses validity [94] and William´s series, Eq. (6) and Eq. (**7**), simply will not work. This exclusion applies for two of the three tested methods: William´s series using full displacements field and ⌡, whereas for the COD method if the points A and B (Figure 2-2) are kept sufficiently close, between 1 and 3 mm in case of the thin tubes, the curvature does not significantly affect calculations.

6.3
Analysis of crack kinking models

The result of evaluating the crack kinking models displayed in section 3.1 to 3.3 is presented and discussed here.

6.3.1
Analysis of crack kinking models for modified C(T) specimen

Figure 6-3 shows how the crack kinking models, presented in section 3, perform for the modified C(T) sample. The models were evaluated for the maximum K_I and its concurrent K_{II}. It is seen that most of the models perform well, but the MSS, which is shown on a separate scale (right side of Figure 6-3). The low carbon steel is not prone to shear dominated failure and, as shown in Table 10, shear mode is not dominant. Therefore, the MSS is not expected to achieve an accurate prediction, which produced a semi-constant value of 69º, so for the sake of image resolution θMSS is not shown in Figure 6-3. The CTD performs well for short crack lengths but deviated when the crack became longer. As Highsmith [24] suggested, the CTD model works better in short cracks. The Demir criteria does not do a close prediction. Although different equations, the MTS and Richard models are based on the same principle. Results show that there is virtually no difference between them in this specimen. Now, the energy based models do a close prediction. The T-stress (stress parallel to the crack and not reported here) is known to influence brittle fracture when the stress field is result of mode II loading [95] or to impact crack path steadiness [96] in pure mode I under mixed-mode loading when in presence of small imperfections. Finally, the SED criterion, Eq. (39) using Ψ=0º as shown in Table 9, does a close prediction, however running parallel to the observed crack path. One point important here is that the machined hole modified the stress field ahead of the crak tip inducing a SIF mode II in presence of pure mode I loading. This is contrary to the case of applied mixed mode loading that produces SIF mode II inducing a change in the stress field ahead of the crack tip. Perhaps such difference in the origin of the stress field is what might explain the relatively low K_{II} values and difference in crack kinking angles.

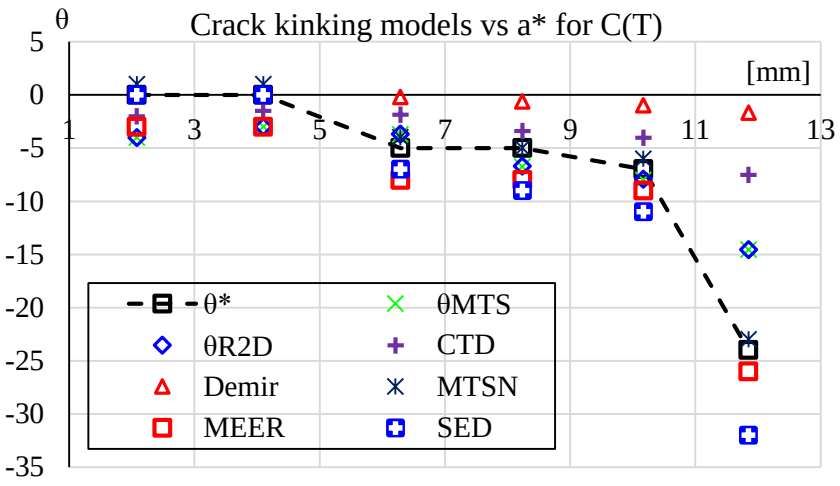

Figure 6-3. Evaluation of crack kinking models for modified C(T) sample

6.3.2
Analysis of crack kinking models for specimen R-029

Figure 6-4 shows the performance of the studied crack kinking models presented in section 3.1 to 3.3 using maximum SIF range that occurs at maximum ΔK_I for each measured crack length. Because ΔK_{III} is present, the Richard 3D criterion is also evaluated here. Moreover, the presented angles are referenced to the sample´s horizontal axis.

From the stress based criteria, it is seen that the MTS does the closer prediction even though there are a couple points that are off the general tendency (K_{II} unexpectedly presented low values at those same points). Richard 2D, as it does not account for sliding mode III, seems to do the furthest prediction. The MSS criterion performs much better when the $\Delta K_{II}/\Delta K_I$ ratio is above 0.5. It is expected that as the crack turns, shear mode becomes more dominant hence, the MSS should describe the crack growth. The MTSN and MEER energy based models are off as they do not account for the present K_{III} values. The SED model, Eq. (39b) using $\Psi=0^o$ as shown in Table 9, on the other hand does account for K_{III}, and it does an excellent prediction even though for the first two values of cracks lengths, the criterion returns about the same Strain Energy Density value when the evaluated angle ranges between -45 to 45 degrees. Therefore, the presented value for SED is the value that would get the closest to the observed path.

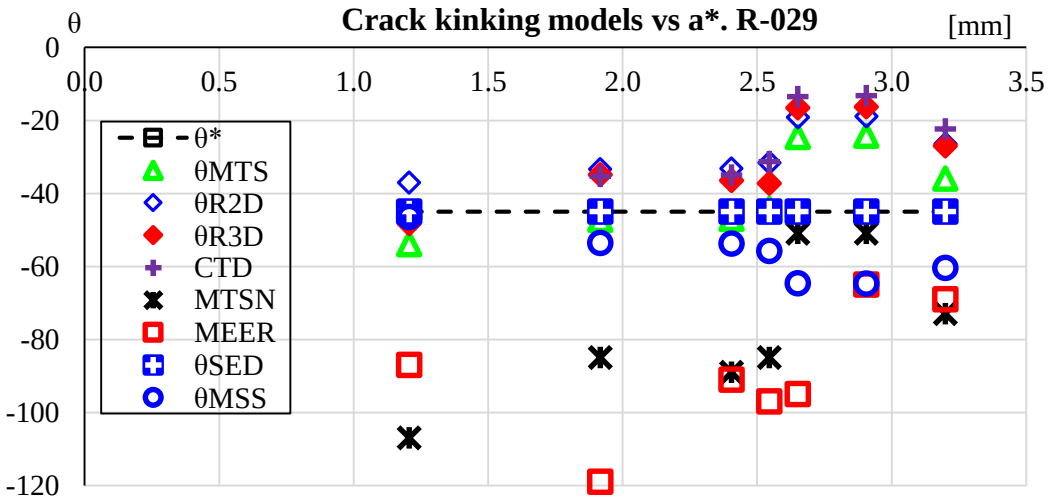

Figure 6-4. Results for crack kinking models evaluation.

6.3.3
Analysis of crack kinking models for specimen R-030

Figure 6-5 shows how the crack kinking models, presented in sections 3.1, 3.2 and 3.3, fare against crack length. They were evaluated using the maximum SIF range occurring simultaneously with maximum ΔK_I, as shown in Figure 5-40. Although small, ΔK_{III} is present, therefore the Richard 3D model is also evaluated here. Moreover, the presented angles are referenced to the sample´s horizontal axis. From the stress based criteria, it is seen that the Richard 2D criteria does the closer prediction even though it is off for about 10º. Richard 3D and MTS criteria seem a little off by about 20º. The MSS does not perform well, predicting a semi constant kinking angle of about -55º as the $\Delta K_{II}/\Delta K_I$ ratio does not change much for the entire experiment. The CTD returns a constant value between -30º to -35º, similar to the R2D criterion. The MTSN and MEER energy based models are way off showing opposite signs. The SED model, Eq. (39b) using Ψ=0º as shown in Table 9, on the other hand, does an excellent prediction despite a couple of points where it is completely off.

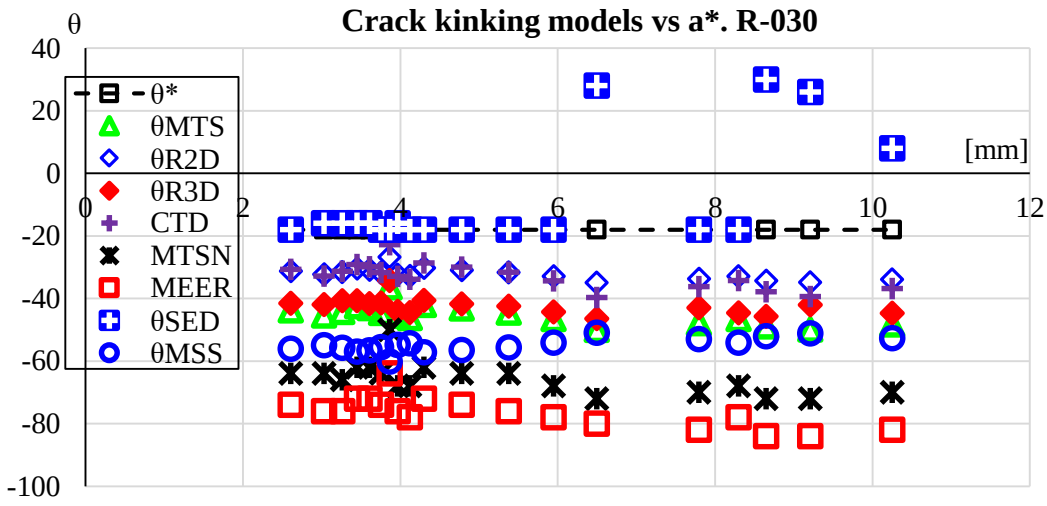

Figure 6-5. Crack kinking models for R-030

6.3.4
Analysis of crack kinking models for specimen R-031

Figure 6-6 shows how the crack kinking models, presented in sections 3.1, 3.2 and 3.3, perform against crack length for specimen R-031. Because ΔK_{III} is present in this sample, the Richard 3D model is also evaluated here, but not the R2D as it does not include SIF mode III. It has to be noted here, that because in this specimen the ratio σ/τ changes along the cycle, the models do not predict a constant kinking angle as opposed to the previous samples. Nonetheless, they were evaluated using the maximum SIF range occurring simultaneously with maximum ΔK_I, as shown in Figure 5-46. Moreover, the presented angles are referenced to the sample´s horizontal axis. From the stress based criteria, MTS, and R3D are very close within each other (separated between 0 to 10º) but far from the experimentally observed angle. This is surprising as there is visible difference in mode III SIF values. However, one must remember that those models were deducted for proportional loading, and this is not the case here. The MSS predicts a kinking angle of about -60º until the second kink where becomes closer as the crack grows. This happens as the $\Delta K_{II}/\Delta K_I$ starts to change and goes above 0.5. The CTD criterion returns similar values found in the three stress-based criteria.

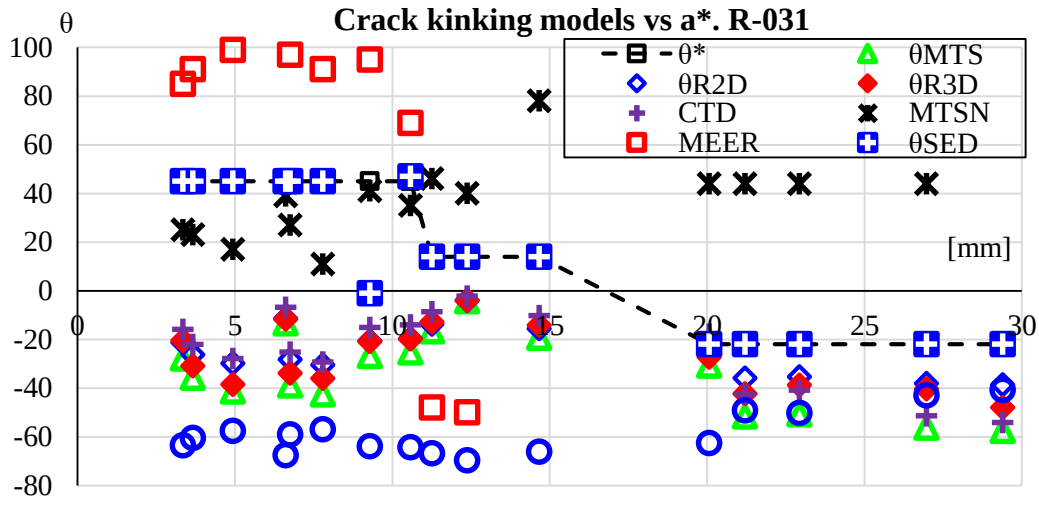

Figure 6-6. Crack kinking models evaluated with experimentally obtained SIF values.

The MEER models is way off in values, however running kind of parallel to the crack angle. Additionally for this criterion, there was no convergence for some crack lengths. The MTSN model comes closer before the first kink but after that, it stays away from the experimentally observed crack kinking values. Just as a reminder, the MTSN and MEER do not account for K_{III}. Finally, for 11 of the 15 evaluated crack lengths, the SED criterion, Eq. (39b) using $\Psi=0^o$ as shown in Table 9, exhibited symmetry of minimum strain energy density values at negative and positive values of the evaluated θ angle. The presented values here are the middle of such range. With that in mind, the SED model does a very close prediction to the observed angle.

6.3.5
Analysis of crack kinking models for specimen R-033

Figure 6-7 presents how the crack kinking models, presented in sections 3.1, 3.2 and 3.3, perform against crack length for specimen R-033. Because ΔK_{III} is present in this sample, the Richard 3D model is also evaluated here, instead of the R2D model. It has to be noted here, that because in this specimen the ratio σ/τ changes along the cycle (the same as with sample R-031), the models do not predict a constant kinking angle as opposed to the previous samples. Nonetheless, they were evaluated using the maximum SIF range occurring simultaneously with

maximum ΔK_I, as shown in Figure 5-52. Moreover, the presented angles are referenced to the sample´s horizontal axis. From the stress based criteria, MTS, and R3D are close to each other (separated between 3 to 12º) but at least 12º away of the experimentally observed angle. The MSS predicts a kinking angle between -65º to -55º until the kink appears, when it start to hover at about -55º. This happens as the $\Delta K_{II}/\Delta K_I$ starts to change and goes above 0.5 and staying about 0.6. The CTD returns values similar to the stress-based criteria but a little closer than they do.

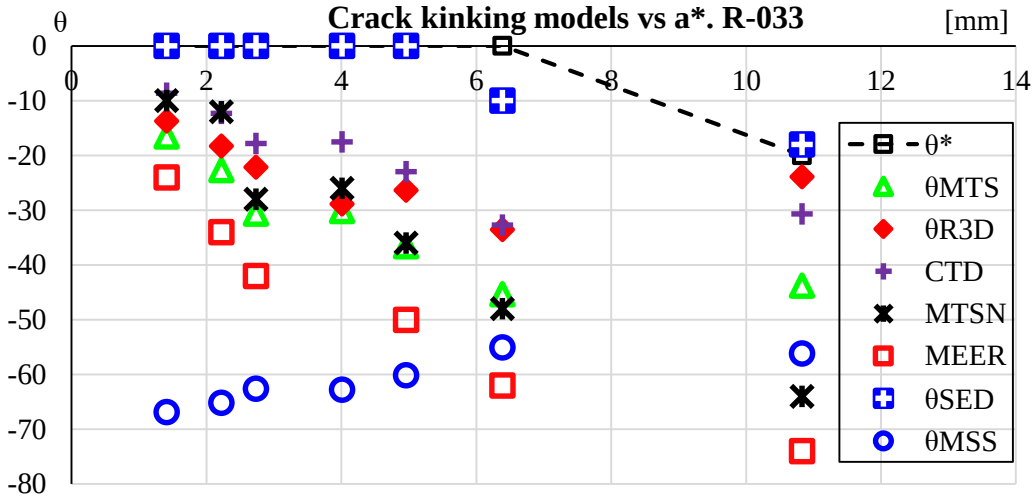

Figure 6-7. Crack kinking models for sample R-033

The MEER models is way off in values with an enlarging difference as the crack grows. Additionally for this criterion, there was no convergence for one crack length. The MTSN model comes closer than the MTSN but, it is still far away from the experimentally observed angle. Just as a reminder, the MTSN and MEER do not account for K_{III}, whereas the SED criterion, Eq. (39b), does consider it. Finally, just before the first kink, the SED exhibited a constant minimum value when the evaluated θ angle ranges from 6º to14º. The presented values here are the middle of such range. With that in mind, the SED, Eq. (39) using Ψ=0º as shown in Table 9, does a very close prediction to the observed angle. A summary of the performance for the SED crack kinking criterion for four out the five thin tubes is presented inFigure 6-8. It can be seen how the SED really does a good job predicting crack path direction Although literature [24] described the SED as not able to describe shear dominated fracture well, in this thesis, the materials used were ductile so that case does not apply.

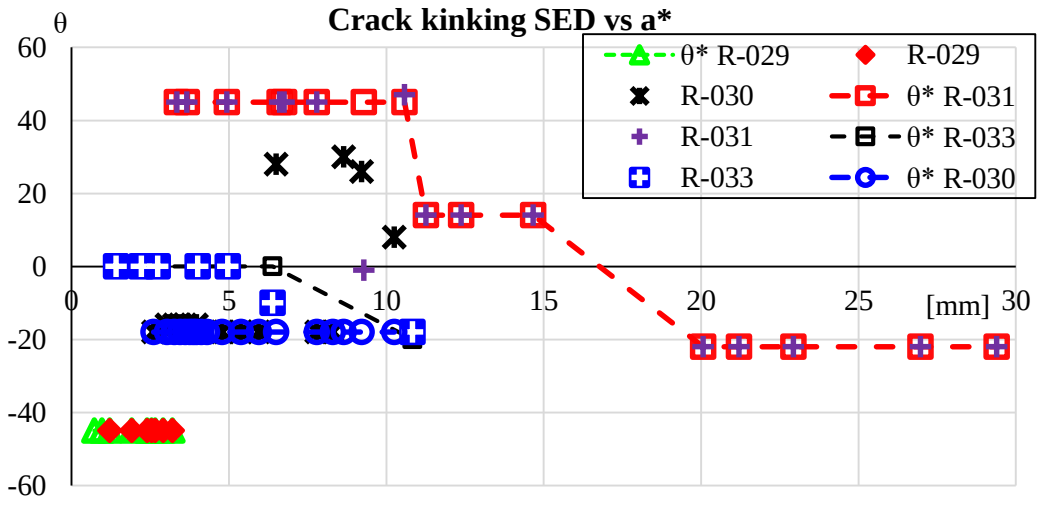

Figure 6-8. Summary of SED model for thin tubes

Highsmith [24] observed that stable crack growth remains co-planar under continuous K_I loading, and it will only deviate from the original path (by a $\Delta\theta$) when in presence of K_{II}. Now for alternating loads, using the assumption of exchanging SIF for SIF range, exploited in section 6.2, crack growth will swerve from its initial path (also by a $\Delta\theta$) when some ΔK_{II} is exerted on the crack. That is observed in the plots of $\Delta K_{II}/\Delta K_I$ versus crack kinking angle in Figure 5-21 for the modified C(T), Figure 5-35b for R-029, Figure 5-41b for R-030, Figure 5-47b for R-031, and Figure 5-53c for R-033 specimens. Furthermore, Kibey et. al. [90] had stated that crack kinking produces an abrupt decrease in mode I SIF and a matching increase in mode II SIF. Therefore, making the ratio K_{II}/K_I higher. If such criteria can be extended in the same way that Richard et. al. [22] and Rosumek et. al. [68] use it to establish an equivalent SIF range from equivalent SIF expressions, the results obtained in this thesis show that it is evident how cracks turn when ΔK_{II} becomes significant, something, as observed by Yang [26], in the vicinity of $\Delta K_{II}/\Delta K_I > 0{,}5$. So at that ratio, there is crack grow transition between normal stress (MTS dominated) and shear stress (MSS dominated), whereas $\Delta K_{II}/\Delta K_I$ ratios bigger than 1.5 are completely MSS dominant [26]. However, $\Delta K_{II}/\Delta K_I$ is not the only describing parameter. There were seen cases with high mode-mixity where the crack did not turn and cases with low mode-mixity where the crack indeed turned such as for the modified C(T) specimen, see Figure 5-21. In that particular case, there is a hypothesis regarding on how the K_{II} values are hindered by crack closure and crack

rugosity [90] and how the T-stress could influenced crack path [96]. That hypothesis would account for the apparent lower K_{II}/K_I ratio (see Figure 5-21) that could help discern the moment where the crack growth process changes from MTS to MSS dominance.

6.4
Analysis of FCG using Paris rule and equivalent SIF range

This section aims to answer whether the da/dN curve represents FCG even for cases when there is multiaxial loading, variable mode-mixity and crack kinking.

Total crack length results were calculated from the summation of partial crack lengths (resulting in values defined as a*) that were measured along each crack growth increment including the presence of kink angles, which occurred in specimens R-031 and R-033.

With that in mind, Figure 6-9 shows the Paris curve using the Erdogan-Sih formulation for equivalent ΔK as presented in tables 11, 13, 15, 17 and 19 for each cycle.

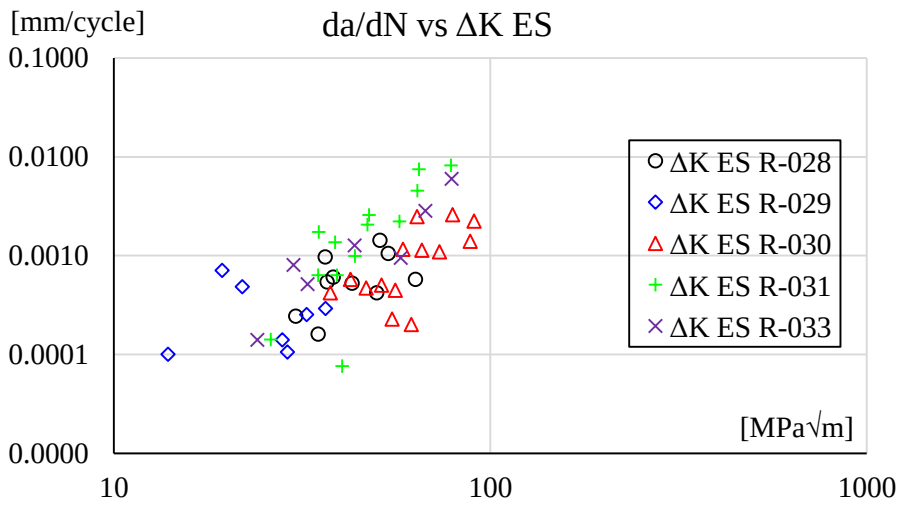

Figure 6-9 da/dN curve using the equivalent SIF range ES model

It was shown earlier how SIF mode III was present in four out the five thin tubes. Therefore, in order to look for an equivalent SIF, one needs to select a model that encompasses mode III, such as Schöllmann et al. Figure 6-10 shows the Paris

curve using the Schöllmann et. al. formulation for equivalent ΔK as presented in tables 11, 13, 15, 17 and 19 for each cycle.

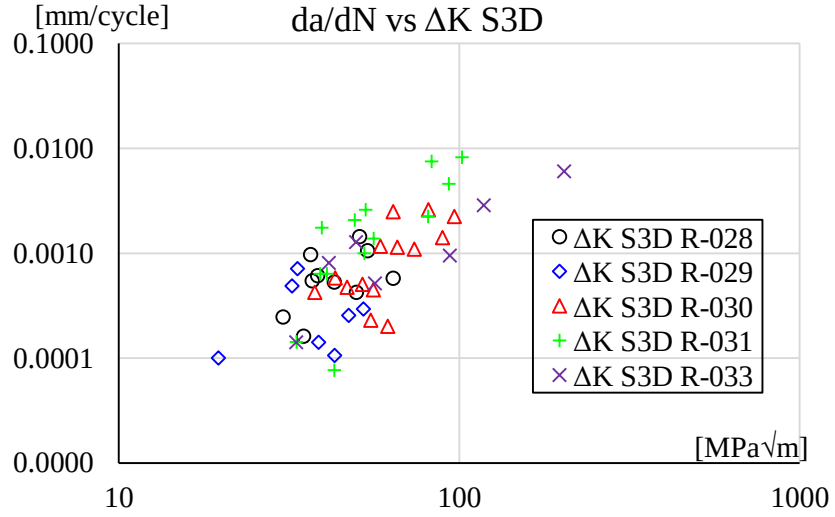

Figure 6-10. da/dN curve using the equivalent S3D SIF range model.

The crack growth rates in Figure 6-9 and Figure 6-10 were calculated by the secant method and they show a rather large scatter. Such statement becomes more visible when data for all five tube specimens, in terms of number of cycles N and total linear crack length a^*, is presented in Figure 6-11. One can see there are different crack growth rates for different cycles.

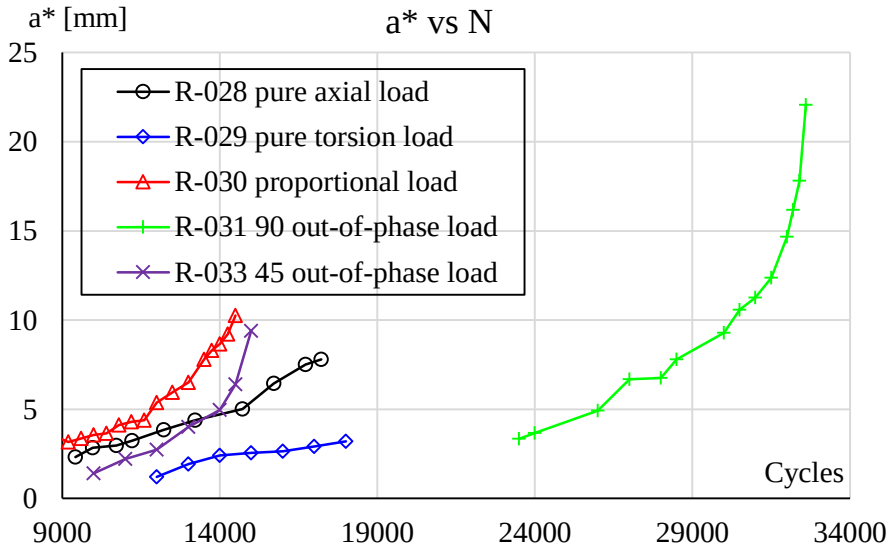

Figure 6-11. Linear crack lenght vs. number of cycles for the tube samples

To smooth such scatter, a correction of da/dN values was made using splines[7], so crack growth rates would fit Eq. (59) [82].

$$a = \left[a_0^{1-m} + C(1-m) \right]^{\frac{1}{1-m}} \tag{59}$$

When the sum of squared difference is minimal, coefficients C and m are found and upon deriving Eq. (59), it becomes Paris rule, Eq. (28), giving a new da/dN plot as presented in Figure 6-12 [82] where one can see that the equivalent Schöllmann et al. SIF falls within a narrower band when compared to the non-smoothed plot of Figure 6-10. The ALL straight line, represents the da/dN values using the ΔK S3D for the five samples and the last row of parameters C and m from Table 21.

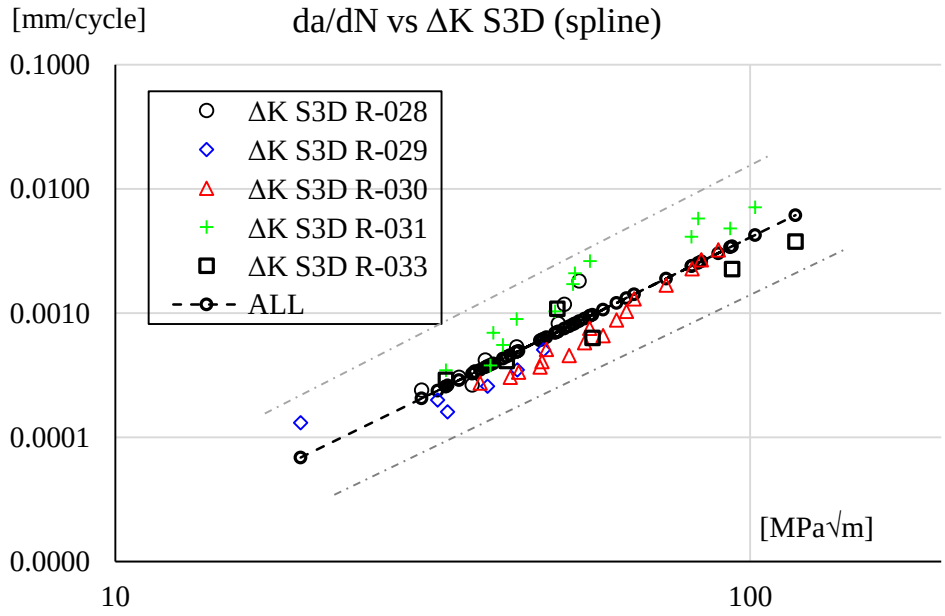

Figure 6-12. Adjusted da/dN vs. ΔK S3D for tube specimens

So, when plotting linear crack length versus number of cycles after doing a spline smoothing, one can see the more clearly the different crack growth rates for the specimens and even more, how they change when the cracks kink.

[7] A spline is an adapting fitting procedure that finds a set of linear paraments for each pair of consecutive points within a scatter of many points.

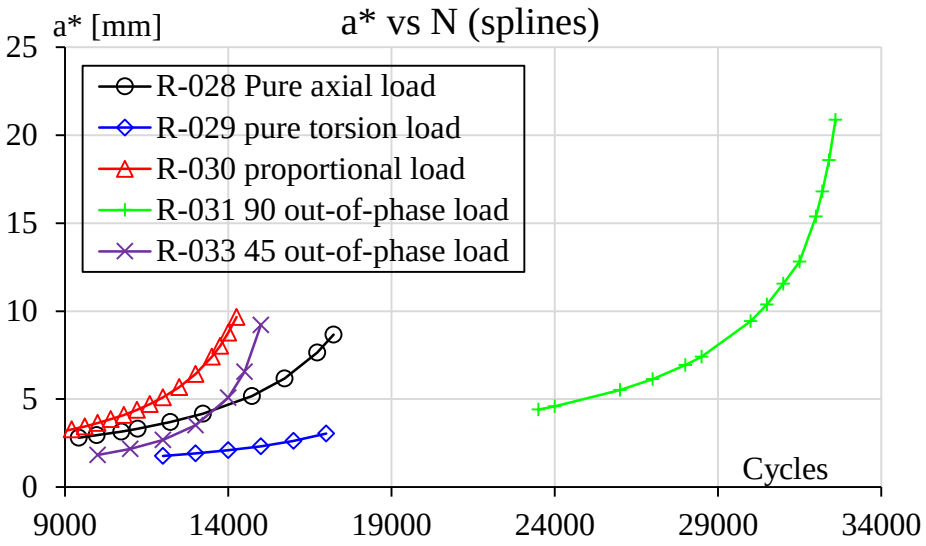

Figure 6-13. Linear crack lenght vs. number of cycles for the tube samples after spline smoothing

The values of the assumed crack driving force, ΔK S3D, were determined by only using measured displacement fields in the vicinity of crack tips. As previously mentioned, they take into account influence factors such as crack closure, surface roughness, crack flank friction, crack path kinking, and cyclic plasticity. Therefore, the ΔK S3D values have to be interpreted as effective.

In an ideal situation, the obtained data points would closely fall in a narrow band. However, the data points fall into a band of a factor 6 in ΔK direction and a factor of 8 in crack growth rate. One source of scatter is still due to the experimental technique, another source comes from the presumption that the mixed-mode Schöllmann et. al. hypothesis might not perfectly describe the FCG behavior, which is based on the MTS assumption. An extension of the Schöllmann et al. model from an equivalent SIF to an equivalent SIF range might be used to explain FCG behavior under and non-proportional mixed-mode loading. Nonetheless, cases have been reported in which fatigue crack growth did not obey to a MTS criterion but more to maximum shear stress criterion [25, 73, 80]. For such cases, the presented hypothesis cannot be expected to correlate all experimental results [82]. Against this background, it might not be too surprising that the MTS criterion does not work perfectly. Although some indications [73, 80], it is still open which condition leads to either normal or shear stress driven fatigue crack growth, respectively [82].

For cases for which the Schöllmann et al. hypothesis is valid, the FCG prediction requires to take all influencing phenomena into account which have impact on the crack tip fields [25, 53].

The scatter of points in Figure 6-12 (spline smoothed) cast the Paris rule coefficients, (Eq. (28) $da/dN=C\ \Delta K^{m}$), shown in Table 21, where R^2 is the correlation factor in data regression for each specimen separately and all combined.

If the parameters *C* and *m* are in fact material dependent, with *m* ranging from 1.5 to 6 for most metals [3], values in Table 21 ought to belong to the same distribution. However, under that premise, a projected crack growth rate might get affected due to the crack kinks preventing the crack from sliding/opening freely.

Table 21. Paris curve parameters for thin tubes using Figure 6-12´s points for each sample.

Spec.	**C ($1*10^{-6}$)**	**m**	**R^2**
R-028	0.001	3.47	0.9224
R-029	2.000	1.42	0.7808
R-030	0.003	3.04	0.9731
R-031	0.030	2.73	0.9290
R-033	0.3	1.97	0.9299
ALL	0.04	2.5	0.814

Additionally, the experimentally measured crack length for the thin tubes account for nonlinear phenomena such as crack closure and crack friction that hinders crack growth. For longer cracks, there is a bigger crack surface, therefore higher friction forces to overcome. Finally, another reason may be, as stated before, that the assumed equivalent SIF range hypothesis is not the best suited criterion to describe FCG. Those reasons may explain why the measured crack length is shorter than the predicted ones, especially after crack kinks.

The results shown in this section (6.4) seem to disagree with data published by Fremy et. al. [30] as they conclude that FCG under non-proportional loading depends on load history. However, the SIF values they used to come up with that conclusion were numerically calculated with peak values of K_I, K_{II} and K_{III} that produced the same equivalent SIF range for the different tested loading sequences.

Furthermore, another difference is that in [30] the crack closure problem was avoided by using a R > 0.33 so non-linearities such as roughness, plasticity induced closure, and environmental effects were not included as opposed to the SIF values used in this thesis which they did, because of the nature of their experimental measurement, with R=-1 for the thin tubes. Finally, the results in this section also disagree with results from Yu, Li, and Proust [27] who also tested thin tubes under some loading conditions very similar to the loading paths reported here. One source of disagreement could come from the fact that their numerically calculated SIFs did not include mode III opening. So their equivalent SIF range, calculated with the MTS criterion, lacks of the out-plane-contribution.

On the other hand, the findings in this section are not fully conclusive that the Schöllmann et al. model, which is MTS based, is able to describe well FCG under non-proportional load. Analysis of data presented in this section shows that Paris rule could describe FCG, even for non-proportional loading cases when the equivalent mixed-mode SIF range can only be calculated using the SIF ranges of the existing opening modes if they occur at the same instant. If they do not occur at the same time, an estimation process, such as the one presented in this section has to be used. SIF values must be determined for each crack length along the cycling history, not forgetting that mixed-mode SIF opening ratios vary during the cycle, and that non-linearities such as roughness, crack tip plasticity and crack flank friction make mixed-mode loading to be non-proportional to mixed-mode SIFs. Much better results will be met if experimentally determined SIFs are used in the analysis. In other words, the maximum equivalent SIF range should be evaluated from all possible equivalent SIFs occurring along a given cycle. This maximum equivalent SIF range will depend on the selected criterion for crack propagation. Although the present approach used the MTS criterion, first proposed by Erdogan and Sih [9] for opening modes I and II, and it was later extended by Schöllmann et al. [19] to include mode III, other criteria can be selected and tested using the same experimentally acquired displacement fields used in this thesis.

7. Conclusion and Future Works

7.1 Conclusion

Methods to calculate SIF from DIC displacements using LEFM formulation for three kinds of specimens were presented, explained, and analyzed. In some cases, results were compared with FEM simulations to corroborate findings. The ⌡ method did not work for negative loads, because at that loading stage the crack is closed so, it simply does not exist. The application of ⌡ in that stage would violate Rice´s formulation. Differences between the experimentally calculated SIF and FEM simulation results, where applicable, were attributed to accumulated cyclic plasticity, crack roughness, and crack blunting.

A dependable way to determine opening mode SIFs I, II and III from relative crack edges displacements, that were measured using the 3D-DIC technique, was presented. The use of the 3D-DIC technique is extremely important because the 2D-DIC technique is only applicable to plane problems (DCT and modified C(T) samples in this case), where the out-of-plane displacements are insignificant. Besides, the use of 3D-DIC allows the measurement of out-of-plane displacements, the consequently determination of mode III crack openings and associated K_{III} values. In the case of the thin tubes, the use of 3D-DIC is essential due to their geometry requires 3D measurement capabilities. Calculations of K_{III} were useful to show that, in some of the thin tubes, they were induced by the combination load-geometry, that they may be higher than the mode I and II SIFs therefore, making a

substantial difference in the calculation of equivalent SIFs and equivalent SIF ranges.

It was shown that mode I SIF is affected not only by the residual strain due to FCG but also on roughness between the crack faces, and crack kinking. The crack roughness acts as an inclined plane, enhancing mode I. For mode II and mode III SIFs, it is concluded they are affected by friction between the crack faces because, they need to overcome the friction force first, before any sliding starts happening.

Some LEFM-based models to predict crack kinking were evaluated using the experimentally calculated SIF and SIF ranges for proportional and non-proportional loading cases. For proportional loading most of the model (stress and energy based) do a close crack path prediction, except the MSS which was expected as the materials used in this thesis were ductile carbon steels not prone to shear dominated fracture. For the non-proportional loading they do not fare so well, as they were originally devised for proportional loading. However, the SED, which was the only energy-based model that include K_{III} in the formulation, got close to the experimentally observed crack angle. This is new information as literature does not report a success in SED evaluation for non-proportional loading. However, the way SIF and SIF ranges are evaluated here shows the SED works for non-proportional loading even though the value used for Ψ may change along crack growth, and it could not be assessed beyond its initial value. Further experiments with other loading secuences migh help analyze other cases with different data.

A way to evaluate equivalent SIF ranges for non-proportional loading using already-existing models for proportional loading was presented. Using the proposed method, coefficients of Paris rule were sought to predict crack growth fitting all

experimental data points using the Schöllmann et. al. equivalent SIF model. It was found that FCG could be acceptably described by Paris rule.

From the experimentally observed SIF, it was observed the ratio between SIFs II and I varied constantly during one cycle and from cycle to cycle for the non-proportionally loaded specimens even though the ratio axial load / torque was kept constant. It is concluded that such variation must be attributed to the constant change in local conditions product of local plasticity, geometry and loading conditions.

Finally, it was shown modes I, II and III were present in four of the thin tubes. The presence of out-of-plane displacements were not observed at first in the visual analysis of the fatigue grown specimens. They were later confirmed after the w-field DIC analysis in one non-proportional sample. That situation may help other researchers, when analyzing similar specimens, who consider only modes I and II, and the respective numerically deduced SIFs. Such omission may produce difficulties in explaining FCG if the mode III opening mode is not properly accounted for.

7.2
Recommendation for Future Works

Check the influence of T-stress on crack propagation angles for proportional loading cases. For that case, the evaluation of SIFs using full field method should be perfected to obtain SIF responses under negative axial load similar to the ones obtained with the COD method. Should the SIF be correctly calculated using full field information, the T-stress is already accounted for in the William´s series.

Continue working on the analysis of DIC measurements for the thin tubes. The ΔJ_{eff} could be calculated if a J decomposition method for multiaxial loading is successfully implemented.

Perform test on same thin tubes with different non-proportional loading cases so SIF, SIF ranges and a FCG can be extracted in the same manner as it was done here. This would help to furher clarify what was observed for the unified Paris rule.

Develop formulations for MEER and MTSN criteria that include KIII in the crack driving force and evaluate them using the experimentally calculated SIFs. Another possible way to evaluate crack path under non-proportional loading is to evaluate crack kinking criteria that includes the T-stress effect.

Evaluate out-of-plane angle, Ψ, with stress as a function of SIFs (K_I, K_{II}, K_{III}) with a range of angles and compare against K_{III}/K_I. A parameter such as the one suggested by Highsmith and Yang could be studied, looking for a threshold that could tell where twisting occurs.

8. References

1. Anderson TL (2005) Fracture Mechanics, 3rd ed. CRC Press, Boca Raton
2. Zhu XK, Joyce J (2012) Review of fracture toughness (G, K, J, CTOD, CTOA) testing and standardization. Eng Fract Mech 85:1–46. doi: 10.1016/j.engfracmech.2012.02.001
3. Castro JT, Meggiolaro MA (2009) Fadiga - Técnicas e Práticas de Dimensionamento Estrutural sob Cargas Reais de Serviço: Volume I & II, 2nd ed. CreateSpace
4. Irwin GR (1957) Analysis of Stresses and Strains near the End of a Crack Traversing a Plate. Appl Mech 24:361–364.
5. Williams ML (1957) On the Stress State at the Base of a Stationary Crack. J Appl Mech 24:109–114. doi: 10.1115/1.3640470
6. Paris PC, Gomez MP, Anderson WE (1961) A Rational Analytic Theory of Fatigue. Trend Eng 13:9–14.
7. Cherepanov GP (1967) The Propagation of Cracks in a Continuous Medium. J Appl Math Mech 31:503–512.
8. Rice JR (1968) A Path Independent Integral and the Approximate Analysis of Strain Concentration by Notches and Cracks. J Appl Mech 35:379–386. doi: 10.1.1.160.9792
9. Erdogan F, Sih GC (1963) On the Crack Extension in Plates Under Plane Loading and Transverse Shear. J Basic Eng 85:519. doi: 10.1115/1.3656897
10. Sih GC (1973) Some basic problems in fracture mechanics and new concepts. Eng Fract Mech 5:365–377. doi: 10.1016/0013-7944(73)90027-1
11. Goldstein R V., Salganik RL (1974) Brittle fracture of solids with arbitrary cracks. Int J Fract 10:507–523. doi: 10.1007/BF00155254
12. Strifors HC (1974) A generalized force measure of conditions at crack tips.

Int J Solids Struct 10:1389–1404. doi: 10.1016/0020-7683(74)90089-4

13. Nuismer RJ (1975) An energy release rate criterion for mixed mode fracture. Int J Fract 11:245–250. doi: 10.1007/BF00038891

14. Chang KJ (1981) On the maximum strain criterion—a new approach to the angled crack problem. Eng Fract Mech 14:107–124. doi: 10.1016/0013-7944(81)90021-7

15. Theocaris PS, Andrianopoulos NP (1982) The T-criterion applied to ductile fracture. Int J Fract 20:125–130. doi: 10.1007/BF01130617

16. Papadopoulos GA (1989) New concepts on the Det.-criterion. Eng Fract Mech 33:283–293. doi: 10.1016/0013-7944(89)90030-1

17. Li C (1989) Vector CTD criterion applied to mixed mode fatigue crack growth. Fatigue Fract Eng Mater Struct 12:59–65.

18. Maccagno TM, Knott JF (1992) The mixed mode I/II fracture behaviour of lightly tempered HY 130 steel at room temperature. Eng Fract Mech 41:805–820. doi: 1016/0013-7944(92)90233-5

19. Schöllmann M, Richard HA, Kullmer G, Fulland M (2002) A new criterion for the prediction of crack development in multiaxially loaded structures. Int J Fract 117:129–141. doi: 10.1023/A:1020980311611

20. Wasiluk B, Golos K (2000) Prediction of crack growth direction under plane stress for mixed-mode I and II loading. Fatigue Fract Eng Mater Struct 23:381–386. doi: 10.1046/j.1460-2695.2000.00300.x

21. Demir O, Ayhan AO (2016) Investigation of mixed mode-I/II fracture problems - Part 2: evaluation and development of mixed mode-I/II fracture criteria. Frat ed Integrità Strutt 35:340–349. doi: 10.3221/IGF-ESIS.35.39

22. Richard HA, Fulland M, Sander M (2004) Theoretical crack path prediction. Fatigue Fract Eng Mater Struct 28:3–12. doi: 10.1111/j.1460-2695.2004.00855.x

23. Zerres P, Bruning J, Vormwald M (2010) Fatigue crack growth behavior of fine-grained steel S460N under proportional and non-proportional loading. Eng Fract Mech 77:1822–1834. doi: 10.1016/j.engfracmech.2010.02.008

24. Highsmith S (2009) Non-Proportional Mixed-Mode Fatigue. Georgia

University of Technology

25. Zerres P, Vormwald M (2014) Review of fatigue crack growth under non-proportional mixed-mode loading. Int J Fatigue 58:75–83. doi: 10.1016/j.ijfatigue.2013.04.001

26. Yang Y (2014) Linear elastic fracture mechanics-based simulation of fatigue crack growth under non- proportional mixed-mode loading. Technischen Universität Darmstadt

27. Yu X, Li L, Proust G (2017) Fatigue crack growth of aluminium alloy 7075-T651 under proportional and non-proportional mixed mode I and II loads. Eng Fract Mech 174:155–167. doi: 10.1016/j.engfracmech.2017.01.008

28. Hos Y, Vormwald M (2016) Experimental study of crack growth under non-proportional loading. Int. J. Fatigue

29. Mei J, Dong P, Kalnaus S, Jiang Y, Wei, Z (2017) A path-dependent fatigue crack propagation model under non-proportional modes I and III loading conditions. Eng Fract Mech 182:202–214. doi: 10.1016/j.engfracmech.2017.07.026

30. Fremy F, Pommier S, Poncelet M, Raka B, Galenne, E, Courtin S, Roux JC (2014) Load path effect on fatigue crack propagation in I + II + III mixed mode conditions - Part 1: Experimental investigations. Int J Fatigue 62:104–112. doi: 10.1016/j.ijfatigue.2013.06.002

31. Tschegg E (1983) Sliding mode crack closure and mode III fatigue crack growth in mild steel. Acta Metall 31:1323–1330. doi: 10.1016/0001-6160(83)90003-2

32. Pook LE (1985) Comments on fatigue crack growth under mixed modes I and III and pure mode III loading. Multiaxial Fatigue, ASTM STP 853 249–263.

33. Hos Y (2017) Numerical and experimental investigation of crack growth in thin-walled metallic structures under nonproportional combined loading. Technischen Universität Darmstadt

34. Irwin GR (1958) Discussion of: the dynamic stress distribution surrounding a running crack. A photoelastic analysis. In: SESA XVI. pp 93–86

35. Wells AA, Post D (1958) The Dynamic Stress Distribution Surrounding a Running Crack. A Photoelastic Analysis. SESA XVI

36. Dally JW, Sanford RJ (1987) Strain-Gage Methods for Measuring the Opening-Mode Stress Intensity Factor, KI. J Appl Mech 27:381–388.

37. Barker DB, Sanford RJ, Chona R (1985) Determining K and Related Stress-field Parameters from Displacement Fields. Exp Mech 25:399–407. doi: 10.1007/BF02321339

38. McNeill SR, Peters WH, Sutton MA (1987) Estimation of Stress Intensity Factor by Digital Image Correlation. Eng Fract Mech 28:101–112. doi: 10.1016/0013-7944(87)90124-X

39. Sanford RJ (1989) Determining Fracture Parameters with Full-field Optical Methods. Exp Mech 29:241–247. doi: 10.1007/BF02321401

40. Lopez-Crespo P, Shterenlikht A, Patterson EA, Yates JR, Withers PJ (2008) The Stress Intensity of Mixed Mode Cracks Determined by Digital Image Correlation. J Strain Anal Eng Des 43:769–780. doi: 10.1243/03093247JSA419

41. Yates JR, Zanganeh M, Asquith D, Tai YH (2009) Quantifying Crack Tip Displacement Fields : T- Stress and CTOA. In: Crack Paths 2009. pp 57–74

42. Zhang R, He L (2012) Measurement of mixed-mode stress intensity factors using digital image correlation method. Opt Lasers Eng 50:1001–1007. doi: 10.1016/j.optlaseng.2012.01.009

43. Hos Y, Vormwald M, Freire JLF (2015) Measurement and simulation of strain fields around crack tips under mixed-mode fatigue loading. Frat ed Integrità Strutt 33:42–55. doi: 10.3221/IGF-ESIS.33.06

44. Hos Y, Vormwald M, Freire JLF (2015) Using Digital Image Correlation to Determine Mixed Mode Stress. COTEQ 2015

45. Harilal R, Vyasarayani CP, Ramji M (2015) A linear least squares approach for evaluation of crack tip stress field parameters using DIC. Opt Lasers Eng 75:95–102. doi: 10.1016/j.optlaseng.2015.07.004

46. Kotousov A, He Z, Fanciulli A (2015) Application of digital image correlation technique for investigation of the displacement and strain fields

within a sharp notch. Theor Appl Fract Mech 79:51–57. doi: 10.1016/j.tafmec.2015.05.012

47. He Z, Kotousov A (2015) Estimation of Stress Intensity Factors from Near Crack Tip Field. Int J Mech Aerospace, Ind Mechatron Manuf Eng 9:1094–1098.

48. Vormwald M, Hos Y, Freire JLF, González GLG, Díaz JG (2017) Variable mode-mixity during fatigue cycles – crack tip parameters determined from displacement fields measured by digital image correlation. Frat ed Integrita Strutt 41:320–328. doi: 10.3221/IGF-ESIS.41.42

49. Gonzáles GLG, Díaz JG, González JAO, De Castro JTP, Freire JLF (2017) Determining SIFs Using DIC Considering Crack Closure and Blunting. In: Zhu Y, Zehnder AT (eds) Exp. Appl. Mech. Vol 4. Springer, Orlando, FL, pp 25–36

50. Díaz JG, Gonzáles GLG, González JAO, Freire JLF (2017) Analysis of Mixed-Mode Stress Intensity Factors using Digital Image Correlation Displacement Fields. 24th COBEM. doi: 10.26678/ABCM.COBEM2017.COB17-0684

51. Mróz KP, Mróz Z (2010) On crack path evolution rules. Eng Fract Mech 77:1781–1807. doi: 10.1016/j.engfracmech.2010.03.038

52. Shukla A, Dally JW (2010) Experimental Solid Mechanics, 1st ed. College Enterprises Inc, Knoxville, TN

53. Vormwald M (2015) Multi-challenge aspects in fatigue due to the combined occurrence of multiaxiality, variable amplitude loading, and size effects. Frat ed Integrità Strutt 33:253–261. doi: 10.3221/IGF-ESIS.33.31

54. Miranda ACO, Meggiolaro MA, De Castro JTP, Martha LF (2003) Fatigue life prediction of complex 2D components under mixed-mode variable amplitude loading. Int J Fatigue 25:1157–1167. doi: 10.1016/S0142-1123(03)00118-X

55. Peters WH, Ranson WF (1982) Digital Imaging Techniques In Experimental Stress Analysis. Opt Eng. doi: 10.1117/12.7972925

56. Sutton MA, Wolters WJ, Peters WH, Ranson WF, McNeill SR (1983)

Determination of Displacements using an Improved Digital Correlation Method. Image Vis Comput 1:133–139. doi: 10.1016/0262-8856(83)90064-1

57. Peters WH, Ranson, W F, Sutton MA, Chu TC, Anderson JJ (1983) Application Of Digital Correlation Methods To Rigid Body Mechanics. Opt Eng. doi: 10.1117/12.7973231

58. Sutton MA, Orteu JJ, Schreier H (2009) Image Correlation for Shape, Motion and Deformation Measurements: Basic Concepts, Theory and Applications. doi: 10.1007/978-0-387-78747-3

59. Yoneyama S, Arikawa S, Kusayanagi S, Hazumi K (2014) Evaluating J-integral from Displacement Fields Measured by Digital Image Correlation. Strain 50:147–160. doi: 10.1111/str.12074

60. Kim JH, Paulino GH (2005) Consistent Formulations of the Interaction Integral Method for Fracture of Functionally Graded Materials. J Appl Mech 72:351. doi: 10.1115/1.1876395

61. Molteno MR, Becker TH (2015) Mode I – III Decomposition of the J Integral from DIC Displacement Data. Strain 51:492–503. doi: 10.1111/str.12166.M.

62. He Z, Kotousov A (2016) On Evaluation of Stress Intensity Factor from In-Plane and Transverse Surface Displacements. Exp Mech 56:1385–1393. doi: 10.1007/s11340-016-0176-8

63. Begley JA, Landes JD (1972) The J Integral as a Fracture Criterion. Astm Spec Tech Publ 514 1–20.

64. Yau JF, Wang SS, Corten HT (1980) A Mixed-Mode Crack Analysis of Isotropic Solids Using Conservation Laws of Elasticity. J Appl Mech 47:335. doi: 10.1115/1.3153665

65. Wüthrich C (1982) The extension of the J Integral concept to fatigue cracks. Int J Fract 20:35–37. doi: 10.1007/BF01141264

66. Dowling NE (1977) Crack Growth During Low-Cycle Fatigue of Smooth Axial Specimens. In: ASTM STP 637. ASTM, pp 97–121

67. Vasco-Olmo JM, Díaz FA, Antunes FV, James MN (2017) Experimental evaluation of CTOD in constant amplitude fatigue crack growth from crack

tip displacement fields. Frat ed Integrita Strutt 11:157–165. doi: 10.3221/IGF-ESIS.41.22

68. Rozumek D, Macha E (2009) A survey of failure criteria and parameters in mixed-mode fatigue crack growth. Mater Sci 45:190–210. doi: 10.1007/s11003-009-9179-2

69. Pommier S (2015) Development of an Incremental Model for Fatigue Crack Growth Predictions. J Aerosp lab 11:1–12. doi: 10.12762/2015.AL09-11

70. Haboussa D, Elguedj T, Leblé B, Combescure A (2012) Simulation of the shear-tensile mode transition on dynamic crack propagations. Int J Fract 178:195–213. doi: 10.1007/s10704-012-9729-8

71. Richard HA (1985) Bruchvorhersagen bei überlagerter normal and Schubbeanspruchung von Rissen. VDI-Verlag, Düsseldorf

72. Badaliance R (1980) Application of Strain Energy Density Factor to Fatigue Crack Growth Analysis. Eng Fracrure Mech 13:657–666. doi: 10.1016/0013-7944(80)90094-6

73. Highsmith S (2009) Crack path determination for non-proportional mixed-mode fatigue. Georgia University of Technology

74. Tanaka K (1974) Fatigue crack propagation from a crack inclined to the cyclic tensile axis. Eng Fract Mech 6:493–507.

75. Miranda ACO, Meggiolaro MA, De Castro JTP, Martha LF, Bittencourt TN (2003) Fatigue life and crack path predictions in generic 2D structural components. Eng Fract Mech 70:1259–1279. doi: 10.1016/S0013-7944(02)00099-1

76. Pei G, Asaro RJ (1997) Crack deflection in functionally graded materials. Int J Solids Struct 34:3085–3098.

77. Pook L (1980) The significance of mode I branch cracks for combined mode failure. Fract. Fatigue. Elasto-Plasticity, Thin Sheet Micromechanisms Probl.

78. Pook L (1985) The fatigue crack direction and threshold behaviour of mild steel under mixed Mode I and III loading. Int J Fatigue 7:21–30. doi: 10.1016/0142-1123(85)90004-0

79. Richard HA, Schramm B, Schirmeisen NH (2014) Cracks on Mixed Mode loading - Theories, experiments, simulations. Int J Fatigue 62:93–103. doi: 10.1016/j.ijfatigue.2013.06.019

80. Yang Y, Vormwald M (2017) Fatigue crack growth simulation under cyclic non-proportional mixed mode loading. Int J Fatigue 102:37–47. doi: 10.1016/j.ijfatigue.2017.04.014

81. Hos Y, Freire JLF, Vormwald M (2015) Measurements of strain fields around crack tips under proportional and non-proportional mixed-mode fatigue loading. Int J Fatigue 89:87–98. doi: 10.1016/j.ijfatigue.2016.01.018

82. Vormwald M, Hos Y, Freire JLF, González GLG, Díaz JG (2018) Crack tip displacement fields measured by digital image correlation for evaluating variable mode-mixity during fatigue crack growth. Int J Fatigue. doi: 10.1016/j.ijfatigue.2018.04.030

83. Richard HA, Eberlein A (2016) Material characteristics at 3D-mixed-mode-loadings. In: 21st Eur. Conf. Fract. ECF21. Elsevier, Catania, pp 2452–3216

84. Harilal R (2015) A Novel Way to Determine Crack Tip Stress Field Parameters Involving Displacement Field Estimated using Digital Image Correlation Technique. Indian Institute of Technology Hyderabad

85. Yoneyama S, Morimoto Y, Takashi M (2006) Automatic evaluation of mixed-mode stress intensity factors utilizing digital image correlation. Strain 42:21–29. doi: 10.1111/j.1475-1305.2006.00246.x

86. Nowell D, Kartal ME, De Matos PFP (2013) Digital image correlation measurement of near-tip fatigue crack displacement fields: constant amplitude loading and load history effects. Fatigue Fract Eng Mater Struct 36:3–13. doi: 10.1111/j.1460-2695.2012.01707.x

87. Beretta S, Patriarca L, Rabbolini S (2017) Stress intensity factor calculation from displacement fields. Frat ed Integrita Strutt 11:269–276. doi: 10.3221/IGF-ESIS.41.36

88. Díaz FA, Yates JR (2013) Evaluation of the Effective Stress Intensity Factor. 25:109–116. doi: 10.3221/IGF-ESIS.25.16

89. Pommier S, Hamam R (2006) Incremental model for fatigue crack growth

based on a displacement partitioning hypothesis of mode I elastic-plastic displacement fields. Fatigue Fract Eng Mater Struct 36:582–598. doi: 10.1111/j.1460-2695.2007.01128.x

90. Kibey S, Sehitoglu H, Pecknold DA (2004) Modeling of fatigue crack closure in inclined and deflected cracks. Int J Fatigue 129:279–308. doi: 10.1023/B:FRAC.0000047787.94663.c8

91. Tong J, Yates JR, Brown MW (1995) A model for Sliding Mode Crack Closure Part I: Theory for Pure Mode II Loading. Eng Fract Mech 52:599–611. doi: 10.1016/0013-7944(95)00044-V

92. Brahma KK, Dash PK, Dattaguru B (1989) Observation of crack closure using a crack mouth opening displacement gauge. Int J Fatigue 11:37–41.

93. Mokhtarishirazabad M, Lopez-Crespo P, Moreno B, Lopez-Moreno A, Zanganeh M. (2016) Evaluation of crack-tip fields from DIC data: A parametric study. Int J Fatigue 89:11–19. doi: 10.1016/j.ijfatigue.2016.03.006

94. Becker TH, Mostafavi M, Tait RB, Marrow TJ (2012) An approach to calculate the J Integral by digital image correlation displacement field measurement. Fatigue Fract Eng Mater Struct 35:971–984. doi: 10.1111/j.1460-2695.2012.01685.x

95. Smith, D. J. Ayatollahi MRPJ (2001) The role of T-stress in brittle fracture for linear elastic materials under mixed-mode loading. Fatigue Fract Eng Mater Struct 24:137–150. doi: 10.1046/j.1460-2695.2001.00377.x

96. Kim JH, Paulino GH (2003) T-stress, mixed-mode stress intensity factors, and crack initiation angles in functionally graded materials: A unified approach using the interaction integral method. Comput Methods Appl Mech Eng 192:1463–1494. doi: 10.1016/S0045-7825(02)00652-7

Appendix A.

Chemical composition for modified C(T) specimen

MTC MATERIALS TEST CENTER LTDA.

RELATÓRIO DE ENSAIO N°: 17100646QUI Fl. 1/1

Empresa interessada : **PONTIFÍCIA UNIVERSIDADE CATÓLICA DO RIO DE JANEIRO**
Rua Marquês de São Vicente, n° 225 – Gávea - Rio de Janeiro / RJ

Pedido de ensaio : 000846

Natureza do trabalho : **ANÁLISE QUÍMICA.**

Laboratório MTC SISTEMA DA QUALIDADE CONFORME ISO 9001

Informações fornecidas pelo interessado sobre o material ensaiado:

QUANTIDADE.....: 01 Amostra para análise química
IDENTIFICAÇÃO.....: Freire

RESULTADOS OBTIDOS
COMPOSIÇÃO QUÍMICA (%)

Carbono	(C)	0,268
Silício	(Si)	0,046
Manganês	(Mn)	0,68
Fósforo	(P)	0,0042
Enxofre	(S)	0,025
Cromo	(Cr)	0,016
Níquel	(Ni)	0,022
Molibdênio	(Mo)	<0,0020
Alumínio	(Al)	<0,0010
Cobre	(Cu)	0,010
Cobalto	(Co)	0,0015
Titânio	(Ti)	0,0015
Nióbio	(Nb)	0,0031
Vanádio	(V)	0,0020
Tungstênio	(W)	<0,010
Chumbo	(Pb)	<0,0030
Boro	(B)	<0,0005
Estanho	(Sn)	0,0012
Zinco	(Zn)	<0,0020
Arsênio	(As)	0,0068
Bismuto	(Bi)	0,0035
Cálcio	(Ca)	<0,0001
Cério	(Ce)	<0,0030
Zircônio	(Zr)	<0,0015
Lantânio	(La)	0,0022
Ferro	(Fe)	98,9

Espectrômetro de Emissão Óptica: SpectroMaxx - Identificação MTC 2050 – Certificado Spectro Sul Americana N° 121411/06 e 18022016-A - Válido até 02/2018

Procedimento MTC: PO-301.

Normas de Referências: ASTM A 751, ed 2014a.

Local e Data dos Ensaios: Rio de Janeiro, 18 de Outubro de 2017.
Emissão do Relatório: Rio de Janeiro, 18 de Outubro de 2017.

Maria Cecília Mendes da Silva
Gerente Técnico de Laboratório

Os resultados apresentados no presente documento têm significação restrita e se aplicam somente ao objeto ensaiado ou calibrado. A sua reprodução, total ou parcial, só poderá ser feita mediante prévia autorização do laboratório emitente.

Materials Test Center Ltda.
Rua Leopoldino de Oliveira, 392 - Madureira - Rio de Janeiro - RJ - CEP 21360-060 - Tel.: (21) 3830-0011 / 2451-9599
mtc@laboratoriomtc.com.br | www.laboratoriomtc.com.br